Cyprus University of Technology

Faculty of Fine and Applied Arts

Doctoral Dissertation

Wave-Based Geometrical Acoustics for Accurate and Efficient Sound Rendering

Panagiotis Charalampous

Limassol, November 2020

CYPRUS UNIVERSITY OF TECHNOLOGY

FACULTY OF FINE AND APPLIED ARTS

DEPARTMENT OF MULTIMEDIA AND GRAPHIC ARTS

Doctoral Dissertation

WAVE-BASED GEOMETRICAL ACOUSTICS FOR ACCURATE AND EFFICIENT SOUND RENDERING

Panagiotis Charalampous

Limassol, November 2020

Approval Form

Doctoral Dissertation

WAVE-BASED GEOMETRICAL ACOUSTICS FOR ACCURATE AND EFFICIENT SOUND RENDERING

Presented by

Panagiotis Charalampous

Examination Committee Members:

Assistant Professor Despina Michael-Grigoriou, Cyprus University of Technology (Supervisor)

Signature _____

Professor Constantinos S. Pattichis, University of Cyprus (Committee Chair)

Signature _____

Professor Lauri Savioja, Aalto University, Finland

Signature _____

Cyprus University of Technology

Limassol, November 2020

Copyrights

ABSTRACT

Keywords: Sound Rendering, Geometrical Acoustics, Sound Propagation, Wave-Based Acoustics, Prioritized Tracing

Sound rendering has many important applications in both engineering software tools and virtual reality systems. However, the complexity of the calculations has led to a gap between research for accurate acoustic modeling techniques and techniques used for efficient sound rendering in performance critical and engineering applications such as virtual reality systems and acoustical simulation tools, resulting to respective trade-offs in both research fields.

In this thesis, we attempt to bridge the gap by presenting a calculation model that can deliver accurate calculation results for a wide range of cases in computation times suitable for practical use. Our model combines geometrical acoustics, a technique which is widely used for efficient sound rendering applications with wave-based equations which allow for the accurate calculation of wave-based phenomena like resonances, noise cancelling and room modes. Our work is incorporated in a commercially available software application as a demonstration of the practical applicability of the calculation model. The model incorporates wave-based calculations for sound reflections, sound diffractions, atmospheric absorption, and atmospheric refraction. Algorithms for detecting the relevant sound paths are introduced. We validate the performance of our model by running simulations on several different setups and comparing the results with sound measurements and theoretical predictions. Our results show an improvement in accuracy when compared to other widely used engineering models. Also, our model proves capable of accounting for wave-based phenomena like sound diffractions, room modes and the seat-dip effect.

Furthermore we improve the efficiency of geometrical acoustics tracing algorithms by looking into how the tree traversal type affects the performance of such algorithms, and by proposing methods that use an intelligent prioritization of the tree traversal to improve the computation time of sound path detection. We show that the type of the tree traversal can affect the performance of algorithms based on the image source method, with differences being of perceptual significance. We introduce a novel algorithm using a prioritized ray tracing technique and we show improvements when compared to a non-

prioritized version of it as well as other popular algorithms. At last, we use prioritization techniques to demonstrate improvements in calculating room acoustics parameters in engineering applications.

TABLE OF CONTENTS

LIST OF TABLES

LIST OF FIGURES

LIST OF ABBREVIATIONS

BEM: Boundary Element Method

EA: Excess Attenuation

GA: Geometrical Acoustics

HRTF: Head Related Transfer Function

FEM: Finite Element Method

FDTD: Finite Differences Time Domain

IR   Impulse Response

ISO   International Standards Organization

OTL   Olive Tree Lab

WBGA   Wave-Based Geometrical Acoustics

1 Introduction

Auditory perception is one of the five basic human senses. It allows humans to capture vibrations of pressure in solids, liquids, and gases and perceive them as sounds through a complex mechanism located in the human ear through a process called "hearing", providing important clues about their surrounding environment. Sound, as perceived by hearing, has evolved as one of human's most important tools for communication and orientation. As a result, the study of sound and hearing has captured considerable attention and became a discrete field of study in physics, called "acoustics". The main objective of acoustics was to demystify the way sound is transmitted throughout the environment and formulate models that could explain and predict the propagation of sound waves.

An extension of the study of acoustics was the implementation of computerized models for the prediction of the behavior of sound, using methods and theories developed by acousticians. Since the mid of the previous century, shortly after the introduction of digital computers, the first papers on computerized predictions of sound behavior were published (Allred & Newhouse, 1958). This marked the creation of a new research field, involving both acoustics and computer science, known as computational acoustics.

Since its inception, the primary objective of computational acoustics has expanded from developing prediction models for architectural acoustics to a variety of usages like various computer-aided design tools, video games and virtual reality applications. Computational acoustics have come a long way since the presentation of the earliest research works in the field, progressing from calculation tools predicting numerical values of acoustical parameters, like sound level and reverberation time, to engines capable of delivering a complete audible experience through three-dimensional sound reproduction systems. Nowadays, computational acoustics is a field stretching from the development of new and more accurate models for calculating various acoustical phenomena to state-of-the-art sound rendering engines intended for real-time use in interactive applications.

The calculation of sound propagation, being a complicated problem, requires substantial computing resources, which increase in a nonlinear manner as the complexity of

computed models grows. Thus, in recent years, research emphasis has been given in developing methods that would allow the development of software tools with practical use for the aforementioned areas of interest. Nowadays, substantial progress has been achieved in all fronts, both in the accuracy of the models used as well as the speed of computation.

However, as Savioja and Svensson note in a recent review, there appears to be a gap between the communities that investigate accurate acoustic modeling techniques for acoustic design and those who focus on techniques for the entertainment and virtual reality industry (Savioja & Svensson, 2015). Researchers who deal with accurate acoustic modeling techniques focus mostly on the calculation of isolated acoustical phenomena like sound reflections, sound diffractions and many more, while paying attention mostly to the accurate reproduction of measured results. On the other hand, techniques focusing on efficient time-sensitive sound rendering often use shortcuts in the computation process, which inevitably leads to lower accuracy in the calculated outcome. While such deviations in accuracy might not be of significant or perceivable importance in the actual domain of use, which is video games and virtual reality applications, it becomes a showstopper when it comes to adopting these techniques for more serious use, like for architectural and environmental acoustics applications.

In this work we aim to make the first steps to bridge this gap. Our focus is to develop methods that deliver accurate results for acoustics calculations in time suitable for practical use. To prove the practicality of our approach, the final product of our work is incorporated into a commercially available software package, Olive Tree Lab (OTL) Suite (Olive Tree Lab Suite, 2020). To achieve this, the research effort supporting this thesis was mentored by GET Lab of the Department of Multimedia and Graphics Arts of Cyprus University of Technology in collaboration with P.E. Mediterranean Acoustics Ltd which is the company developed the aforementioned software package. Most of the part of the current research work is already a part of OTL Suite while some of the latter parts are still in experimental prototypes planned for future releases.

1.1 Scope of Work

The main objective of the current thesis is to develop a computational model for simulating the propagation of sound in 3D environments that will yield results with

improved accuracy compared to the current models while calculating the results in acceptable time for practical use. We focus on developing calculation methods based on geometrical acoustics since it is a group of methods that has been used successfully in the industry. We extend geometrical acoustics to account for wave-based phenomena as well as phenomena that current commercial calculation models fail to account for, like sound diffractions, atmospheric turbulence, and atmospheric refraction. We also propose novel tracing algorithms that improve the execution speed of geometrical acoustics techniques. At last, we evaluate the accuracy of our model by comparing the results with sound measurements and theoretical predictions and we assess the improvements achieved by our model by comparing the results with other proposed calculation models.

Our model is incorporated in a commercially available application that allows auralization, as a proof of concept that our model has practical applicability.

1.1.1 Motivation

There is a need in current commercial applications for sound rendering with improved accuracy in calculation results while keeping the calculation times short for practical use. Accurate sound rendering calculations require the use of wave-based methods while geometrical acoustics have been used to shorten calculation times. The motivation behind this thesis is to develop methods that allow the use of wave-based methods in geometrical models so that they can be used by widely available software solutions as well as bridge the gap between models used by acoustical engineers and the entertainment industry.

1.1.2 Problem Statement

Research on calculating accurately the propagation of sound has progressed substantially during the last decades, however much of this research has not found its way to widely used applications. Most of commercial applications for sound auralization still use techniques that ignore the wave nature of sound and/or significant characteristics of sound propagation like sound diffraction. The major obstacle for this transition is the generalization of such models for arbitrary 3D geometries and the ability of contemporary software solutions to calculate the required information. For

example, many of the available geometrical models for acoustical phenomena require certain parameters as inputs e.g. to calculate the sound diffraction over a wedge you need to have the angles between the rays and the wedge surfaces. Therefore, even though these models yield accurate results for simple cases, using them in a general calculation model where the input is an arbitrary 3D model becomes a complicated problem and a research task itself. Despite the fact that wave-based solutions for individual sound phenomena, like sound diffraction, sound reflection from material impedance and many other exist, there is a gap in general solutions that allow to input an arbitrary geometry use it to calculate the sound propagation and auralize the result as an output.

This problem has caused the gap between accurate acoustic modeling techniques for acoustic design and those who focus on techniques for the entertainment and virtual reality industry mentioned in the introduction. Since general fast wave-based models are missing from literature, most of the research about computational models used in models with real-time constraints is based on simplified energy-based calculations that lack adequate accuracy and ignore the wave nature of sound.

1.1.3 Thesis Objectives

The objectives (O_i) of this thesis address the accuracy and the efficiency of sound computation: The specific objectives are as follow:

Towards accurate computations:

O_1: Identify wave-based models from existing research that can be used in geometrical acoustics models and allow the calculation of various acoustical phenomena with improved accuracy when compared to industry popular geometrical acoustics models.

O_2: Develop a calculation model based on geometrical acoustics that will generalize the models identified in O_1. Develop tracing algorithm to detect sound paths for arbitrary 3D geometries and incorporate them in a single solution.

O_3: Develop solutions for automatic calculation of parameters required as inputs for the models of point 1, allowing the application of our solution on arbitrary geometries.

Towards efficient computations:

O$_4$: Introduce new algorithms that improve the behavior of the geometrical acoustics tracing process to speed up the computation process and bridge the gap between accurate engineering applications and virtual reality solutions.

Overall:

O$_5$: Integrate all the above in a single framework

1.1.4 Thesis Structure

This thesis is organized in five chapters. Chapter 1 and Chapter 5 consist of introduction and conclusion and Chapters 2, 3 and 4 are the main chapters of the thesis. Chapter 2 is the Background and Related Work; Chapter 3 mainly focuses on thesis objectives related to accuracy and Chapter 4 on the objective related to efficiency.

Chapter 2 presents a comprehensive review of the subject matters on which this thesis is touching. We also classify geometrical acoustics tracing algorithms based on a novel way. We group the existing literature based on the way each method improves the speed of the tree traversal by defining three distinct ways of achieving such an improvement a) tree pruning b) traversal acceleration and c) traversal prioritization.

Chapter 3 covers:

a. The construction of a computational geometrical acoustics model that calculates accurate transfer functions (O$_1$ and O$_2$).
b. The introduction of novel algorithms for speeding up the image source method (O$_4$) and calculating sound diffraction rays from multiple parallel edges, reflected-diffracted rays as well as rays bended by sound refraction (O$_3$).
c. The validation of this model based on several published case studies. These case studies include:
    i.   Calculation of room modes and comparison with measurements
    ii. Comparison with the calculation model proposed by ISO 9613-2
    iii. Calculation of sound propagation in an ancient theatre and comparison of the results with measurements
    iv. Calculation of the seat dip effect in a 3D model

v.   Calculation of sound propagation by wind turbines and comparison with sound measurements

Chapter 4 covers:

a. Investigation of the impact of tree traversal types on typical image source methods.

b. Implementation of two novel algorithms, based on traversal prioritization, which deliver better results when compared to other types of tree traversals.

Chapter 5 concludes the thesis and highlights our plans for future research work.

2   Background and Related Work

In this chapter we will explain how the propagation of sound is calculated and we will provide an overview of the existing literature. We will discuss the category of methods called geometrical acoustics and we will expand on the concept of wave-based geometrical acoustics backing it up with relevant existing work, that counts in for several physical phenomena.

2.1   Calculating the Propagation of Sound

2.1.1   Sound Theory

Sound is a form of mechanical vibration. A sound wave is a transfer of energy through the fluctuation of acoustic pressure as the wave travels away from a vibrating source. Sound waves are formed when a vibrating object causes the surrounding medium to vibrate. A medium is a material (solid, liquid or gas) which waves travel through. As a given object vibrates or oscillates in the medium, for example in the air, the air molecules near or around the vibrating object will be moved back and forth. This energy then travels through the air as a pressure wave. As sound waves move through a medium the particles vibrate forwards and backwards. The medium's particles themselves do not travel.
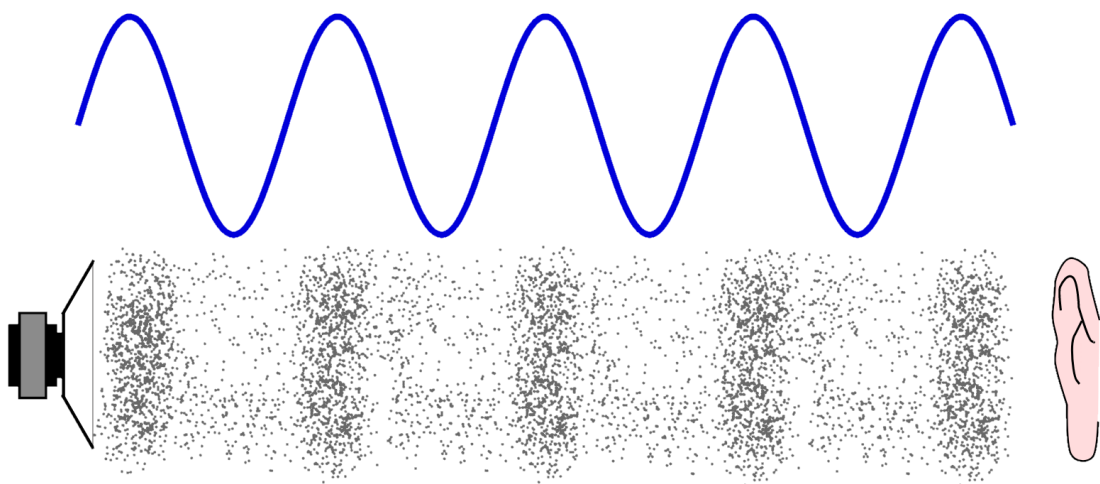
Figure 1. Pressure difference in air molecules as sound travels through the air.

The particles are moved back and forth in relation to the frequency and force of the vibration. If the vibration is strong and slow, the sound will be loud (high volume) and low in pitch; if the vibration is weak but fast, the sound will be soft (low volume) and high pitched.

By transferring energy away from a vibrating source, and propagating through any given medium, solid gas or liquid, the sound waves reach our ears and brain, where the information is stored, decoded and interpreted.

2.1.2   Sound wave equation

The equation that describes the movement of waves is known as the wave equation. It was presented by d'Alembert in 1746 (Kuttruff, 2007) and assuming 1-dimensional propagation of a sound wave, is described as below:

$$\frac{\partial^2 p}{\partial t^2} = c^2 \frac{\partial^2 p}{\partial x^2}$$

Equation 1: The sound wave equation for 1-dimensional propagation.

Where p is the pressure created due to particles vibration, at distance x from the origin of the vibration, after elapsing t time from the beginning of the vibration. c is the speed of sound.

For the scope of this thesis, we are concerned in a solution of the equation that provides the acoustical pressure of monopole spherical wave sources. A monopole is a source which radiates sound equally well in all directions. Such a solution is provided by the following equation (Salomons E. , 1997) which can be used to compute the pressure of sound $p_r(f)$ produced by a wave with f frequency, at distance r from the source.

$$p_r(f) = p_1(f) \frac{e^{jkr}}{r}$$

Equation 2. Pressure at distance r and frequency f

Where f is the frequency of the sound wave, k is the wavenumber, r is the distance from the source to the receiver and $p_1(f)$ is the sound pressure at one unit of distance from source.

2.2   Geometrical Acoustics vs Numerical Methods

Currently, methods for sound rendering are grouped into two major categories, based on their methodology. These are a) geometrical acoustics and b)numerical solutions (Charalampous & Michael, 2014).

Geometrical Acoustics (GA) methods are those methods that use rays to describe the propagation of sound waves. GA is the prevailing category of methods used for sound rendering due to its faster execution time. Sound rendering using GA can be divided into two major sub processes. These are a) the simulation of sound propagation through space and b) the generation and reproduction of the appropriate audio.

The biggest and most computationally expensive part of sound rendering using GA is the detection of sound rays propagating throughout a three-dimensional space i.e. how sound travels through space.

Sound propagation calculation results into an estimation of an impulse response (IR). An impulse response is the output of a given system, i.e. the structure of the 3D environment is fed with a Dirac pulse as an input and the impulse response is calculated as the output. An impulse is given as an input and it is a signature of the characteristic behavior of that system. The impulse response is the result of the propagation of sound from one point to another within a given environment.

After the impulse response is calculated, it is convolved with an anechoic signal, which is a signal that has been recorded without any spatial effects. The result of the calculation is an audio signal, which resembles how the sound would be heard in the simulated model at a given position.

Numerical solutions are methods which subdivide the environment into elements for solving the wave equation. They include methods for calculating partial differential equations like the Finite Element Method (FEM), the Boundary Element Method (BEM) for the time-independent Helmholtz equation and the Finite Differences Time Domain (FDTD) for the time-dependent wave equation (Vorlander, M, 2010). These solutions are computationally expensive, and their performance is not comparable with GA making them unusable for many practical scenarios like large spaces and high frequencies. Numerical solutions are out of the scope of this thesis.

2.3   The Wave-Based Geometrical Acoustics Model

In our work, the approach we follow in calculating the propagation of sound in three-dimensional spaces is the Wave-Based Geometrical Acoustics (WBGA). GA as a group of techniques that represent the propagation of sound as a propagation of rays throughout space, typically ignore the wave properties of sound, simplifying the problem from a problem of calculating the change of sound pressure to a problem of calculating the energy transmission throughout space. WBGA is an approach that keeps the principle of representing the propagation of sound as a ray, however, it uses equations that consider the wave nature of sound and allow the calculation of several wave-based phenomena, thus delivering pressure-based results. As a result, the calculation results are close to the results of numerical methods while maintaining the efficiency of geometrical acoustics techniques, by using fast path tracing methods.

2.3.1   Sound signal reproduction

The purpose of any sound rendering system is the reproduction of an audible sound signal that simulates the soundscape of a virtual environment. The construction of the audible two-channel (stereo) sound signal can be described at an abstract level by the following equation (Vorlander, 2010).

$$H|_{left,right} = \sum_{i=1}^{n} p_s * IR_i * HRTF(\theta, \varphi)|_{left,right}$$

Equation 3: Sound signal reproduction

Where $H|_{left}$ is the sound signal to be reproduced by the left channel, $H|_{right}$ is the sound signal to be reproduced by the right channel, n is the total number of wave-fronts arriving at a receiver, p is the sound pressure of a dry-recorded sound of a sound source s, IR_i is the impulse response of wave-front i and $HRTF(\theta, \varphi)|_{left,right}$ is the head-related transfer function of each ear at an inbound angle (θ, φ) where θ and φ are the polar and azimuthal angles from the receiver's horizontal plane (Vorlander, 2010). If the output needs to be computed for a different channel configuration, e.g. 5.1 or 7.1, the above equation is adjusted accordingly by computing an H for each channel. For

example, HRTF functions will not be relevant any more since their function is not relevant to 5.1 or 7.1 reproduction.

As derived from the above the solution, a geometrical acoustics model includes two important and complex subtasks a) detecting the sound paths in a three-dimensional environment for counting in the solution the n wave-fronts arriving at the receiver and b) calculating the impulse response IR for each of these wave-fronts.

2.3.2   Impulse Response Calculation

As mentioned above, the most common task of a sound propagation software is the calculation of the impulse response variable in the above equation, since the dry sound pressure and the HTRFs are usually given as an input (Vorlander, 2010). In GA, the estimation of the impulse response of an environment is calculated by considering that sound propagates as a ray. In this case, the task becomes easier as the impulse response can be given by analytical solutions like the following

$$IR = F_f{}^{-1}\left[\frac{e^{jkr}}{r}\prod_{z=0}^{n}C_z\right](t)$$

Equation 4. IR Calculation

Where IR denotes the impulse response of a specific wavefront, $F_f{}^{-1}$ the inverse Fourier transform of the result from the frequency domain to the time domain, $\frac{e^{jkr}}{r}$ the attenuation of the sound pressure due to spherical spreading, j the imaginary number, k the wavenumber, r the ray length from source to receiver, n the total number of coefficients calculating the effect of respective sound phenomena affecting the sound ray and C the coefficient which represents the effect of each phenomenon on the sound ray. The calculation of such coefficients is presented and explained in Chapter 3.

Since our calculations take place in the frequency domain, the component of interest becomes the following

$$p_r(f) = \frac{e^{jkr}}{r}\prod_{z=0}^{n}C_z$$

Equation 5. Transfer Function Calculation

Where $p_r(f)$ is the sound pressure for the specific frequency f at distance r from the source of the sound.

In the paragraphs below, we elaborate on the relevant literature on sound rendering and the calculation of sound propagation using geometrical acoustics.

2.3.3 Sound Path Detection

An integral part of the sound signal reproduction equation (Equation 3) is the detection of n wavefronts arriving from the source of the sound to the receiver. In this section, we explain briefly how the sound path detection task can be described as a tree traversal problem and we classify the available literature in the subject based on the way each method improves the way this tree traversal problem is solved.

2.3.3.1 *Sound Path Propagation as a Tree Traversal Problem*

Huygens-Fresnel principle states that the form of a wave is the summation of secondary waves created from point sources on the wave-front (Kuttruff, 2007). If the field is homogeneous and isotropic, the wave propagates toward a direction determined by the source's geometry. For example, point sources generate spherical waves, line sources generate cylindrical waves and surface sources generate plain waves. Waves alter their propagation behavior as soon as a discontinuity in the field occurs. Impedance discontinuities cause new wave fronts to be created and propagated throughout the space. The new wavefronts are caused by sound reflections or sound diffractions. In the case of non-homogenous or non-isotropic fields, other phenomena occur, like sound refraction. The additional sound waves can be modeled using new sound sources. From now and on, we will call these new sound sources as "*secondary sound sources*" (Figure 2). Practically, all surfaces and edges in an environment are potential secondary sound sources which emit sound received from other sources.
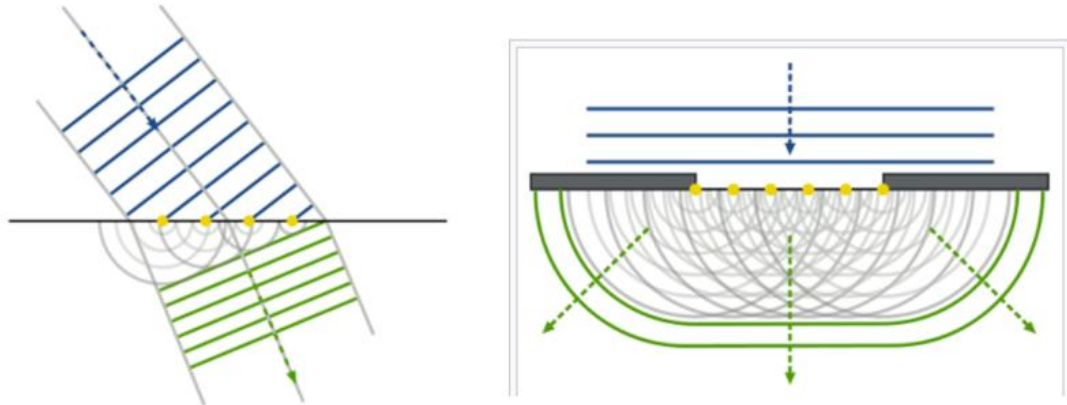
Figure 2. The refraction (left) and diffraction (right) phenomena based on Huygens-Fresnel principle. The yellow circles are the secondary sound sources.

As described above, a wave propagating in an environment with impedance discontinuities, i.e. reflecting surfaces and occluding obstacles, generates secondary waves. Similarly, secondary waves propagate throughout the space interacting in turn with the reflecting and occluding objects, which create new waves. These interactions continue in a recursive way, until the energy carried by the waves becomes negligible. As mentioned earlier, GA is the method used to describe sound as a ray phenomenon. Therefore, the propagation of waves is modeled as propagation of rays. This allows modeling waves generated by impedance discontinuities with the use of *virtual sources*. In a similar way that a propagating wave generates secondary waves when interacting with reflecting and occluding obstacles, a sound source generates *virtual child sources* representing these interactions. Extending this approach, virtual child sources create their own child sources, resulting in a tree of sound sources that models the sound field.

In computational terms, the possible virtual sound sources can be represented with the use of a tree structure. Following on, we will concentrate on virtual sources generated by reflecting surfaces, called *image sources*. Nevertheless, the same principles apply for diffracting edges too. The image source method is extensively documented in literature, thereupon we will focus on explaining the tree traversal nature of the problem.

Every sound source has a possible image source in each reflecting surface. The image source is computed by mirroring the parent source in the plane extending the reflecting surface (Figure 3). The source consists of the parent node in the tree and the

resulting image sources are the child nodes of that parent node. Recursively, each image source is considered as a parent node and higher order images are created as child nodes of this image source.
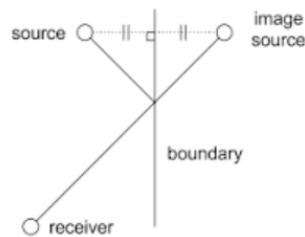
Figure 3. Creating an image source from a boundary.

This recursive process redounds to a tree of image sources that could affect the sound field. A typical implementation of an image source algorithm can be split into two major tasks a) the construction of the image tree b) the evaluation of the validity of each image. The first step (a) is described in the previous paragraph. Since most image source implementations deal with specular reflections only, task b deals with checking if the image source constitutes a valid sound reflection. The validity conditions of each image source are described in detail by Mechel (Mechel F. P., 2002). Implementations incorporating sound diffractions have also been proposed (Charalampous & Economou, 2016).

In principle, the calculation of the sound field at a receiver position is the summation of sound arriving from all valid sources at the receiver and it is described by Equation 3. To find the valid sources that need to be considered for Equation 3, a tree traversal is required, during which each node is evaluated for its validity. In Figure 4 a simple 3D model composed of a source, a receiver and three surfaces are displayed and in Figure 5 the tree representing the image sources up to the 3rd order. A simple image source method traverses the entire tree and decides which sources are valid and which are not. In color we can see the valid image sources and in gray the non-valid image sources. The images are rendered at their geometrical location with the respective color representing their validity (Figure 5). We can also see the sound paths constructed by the valid images.
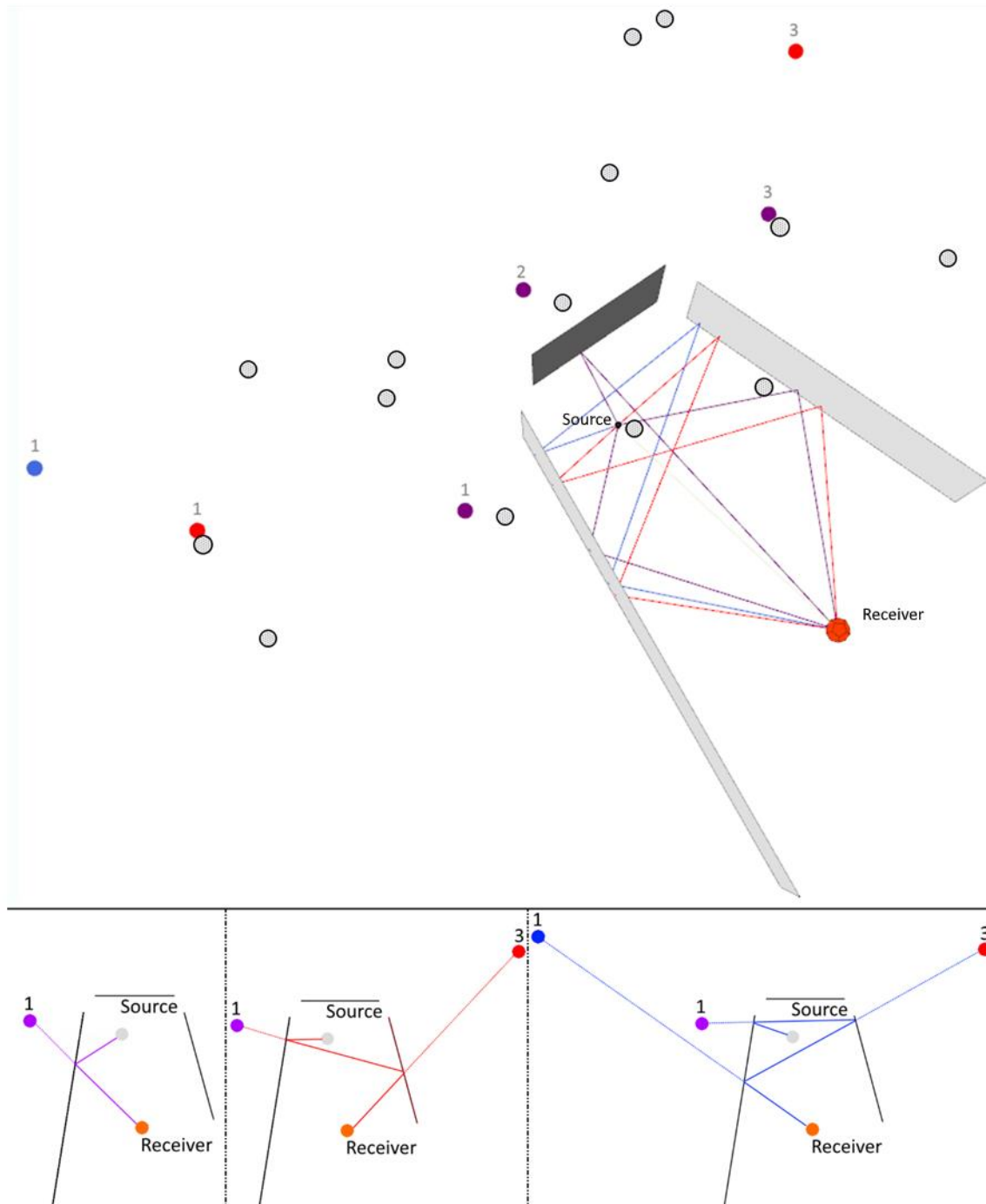
Figure 4. Reflections up to the 3rd order for a source-receiver configuration and three surfaces. The figure on top shows a typical configuration of a source and a receiver surrounded by three surfaces. The circles represent detected image sources. Colored image sources represent valid image sources while grey circles represent non valid image sources. The number above the valid image sources represents the surface from which the image source was generated. Surfaces are numbered in a clockwise manner from 1 to 3. The color represents the order of reflection. Purple paths represent 1st order reflections, red paths 2nd order reflections and blue paths 3rd

order reflections. The three images in the bottom depict the construction of one path for each order of reflection.
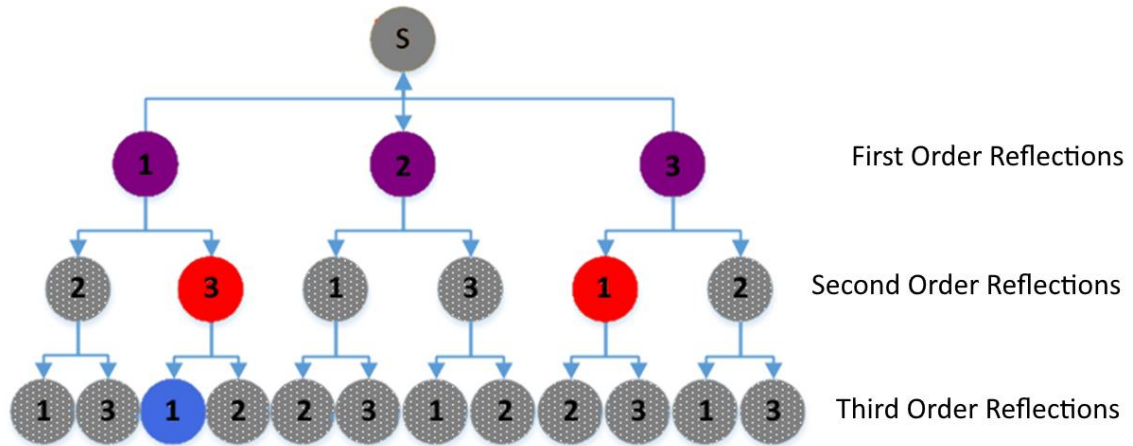
Figure 5: Tree representation of Figure 4. The nodes represent reflecting surfaces. Surfaces with valid image sources are in colored circles and surfaces with non-valid sources are in grey dotted circles. The number within each note denotes the number of the surface from which the image was generated.

We classify the related work in the field in a less common way. In contrast to previous studies, where sound rendering algorithms have been classified by the technique used (Charalampous & Michael, 2014), like image sources, beam tracing, ray tracing etc., we categorize these algorithms based on the way they handle processing to improve performance. The categories we propose are processing reduction algorithms, processing acceleration algorithms and processing prioritization algorithms. We chose this classification to show that prioritization algorithms have received less attention and that therein lies further potential in this type of algorithms. Following on, we describe each category in detail, and we elaborate on the relevant work.

2.3.3.2   Tree Pruning

Tree pruning algorithms are those algorithmic techniques that result in the reduction of the size of the tree, therefore improving execution times substantially. Most of the advances in sound propagation calculations fall under this category. Most notable techniques are ray tracing (Krokstad, Strom, & Sørsdal, 1968), visibility tracing (Mechel F. P., 2002), beam tracing (Funkhouser, et al., 2004) and frustum tracing (Chandak, Lauterbach, Taylor, Ren, & Manocha, 2008). All these techniques share the

same concept, that of tracing geometrical primitives through the 3D environment and detecting which geometrical objects are visible from other objects. By neglecting non-visible geometrical objects from further processing, the tracing results into a pruned tree, that includes only geometrically visible child-nodes. Visibility tracing and beam tracing result in an accurate pruning, where all visible objects are considered, unlike frustum and ray tracing, which might miss some visible objects. These techniques can be split into two major subcategories, deterministic tracing, and stochastic tracing.

Deterministic tracing is a category of algorithms that produce the same sound paths when ran multiple times. For example, a deterministic algorithm for detecting sound reflections in a given model detects the exact same reflection paths up to a given order of termination each time executed. The image source method and beam tracing are the main types of deterministic algorithms.

The image source method (Allen & Berkley, 1979), which falls within the deterministic tracing category, computes virtual sources by considering each polygonal surface in the environment as a reflector and mirroring in it, the location of the original source. Virtual sources can be used for the determination of reflection points, by finding the intersection of a line segment from the image source to the receiver. Then, the reflection points can be used for the construction of reflected sound paths. Virtual sources can be recursively mirrored, resulting in new virtual sources of higher order, therefore representing higher order reflections. The image source method is a method that provides accurate results, as it detects all the possible sound reflections in a 3D environment, but it suffers from poor performance. A simple image source algorithm has a growth of exponential complexity (Charalampous & Economou, 2013). It was first proposed by Alen and Berkley (Allen & Berkley, 1979) for rectangular rooms and was extended for arbitrary polyhedral (Borish, 1984). Since then, several improvements were suggested, like Vorlander's hybrid-ray tracing/image source implementation (Vorländer, 1989), Mechel's validity criteria (Mechel F. P., 2002), Schroder's binary space partitioning (Schröder & Lentz, 2006) and a generalized image source method based on spherical harmonics (Samarasinghe, Abhayapala, Lu, Chen, & Dickins, 2018).

Beam tracing is a method that has been borrowed from graphics and is based on image sources (Funkhouser, et al., 2004) (Laine, Siltanen, Lokki, & Savioja, 2009). During beam tracing, beams are cast throughout the 3D space (Funkhouser, et al.,

2004). Each beam is intersected with each polygon in the environment in a front-to-back order. After the intersecting polygons are detected, the beam is clipped, removing the shadow region. Then, a transmission beam is constructed by matching the shadow region and a reflection beam is constructed by using the image source method and mirroring the transmission beam over the polygon's plane. The use of beams is an effective way to accurately prune the tree of possible image sources, by only considering the visible leaves of each parent node. Beam tracing is currently considered as the fastest commonly used deterministic geometric room acoustics modeling technique (Laine, Siltanen, Lokki, & Savioja, 2009). Other developments in this area include the development of priority based beam tracing (Min & Funkhouser, 2000), bidirectional beam tracing, amortized beam tracing (Funkhouser, Min, & Carlbom, 1999), beam tracing using precomputed visibility diagrams (Antonacci, Foco, Sarti, & Tubaro, 2004), beam tracing using binary space partitioning (Laine, Siltanen, Lokki, & Savioja, 2009), multithreaded beam tracing (Sikora & Mateljan, 2013), as a part of hybrid models (Southern & Siltanen, 2013) and with the inclusion of refraction effect (Sikora, Mateljan, & Bogunović, 2012). Also, Markovic et al. present a 3D beam tracing based on visibility lookup for interactive acoustic modeling (Markovic, Antonacci, Sarti, & Tubaro, 2016). Sikora et al. combine beam tracing method with ray tracing method (Sikora, Russo, & Mateljan, 2018). Currently beam tracing methods are successfully used for modeling indoors and outdoors sound propagation (Wang, Cai, & Hongjun, 2019) (Wang, Gao, & Cai, 2019) as well as ocean acoustics (Porter, 2019).

Stochastic methods for sound propagation in 3D spaces are methods that use random sampling to achieve approximate representation of the sound field at the listener's location. In contrast with deterministic methods, stochastic methods provide results that may vary between executions and suffer from sampling problems but enjoy faster execution times. These methods are based on tracing the propagation of objects in an environment and their interaction with other entities like triangles, faces and edges. In terms of a tree traversal, stochastic tracing is the stochastic selection of paths in the tree, for which the visibility is determined by propagated objects. The propagated objects most used are rays, particles, and frusta.

Ray tracing is based on propagating rays throughout the environment by calculating ray surface intersections. Rays are emitted from the center of a sphere,

which represents the sound source location, and pass through a point on the sphere's surface which is obtained either by an equal distribution of points (Krokstad, Strom, & Sørsdal, 1968) or a statistical random distribution (Lehnert, 1993). Then, the rays are traced throughout the virtual environment until they reach the receiver or hit a surface. If they hit a surface, they become reflected, and the tracing continues until a termination criterion is met. When rays intersect with a receiver then the relevant energy impulses are recorded in the reflectograms. Ray tracing has been introduced in acoustics in 1958 (Allred & Newhouse, 1958). Krodstad has proposed the first algorithm using ray tracing to calculate impulse responses in rooms (Krokstad, Strom, & Sørsdal, 1968). Kulowski presented an improved algorithm for ray tracing which handles arbitrary room shapes (Kulowski, 1985). Vorlander used a combination of ray tracing and image source model to calculate acoustical impulse responses for rooms (Vorländer, 1989). Svensson outlines a brief history of the use of ray tracing techniques for sound propagation (Svensson & Krokstad, 2008).

The most recent developments in ray tracing for sound rendering include the development of hybrid algorithms combining ray tracing with frustum tracing and methods for artificial reverb estimation (Taylor M. T., Chandak, Antani, & Manocha, 2009), algorithms for the calculation of sound diffraction (Okada, Onoye, & Kobayashi, 2012), ray tracing using multi-view ray casting (Taylor M. , et al., 2012), ray tracing using acceleration structures (Dreher, Dutilleux, Junker, & others, 2012) ray tracing for higher order diffractions and diffused reflections (Schissler, Mehra, & Manocha, 2014) and bidirectional path tracing techniques (Cao, Ren, Schissler, Manocha, & Zhou, 2016). Ray tracing is also used in combination with artificial neural network techniques for the estimation of binaural impulse responses (Tenenbaum, Taminato, & Melo, 2019). Particle Tracing is a variation of the ray tracing technique (Bertram, Deines, Mohring, Jegorovs, & Hagen, 2005). In literature, it is presented as "phonon tracing" and "sonel mapping". Phonon tracing for acoustics has been proposed by (Jensen, 1996) and (Kapralos, Jenkin, & Milios, 2004) (Kapralos B. , 2006).

Frustum tracing is an approach that uses a simple volumetric representation based on a four-sided convex frustum; efficient algorithms are described that perform hierarchy traversal, intersection and specular reflection, and transmission interactions at the geometric primitives (Lauterbach, Chandak, & Manocha, 2007). Lauterbach et al.

(Lauterbach, Chandak, & Manocha, 2007) presented the first frustum tracing algorithms applied in sound propagation. Chandak et al. (Chandak, Lauterbach, Taylor, Ren, & Manocha, 2008) proposed an improved version of frustum tracing called adaptive frustum tracing which adaptively refines the quadtree to perform accurate intersection computations with the primitives in the scene and generate new frusta. Taylor et al. (Taylor M. T., Chandak, Antani, & Manocha, 2009) use frustum tracing to calculate sound diffraction in complex environments.

Other techniques also used in the reduction of the size of the tree are visibility computations. The performance of all proposed propagation methods, like image source, ray tracing and volume tracing algorithms is linked with the number of primitives under consideration. Hence, visibility computations are important for the reduction of the considered primitives. Chandak, Antani et al. (Chandak, 2011) (Chandak, Antani, Taylor, & Manocha, 2009) (Antani, Chandak, Taylor, & Manocha, 2012), who highlight the connection between these propagation techniques and the research on visibility computation in computer graphics and computational geometry, give a brief overview of visibility algorithms and apply some of these methods to accelerate geometrical acoustics.

2.3.3.3 Traversal Acceleration

Traversal acceleration algorithms are algorithms that improve the execution times of the tree traversal. These techniques deal with the reduction of the environment complexity, like visibility computations and preprocessing, as well as the exploitation of the hardware capabilities, like GPU acceleration.

Preprocessing information before the actual real-time propagation allows the reduction of required operations during run-time. Precomputation is used for the calculation of perceptual characteristics of the environment such as the perceptual importance of sound sources, for the reduction of the environment's complexity and the calculation of transfer factors. Tsingos (Tsingos, Gallo, & Drettakis, 2004) presents a method for the precomputation and perceptual assessment of spectral features of the input signals and also for precomputing geometry-based reverberation effects (Tsingos, 2009). Foale et al. (Foale & Vamplew, 2007) use precomputations for caching offline sound propagation calculations based on the portal subdivision method. Siltanen et al.

(Siltanen, 2010) as well as Drechsler (Drechsler, 2014) use precomputation for the reduction of the model's geometrical complexity. Raguvanshi et al. precompute impulse responses for complex scenes and interpolate in real-time for moving sources and receivers (Raghuvanshi, Snyder, Mehra, Lin, & Govindaraju, 2010).

Antani et al. (Antani, Chandak, Savioja, & Manocha, 2012) precompute the acoustic transfer operators using a technique similar to precomputed light transport. Stavrakis et al. precompute transport operators between coupled spaces connected by a portal to compute reverberation decay envelopes at interactive rates (Stavrakis, Tsingos, & Calamia, 2008) and Mehra et al. precompute transfer operators based on equivalent sources (Mehra, Raghuvanshi, Savioja, Lin, & Manocha, 2012). Another preprocessing function that could speed up calculations is the geometry reduction of complex 3D models to simpler ones containing only the acoustically relevant information (Siltanen, Lokki, Savioja, & Lynge Christensen, 2008). . Liu and Tan improve the performance of image source method by pre-computing the visibility of scene (Liu & Tan, 2016) and Zechen proposes a framework that that simulates ambient sound propagation in a preprocessing stage and reconstructs ambient sound efficiently at render time (Zechen, 2019). The main disadvantage of preprocessing methods is that they apply mostly for static scenes. In the case of dynamic environments, the preprocessing step needs to be repeated each time the environment changes.

Another approach in accelerating tree traversal is by taking advantage of the latest developments in hardware. For example, advancements in GPU technology have allowed the use of GPUs for general-purpose computing, also known as GPGPU. Hamidi and Kapralos (Hamidi & Kapralos, 2009) as well as Tsingos and Jiang (Tsingos, Jiang, & Williams, 2011) provide an extended overview of the use of GPUs for spatial sound in virtual environments and games. More specifically, GPU technology has been used extensively for geometrical acoustics calculations (Jedrzejewski & Marasek, 2006) (Röber, Kaminski, & Masuch, 2007). Tsingos and Gascuel (Tsingos, Gascuel, & others, 1997) use GPU for sound visibility calculations. Tsingos also exploits hardware capabilities to efficiently calculate sound scattering (Tsingos, Dachsbacher, Lefebvre, & Dellepiane, 2007). Rober et al. map acoustic equations to graphics rendering equations to take advantage of graphics programming technologies (Röber, Kaminski, & Masuch, 2007). Cowan and Kapralos (Cowan &

Kapralos, 2010) use GPU acceleration for fast acoustical occlusion modeling. Beig et al. propose a GPU-Based voxel graph path finding technique for spatial audio rendering in games and virtual reality (Beig, Kapralos, Collins, & Mirza-Babaei, 2019). Besides GPU acceleration, other hardware acceleration techniques are also used, like the use of SSE instructions for Intel processors (Chandak, 2011).

2.3.3.4 Traversal Prioritization

Traversal prioritization is another group of techniques that improves the performance of geometrical acoustics. Traversal prioritization is the concept of intelligently prioritizing the traversal of the tree, in such a way that the ratio of the visited valid nodes over the total visited nodes is increased. This way more valid nodes are discovered during the same amount of time. Work on this field has been presented by Min and Funkhouser (Min & Funkhouser, 2000) and Charalampous and Michael (Charalampous & Michael, 2014), (Charalampous & Michael, 2016) (Charalampous & Michael-Grigoriou, 2018). Koutsouris et al. (Koutsouris, Brunskog, Jeong, & Jacobsen, 2013) also apply termination criteria based on the radiation densities of the walls, a technique that can be interpreted as a prioritization of the traversal as well. As seen here, the amount of research regarding this type of performance improvement is significantly smaller than the rest, indicating that the subject might not have been exhausted. Based on this fact, we focused our research on investigating further the possibility of prioritizing tree traversals in an intelligent way.

2.3.4   Calculating Sound Phenomena using Ray Models

The second complex subtask of a GA method is the calculation of the impulse response of a sound path by calculating the attenuation and phase shift due to various acoustical phenomena encountered during propagation. Energy-based GA methods are limited to calculating the attenuation of sound energy while WBGA methods can calculate the attenuation of sound pressure as well as shifts in the phase of the sound wave. The most important phenomena are the reflection of sound, due change of impedance between two media, the diffraction of sound around edges of obstacles and the attenuation of sound, due to absorption and changes in the medium of propagation. In this case, atmospheric absorption and atmospheric refraction are the mentioned absorption and the change in the medium of propagation, respectively.

2.3.4.1 Sound Reflection

The effect of sound reflection on a sound path is added to the path's sound pressure by multiplying by a factor R, which corresponds to the reflection coefficient. The equation is extended as follows

$$p_r(f) = p_1(f)\frac{e^{jkr}}{r}R$$

Equation 6: The extended equation of computing sound pressure, considering reflection phenomena

The calculation of R is explained in detail in Chapter 3 however the main component affecting the calculation of R is the impedance of the sound material. Several models have been proposed for the calculation of material impedance. Delany and Bazley propose a simple model for porous materials using flow resistivity (Delany & Bazley, 1970). Attenborough proposes a two-parameter model for calculating sound impedance (Attenborough K. , 1992). Attenborough and Waters-Fuller propose a model for calculating the effective impedance of rough porous ground surfaces (Attenborough & Waters-Fuller, 2000). Atalla and Sgard attempt to calculate the impedance of perforated plates and screens (Atalla & Sgard, 2005) (Atalla & Sgard, 2007). Allard and Atalla described a porous layer as a mixture of air and an elastic frame, which could be modelled through some non-acoustical parameters, such as the bulk density, the fiber density, the Prandtl number of the air movement, the thermal characteristic length, and some elastic coefficients (Allard & Atalla, 2009). Berardi and Iannace suggest a model for calculating material impedance for natural materials (Berardi & Iannace, 2015) and an inverse method to predict the acoustical properties of nine natural fibers (Berardi & Iannace, 2016).

2.3.4.2 Sound Diffraction

In a similar manner to sound reflection, the effect of sound diffraction on propagated sound is calculated. Explicit diffraction calculations attempting to calculate or at least approximate the diffraction component of the sound path have been proposed by several authors. Exact frequency-domain, contour-integral expressions have been proposed by Macdonald (Macdonald, 1915), Oherhettinger (Oberhettinger, 1954), Bowman and Senior (Bowman & Senior, 1969), and Hadden and Pierce (Hadden & Pierce , 1981).

Corresponding exact time-domain solutions have been proposed by Biot, Tolstoy and Medwin (Biot & Tolstoy, 1957) (Medwin, 1981) and extended for finite edges by Svensson et al (Svensson, Fred, & Vanderkooy, 1999).

Approximate and asymptotic methods based on the Kirchhoff approximation have been proposed by Trorey (Trorey, 1970) (Trorey, 1977), Embleton (Embleton T. W., 1980) and Sakurai and Nagana (Sakurai & Nagata, 1981). Geometrical Theory of Diffraction (GDT) (Keller, 1962) and Uniform Theory of Diffraction (UTD) (Kouyoumjian & Pathak, 1974) are also approximate methods of calculating the effect of sound diffraction and Pierce (Pierce, 1974) proposes a method based on them. Further methods have been proposed by Vanderkooy (Vanderkooy, 1991), Menounou (Menounou, Busch-Vishniac, & Blackstock., 2000) and Stephenson and Svensson (Stephenson & Svensson, 2007). Calamia (Calamia, 2009) provides a comprehensive review on the subject. More recently, Kleshchev proposes some methods of solution of problems of sound diffraction on bodies of non-analytical form (Kleshchev, 2016), Menounou and Nicolaou present an analytical model for predicting edge diffraction in the time domain (Menounou & Nikolaou, 2017), Rodriguez et al. suggest a uniform theory of diffraction (UTD)-based solution for sound diffraction caused by an array of obstacles (Rodriguez, Pascual-Garcia, Martínez-Inglés, Molina-Garcia-Pardo, & Juan-Llácer, 2017) and Ouis proposes a solution for the diffraction of a spherical wave by a hard half-plane (Ouis, 2019).

2.3.4.3 Atmospheric Effects

Atmospheric conditions also play an important role in the propagation of sound waves. Sound passing through the air loses energy due to a phenomenon known as atmospheric or air absorption. Air absorption formulas are found in many acoustics textbooks and are described in the next chapter of this thesis (Attenborough, Li, & Horoshenkov, 2007) (Salomons E. , 1997). The sound field is also modified by atmospheric turbulence and atmospheric refraction, which are observed when the atmosphere becomes inhomogeneous. Clifford and Lataitis present a model for calculating turbulence effects on acoustic wave propagation over a smooth surface (Clifford & Lataitis, 1983). Ostashev et al. extend this model by using the paravolic equation method (Ostashev, Clifford, Lataitis, Blanc-Benon, & Juve, 2000). Several ray models for calculating sound propagation in inhomogeneous mediums are proposed. L'Esperance et al. devised

a model, which includes the effects of turbulence, atmospheric absorption, geometrical spreading, the ground effect and refraction for linear sound speed profiles (L'Esperance, Herzog, Daigle, & Nicolas, 1992). Salomons developed a model to include logarithmic and power profiles (Salomons E. M., 1994) and combine the ray model with theories of caustics (Salomons E. M., 1998). For upwind conditions and cases where the receiver is located in the shadow zone, Pierce proposes a residual method (Pierce, 1994), later improved by Berry & Daigle (Berry & Daigle, 1988) and West et al (West, Walkden, & Sack, 1989). Lam suggests an alternative analytical solution that includes turbulent scattering in the shadow zone (Lam Y. W., 2009). More recent developments include models that calculate the effect of atmospheric attenuation on a propagation outdoor noise (Ocansey & Bikdash, 2016), models that adapt transfer functions to changes in atmospheric conditions (Heuvhek, Caviedes-Nozal, Fernandez-Grande, Brunskog, & Agerkvist, 2019) and ray-based models for calculating multiple diffraction in a downward refracting atmosphere (Wolfgang & Lars, 2019).

2.3.4.4 *Wave Based Geometrical Models*

Geometrical acoustics models that maintain some of the characteristics of the wave propagation have been presented in the past, although with several limitations. The image source method presented by Allen & Berkley (Allen & Berkley, 1979) uses pressure summation, hence it is able to reproduce interferences, but it is limited to rigid walls with infinite impedance. Lam introduces the term Wave Based Geometrical Acoustics and proposes the use of spherical wave reflection coefficients (Lam Y. W., 2005). However, his model is limited to sound reflections and does not consider sound scattering caused by sound diffractions. Jeong el at. present a phased beam tracing method for the simulation of enclosed sound fields, however their model is limited to reflections and approximate reflection coefficients which are calculated based on absorption coefficients (Jeong, Jeong, & Rindel, 2008). Aretz et al. apply pressure-based summation and spherical wave reflection coefficient to the image source algorithm but their model is limited to rectangular rooms (Aretz, Dietrich,, & Vorländer, 2014).

3   Improving Geometrical Acoustics Using Wave-Based Equations

In this chapter we describe how by using wave-based equations, we can improve the calculation results of geometrical acoustics methods. We focus on our contribution to assemble a general method that could take an arbitrary 3D geometry as input and calculate the transfer function, with substantial accuracy improvements when compared to other widely used models based on geometrical acoustics and energy based equations. We present relevant wave-based equations used in other published ray models for various acoustic phenomena and we use them in our algorithms for accurately detecting sound paths traveling throughout the 3D space, which are then used to assemble a general calculation model that allows accurate acoustic predictions for arbitrary 3D geometries. Our contribution is focused on creating algorithms for detecting sound paths in arbitrary geometries and detecting the relevant information required by wave-based equations like angles of incidence, angles of reflection and angles of diffraction. Then, we present our published research findings on using our calculation engine to predict measurement results and theoretical expectations.

Our new model introduces the following advances in calculating the attenuation of sound pressure from a sound source when compared to traditional geometrical acoustics ray models

 a. Coherent pressure-based summation of sound paths using complex numbers.
 b. Spherical wave reflection coefficient using material impedance.
 c. Analytical solutions for sound diffractions over multiple wedges.
 d. Fresnel correction for finite-sized surfaces.
 e. Consideration of attenuation/amplification due to atmospheric absorption and atmospheric refraction.

To accomplish the inclusion of the above calculations into a general calculation model, we have developed novel algorithms which detect

 a. Multiple sound diffractions from parallel edges.
 b. Paths that combine reflections and diffractions.
 c. Refracted paths from refracting atmospheres.

As explained in Chapter 2, wave signals are governed by Equation 1 and this is also the case of our model which is a WBGA solution. Calculating Equation 4 is the objective of

this chapter, so we present a model that computes the required equation variables when given a 3D model consisting of meshes and surface materials e.g. the distance a sound path travels, angles of incidence and other variables required in the C_z components of the equation. This chapter is subdivided into sections describing the calculation process of each acoustical phenomenon and sections presenting projects where the efficiency of our new calculation model was evaluated when used to predict sound measurements in different contexts and compared with other solutions. The phenomena considered by our model are a) sound reflections b) sound diffractions c) atmospheric phenomena.

3.1 Reflections

When a sound wave is propagating through a medium e.g. air, and encounters a boundary with another medium e.g. a solid material, then two things happen, a part of a wave is reflected and another part is refracted/transmitted through the other medium (Kuttruff, 2007). Sound reflections are responsible for the most important alterations of the sound fields like sound amplification, room reverberation, resonances, echoing and many more. Transmission of sound through solid structures is generally neglected in current geometrical methods (Savioja & Svensson, 2015) and is not a part of the presented calculation model.

To be able to calculate the effect of sound reflection in a three-dimensional environment using geometrical methods, we need to abstract the sound wave as a ray, which is hitting on a surface and reflecting to the environment. A geometrical model that aims to calculate the effect of sound reflections on the sound field has two high-level tasks

1. Detect the sound paths emitted from sound sources, reflect on surfaces, reach the receiver, and gather all relevant geometrical information like the distance and the angles of incidence of each path on each surface.
2. Calculate the attenuation/amplification as well as the phase shift caused by the reflection of the sound path on the surface by considering the geometrical properties of the sound path and the material properties of the reflecting surface.

In the subsections that follow, we introduce our path detection algorithm for reflections, and we explain the existing methods used in our model to accomplish the tasks described above.

3.1.1   Reflection Detection

To calculate the sound pressure caused by sound reflection at a specific receiving point using the equations provided above, one needs to detect all the sound paths that travel from a point source to the receiver. As described in 2.3, there are several methods to achieve this. These methods belong in two large categories a) deterministic image source variants and b) stochastic tracing algorithms. A detailed presentation of these methods can be found in 2.3.3. In our case, we chose to base our reflection detection algorithm on the image source method, which falls in the deterministic algorithms' category, for the following reasons

- **Completeness**. The image source method can detect all reflected sound paths in any given 3D environment compared to other methods, like ray tracing variants that might miss some sound paths.
- **Accuracy**. The image source method provides accurate information about the 3D properties of each sound path, like the distance between source and receiver as well as angles of incidence. This is necessary for correctly calculating sound effects caused by sound interference, like room modes.
- **Determinism**. The image source method yields the same calculation results after any execution. This is of importance when considering the use of the model for engineering applications.

Knowing that the pure image source method a computationally expensive algorithm and that it is not practically usable for large models and high reflection orders, we were inspired by Mechel (Mechel F. P., 2002) for improvements in the performance speed. Below our new proposed method and the improvements, we introduced are explained in detail.

3.1.1.1   The Image Source Method

The image source method is a simple recursive method that attempts to replace sound waves with image source created by the reflection of each source, and subsequent image sources by a reflecting plane. This recursive process is depicted in Figure 4. As seen in Figure 5, the process can be abstracted using a tree structure. Again, we outline in brief the steps to create the image source tree, below

a. A source/image source is mirrored in a plane while extending a reflecting surface and the location of the image source is detected.

b. The sound path is created by joining the reflection point with the source and the receiver, and then the image source is checked for its validity. The necessary validity criteria are the following

　　1. The reflection point falls inside the reflecting surface.

　　2. No other objects obstruct the sound path.

c. The image source is added to the tree.

d. The process is repeated for each detected image source and image sources are detected up to a user-specified order of reflections.

We can easily conclude that following this iterative procedure for several orders leads to a huge tree of image sources, increasing exponentially the computational effort to compute all the applicable valid paths. To reduce the number of evaluated image sources, we have incorporated validity criteria in our algorithm, which we describe in the following sections. A detailed explanation of the image source method and the relevant formulas required can be found in (Allen & Berkley, 1979) and (Mechel F. P., 2002).

3.1.1.2　Visibility Matrix

Mechel outlines the first criterion for rejecting an image source, which is called the inside criterion. Mechel says that

> *"The first criterion for the generation of a daughter MS at a wall is that the mother source irradiates the interior surface of that wall. As a consequence, if a source is outside a wall, it does not create a daughter source at that wall".*

Rephrasing Mechel, we can say that an image source will send the sound wave only on the reflecting direction of the surface. Figure 6 helps in visualizing this criterion.
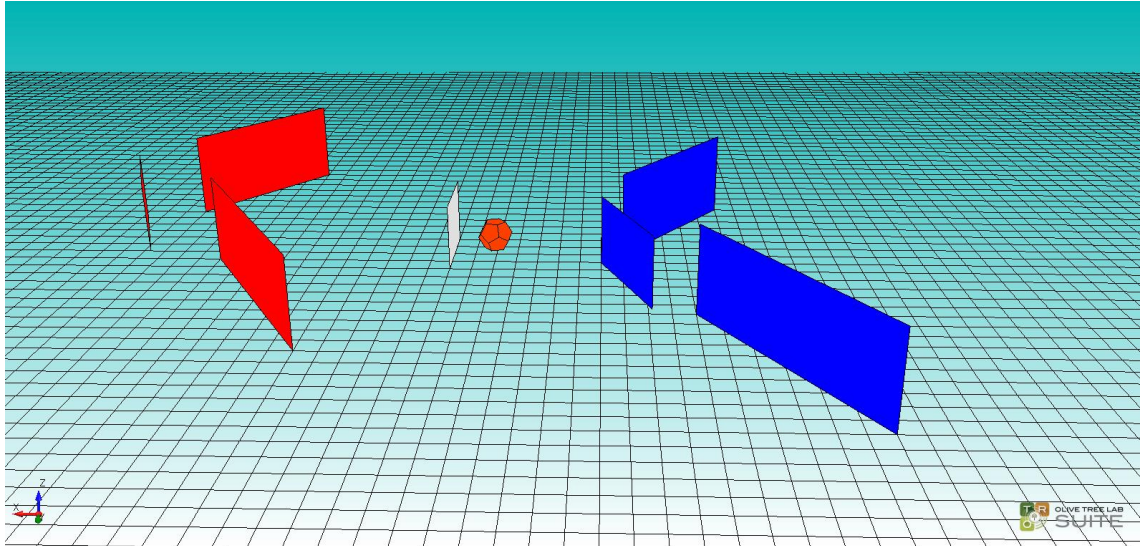
Figure 6. Red surfaces are on the visible side of the image source while blue surfaces are on the invisible side

In Figure 6, we can see the hypothetical location of the orange image source reflecting from the grey surface. In this case, the reflected path constructed by this image source can only send the reflected sound to the surfaces in red color. Contrariwise, if the image source was located on the opposite side of the grey surface, it would only consider reflections on the blue surfaces. Therefore, irrespective of the exact location of the image and depending on which side of the surface the image is, it can only reflect sound toward the surfaces on the reflecting side of the image source.

This fact allows us to limit the tree search scope even before we start detecting image sources. This could be achieved by constructing a visibility matrix between the surfaces. A visibility matrix is a matrix that allows us to store the visibility of each surface in relation to the sides of all other surfaces. A small example of a visibility matrix is demonstrated in Table 1.

	Surface 1	Surface 2	Surface 3
Surface 1	N/A	1	0
Surface 2	1	N/A	0
Surface 3	1	0	N/A

Table 1. A visibility matrix showing the visibility between surfaces

The first column is the list of the available surfaces. The rest of the columns store a value that indicates in which side of the surface normal is the surface under consideration located, e.g. 0 if is on the negative side and 1 if it is on the positive side. This table can be constructed before the initiation of the tree traversal. During the construction of the image tree, only surfaces that are on the opposite side of the image source normal are included, e.g. an image source is created for Surface 2 on the positive side of the plane's normal. For this image source, we will only consider Surface 3 since Surface 1 is on the same side of the normal as the image source.

3.1.1.3 Visibility Beams

The second validity criterion that we are introducing is inspired by Mechel's field angle criterion and it evaluates the visibility of a child image source surface from the parent source. In this case, an image source can only be considered if its surface is within the visible angle of the parent surface. To check if an image is within the angle, Mechel proposes a number of checks, however his checks are approximate and leave out image sources, since the criterion for exclusion of a wall as mirror wall is if the wall's center is inside the field angle cone of the parent source (Mechel F. P., 2002, p. 885). This criterion excludes mirror walls that might have valid image sources, but their center is outside the field angle cone. Such an example can be taken from his first experiment on a concave wall, where for the first three orders of diffraction he detects a total of 77 image sources (Mechel F. P., 2002, p. 888) while the original image source method detects 82.
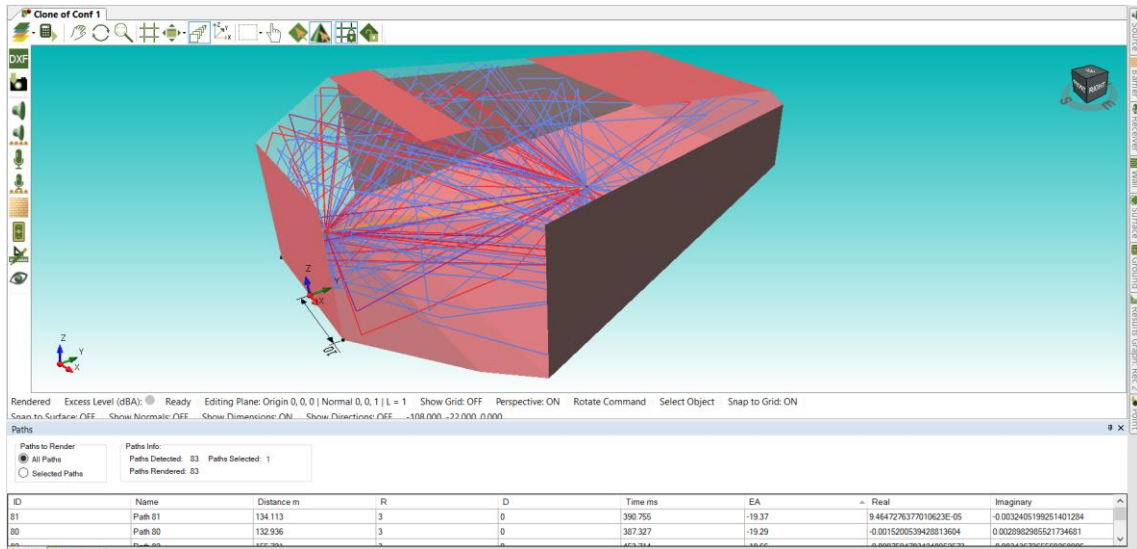
Figure 7. Mechel's concave room simulated in Olive Tree Lab using a simple image source method. One direct path is detected and 82 reflected paths. For the same setup, Mechel reports only 77 image sources.

Therefore, we used a more conservative approach in discarding non-valid images. The method consists of the following high-level steps

1. We take the image source of the reflecting surface and the two points of each edge on that surface and we create a plane (Figure 8).
2. We run step one for all edges of the surface, and we end up with a collection of planes with their normal facing outwards of the surface.
3. For a surface not to be considered for the generation of a child image source, it needs to be behind two or fewer planes. If it is behind three or more planes, it is considered for generating a child source.
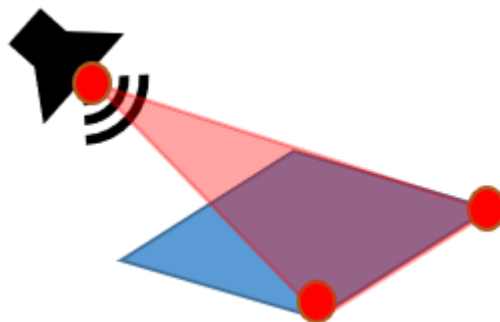
Figure 8. Creating a plane from a source and two surface points

Figure 9 represents an example case in a 3D representation. We have the image source of the green surface in orange color. We have the surfaces, which are discarded from subsequent image source detection, in red color. We can see the surfaces, that fulfill the visibility criterion and are kept for further image source detection, in yellow color.
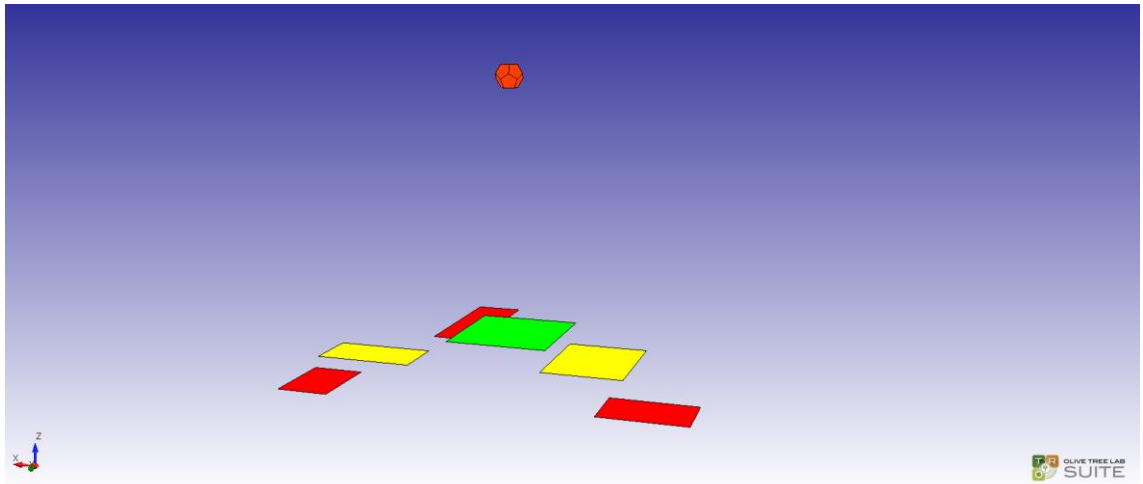
Figure 9. Example of surface selection using visibility beams. In green is the surface of the image source. Red surfaces are discarded from subsequent image source detection. Yellow images are kept for further image detection.

Figure 10 shows a top-down view of the same configuration. We can clearly see that surfaces in red are outside the visibility beam created by the image source and the surface in green. For the two yellow surfaces, the one on the left is clearly inside the visibility beam, however, the yellow surface on the right is not. Nevertheless, it fulfills the criteria laid out above hence kept for further check. Based on this we can see that this method can generate false positives. However, the validation overhead is substantially lower than more accurate methods like beam tracing which requires time-consuming geometrical operations to check if the beam intersects with the surface.
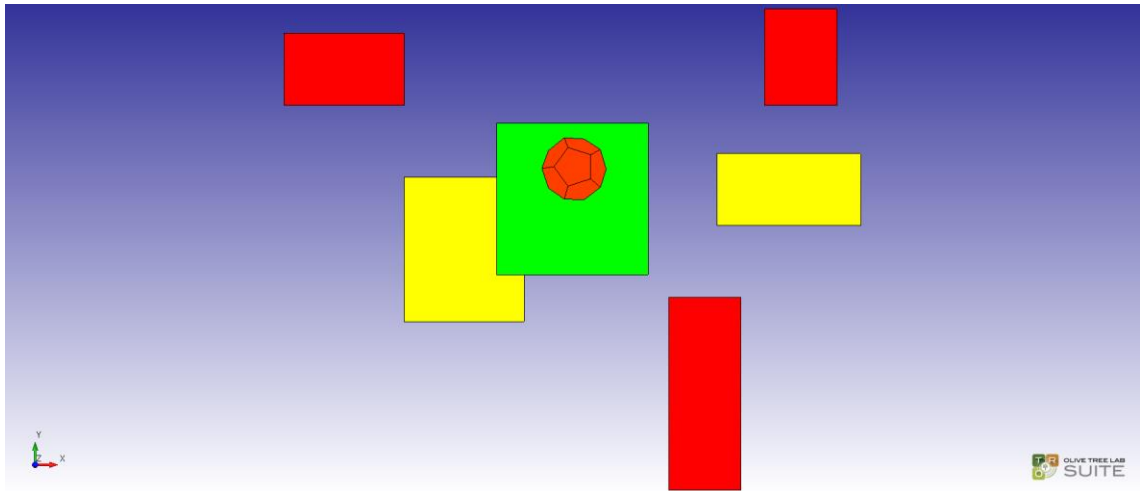
Figure 10. Top-down view of Figure 4 example.

3.1.1.4 *Performance Improvements*

To demonstrate the performance improvements of the visibility matrix and visibility beam, we ran a simple experiment. We used the 3D model of the geometry structure shown in Figure 11 and we detected sound reflections up to the 2nd, 3rd and 4th order using three different methods a) image source without speed up b) image source using visibility matrix c) image source using visibility matrix and visibility beam.
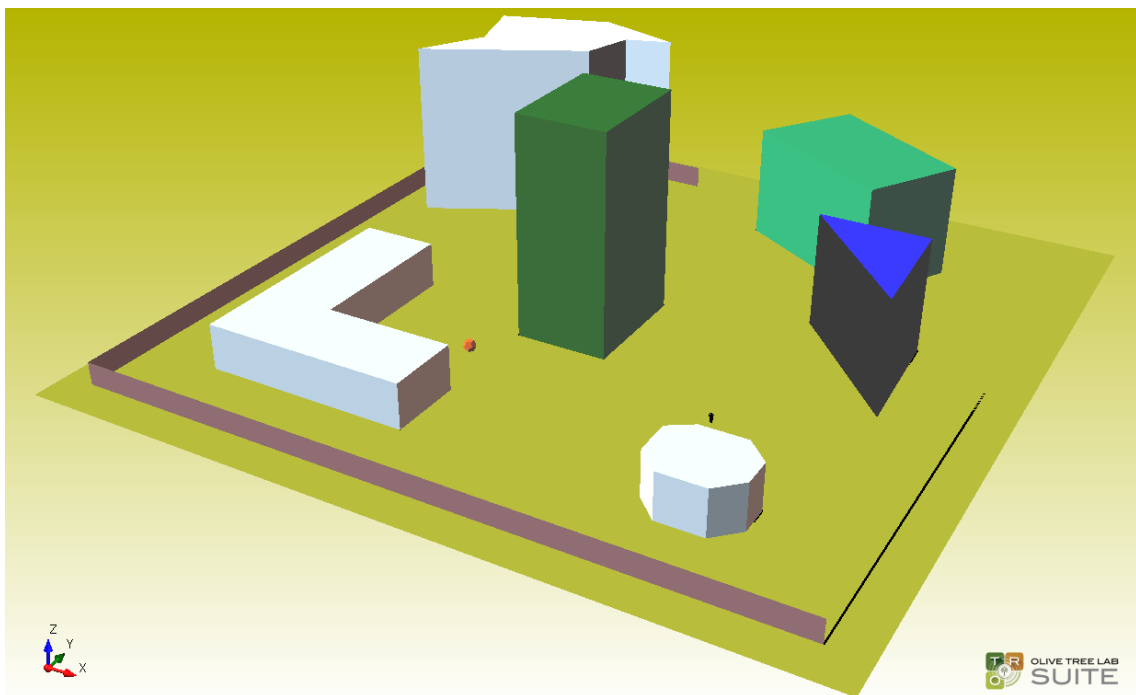
Figure 11. The model used for validating image source performance improvements

In Table 2 we can see the number of image sources examined in each case. We can notice the significant reduction in the number of image sources examined when compared to an image source implementation without any speed up additions while there is no compromise in calculation accuracy since all implementations detect the exact same number of sound paths[1].

Reflection Order Sound Path Detection Method	2	3	4
Image Source with No Speed Up	8.836	821.842	76.431.400
Image Source using Visibility Matrix	7.404	531.102	35.900.739
Image Source using Visibility Matrix & Visibility Beam	7.407	109.818	1.395.955

Table 2. Images detected for each case and reflection order.

3.1.2   Reflection Calculation

In our calculation model, the equation for calculating the sound pressure at a receiver for a reflected sound path is the following (Vorlander, M, 2010)

$$p(f) = p_1(f) \frac{e^{jkr}}{r} R$$

Equation 7

Where

---

[1] For 2nd order reflections the number of images is the same for Visibility Matrix Only case and Visibility Matrix & Visibility Beam case. This happens because for 1st order reflections there is no Visibility Beam check, as there isn't for last order image sources (in this case 2nd order) since it takes less time to check the validity of the source than construct a visibility frustum. Hence, the two cases become equivalent.

$$p_1(f)$$

is the sound pressure of the source measured at 1 meter.

$$\frac{e^{jkr}}{r}$$

denotes the attenuation of a spherical wave's sound pressure due to spherical spreading with k being the wave number and r the distance in meters covered by the sound path.

$$R$$

is the coefficient of interest and represents the factor of the attenuation of sound due to the absorption from the sound material. When the sound path reflects on more than one surface, the equation becomes.

$$p(f) = p_1(f) \frac{e^{jkr}}{r} \prod_{z=0}^{o} R_z$$

Equation 8

The reflection coefficient is a value dependent on θ, that is representing the angle of incidence of the sound path. In common energy-based GA techniques, the absorption coefficient a is used to calculate R using the following equation

$$R(\theta) = \sqrt{1-a}$$

Equation 9

Since absorption coefficient is an energy-based variable, we need to use the square root to revert it back to pressure, however in this case the phase information is lost.

Most GA techniques skip the calculation of the absorption coefficient, due to the scarcity of information about material impedances, and use absorption coefficients obtained from measurements. However, the use of absorption coefficients leads to the loss of phase information since absorption coefficients are represented in real instead of complex numbers. Thus, they are not suitable for our model since all wave effects caused by the reflection of sound on materials are lost. Instead, we need to use $R(\theta)$ to retain the phase information in our calculations. Therefore, in our model we are using an analytical way to calculate the reflection from materials using the material properties i.e.

the material's flow resistivity, for which we could obtain a database with data sufficient for most of the cases examined in this thesis.

We use the following equation

$$R(\theta) = \frac{Z_s \cos \theta - \rho c}{Z_s \cos \theta + \rho c}$$

Equation 10

Where Z_s is the impedance of the surface and ρc denotes the impedance of air (Salomons E. , 1997). For the calculation of Z_s we use the model presented by Delany and Bazley (Delany & Bazley, 1970). The expression used is the following

$$Z = R_2 + iX_2$$

Equation 11

Where

$$\boldsymbol{R_2 = 1 + 9.08(f/c)^{-0.75}\rho c}$$

Equation 12

and

$$X_2 = 11.9(f/c)^{-0.73}\rho c$$

Equation 13

Where f is the frequency of the sound wave.

Equation 7 gives us the solution for the reflection of a plane wave on an infinite, flat and smooth surface with local reaction material. Further on we extend our solution to finite surfaces. Also, diffraction calculation, presented later, can be used to model surface anomalies. To take account of spherical waves, we apply the Weyl-van der Pol approximation (Lam & Monazzam, On the modeling of sound propagation over multi-impedance discontinuities using a semiempirical diffraction formulation, 2006) for spherical wave reflection coefficients and Equation 7 becomes

$$p(f) = p_{1(f)} \frac{e^{jkr}}{r} Q(\theta)$$

Equation 14

Where

$$Q(\theta) = R(\theta) + (1 - R(\theta))F(w)$$

Equation 15

w is the numerical distance and $F(w)$ is the ground function calculated using the following expression

$$F(w) = 1 + i\pi^{\frac{1}{2}}w^{\frac{1}{2}}e^{-w}erfc(-i\sqrt{w})$$

Equation 16

To compute the sound pressure of a path that reflects on multiple surfaces, Equation 14 becomes

$$p(f) = p_{1(f)} \frac{e^{jkr}}{r} \prod_{i=1}^{n} Q_n(\theta)$$

Equation 17

Where n represents the respective reflection point

3.1.3 Finite Surfaces

To take into consideration the effect of finite-sized surfaces in our model, we use the model developed by Clay et al (Clay, Chu, & Li, 1993). Clay et al use Fresnel zones to calculate the amplitude of a wave reflecting on a rectangular surface of a finite size. Based on their model the equation for calculating the sound pressure of a path, reflecting on a finite surface becomes

$$p(f) = p_{1(f)} \frac{e^{jkr}}{r} Q(\theta)I(u_1)I(v_1)$$

Equation 18

54

Where

$$I(u_1) = \int_{-u_1}^{u_1} \exp\left(-i\frac{\pi}{2}u^2\right) du$$

Equation 19

And

$$I(v_1) = \int_{-v_1}^{v_1} \exp\left(-i\frac{\pi}{2}v^2\right) dv$$

Equation 20

And

$$u1 = \cos\psi\left(\frac{(R_1 + R_2)^{1/2}}{2\lambda R_1 R_2}\right)w_x$$

Equation 21

And

$$v1 = \left(\frac{(R_1 + R_2)^{1/2}}{2\lambda R_1 R_2}\right)w_y$$

Equation 22

Where R_1 is the distance of the sound path from the source to the reflection point, R_2 is the distance of the sound path from the reflection point to the receiver, w_x is the width

of the surface in the x dimension, w_y is the width of the surface in the y dimension and λ is the wavelength.
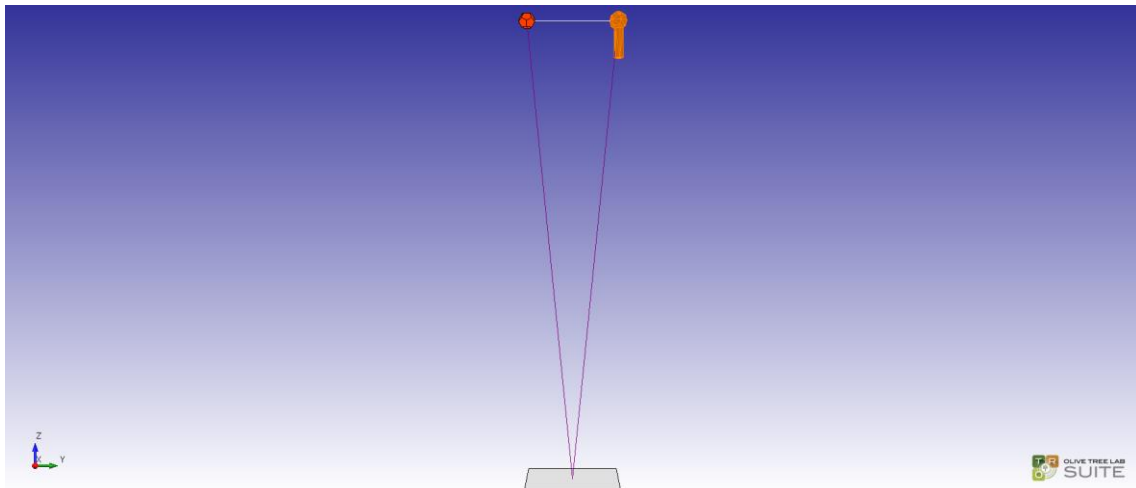
Figure 12. Finite Surface Setup

In Figure 13 we can see the comparison of the excess attenuation for a source and receiver setup, 10m above a 2x2m finite surface with and without finite surface corrections.

We can observe the difference in low frequencies indicating that the reflected surface has a minimum effect on lower frequency waves. The blue line represents the results without Fresnel corrections and the red line shows the results with the corrections taken into consideration. Also, we can see the fluctuations in higher frequencies. Our results agree with the expected results, based on Clay et al (Clay, Chu, & Li, 1993).

To demonstrate the differences of the various methods of calculating sound reflection, we created a simple setup with a source and a receiver over a surface of finite

impedance with a flow resistivity of 200kPas/m2. We show the differences in results for the following four sets of calculations. The four sets of calculations are

a. Plane wave reflection coefficient based on absorption coefficient and energy summation.
b. Plane wave reflection coefficient based on absorption coefficient and pressure summation.
c. Plane wave reflection coefficient based on impedance and energy summation.
d. Spherical wave reflection coefficient based on impedance and pressure summation.

Figure 14 shows the configuration on the left and the excess attenuation (EA) in dB on the right.
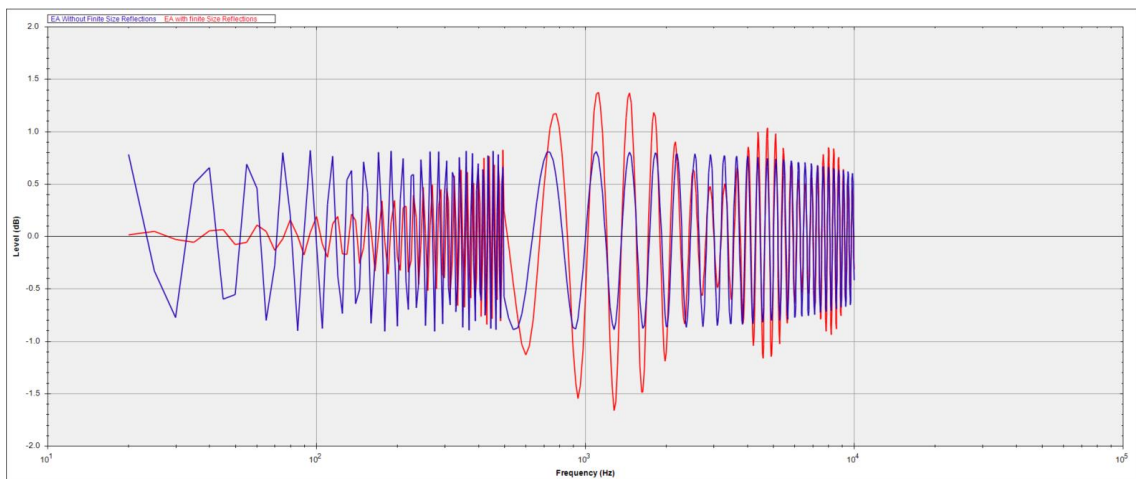
Figure 13. Comparison between calculations with and without Fresnel corrections
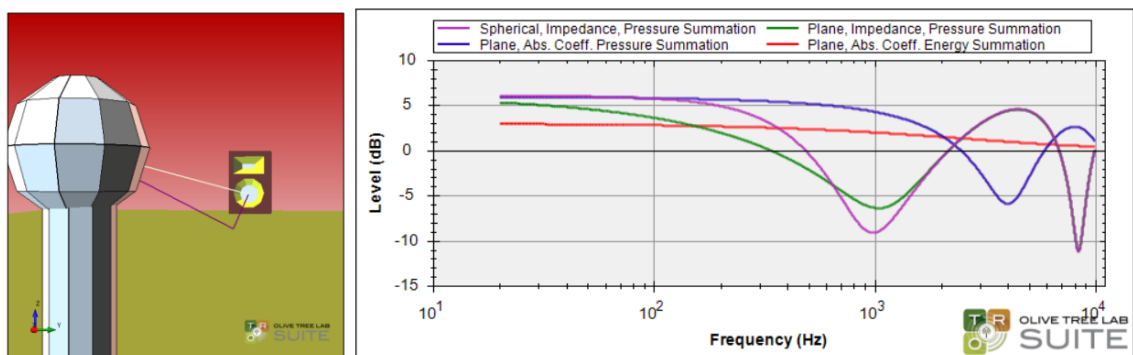
Figure 14. Comparison between different methods of calculating sound reflection from a surface.

From the results, it is obvious that energy summation redounds to complete loss of wave effects, like sound cancellation at certain frequencies. Another evident conclusion is that the use of absorption coefficient yields inaccurate results even with the use of pressure summation. The cancellation is shifted to higher frequencies, something that affects the outcome of the final calculation.

3.2 Diffractions

Diffraction is a component of the sound field, often completely neglected in most GA modeling methods or approximated at best (Calamia, 2009)

Several methods have been proposed for dealing with sound diffractions in 3D geometries. However, each of them bears with their own limitations. Tsingos et al. present a method based on beam tracing which is practical only for densely occluded and coarsely detailed 3D models, since beams get fragmented in scenes with many free-space cell boundaries (Tsingos, Funkhouser, Ngan, & Carlbom, 2001). Chandak et al use a frustum tracing technique that ignores the non-shadow part of the sound diffraction and can lead to inaccurate diffraction paths since the shape of the diffraction frustum may extend beyond the actual diffraction field that originates from the edge (Chandak, Lauterbach, Taylor, Ren, & Manocha, 2008). A ray tracing solution proposed by Okada et al. does not have the ability to find higher-order diffraction paths, which play significant roles especially in densely occluded scenes (Okada, Onoye, & Kobayashi, 2012). Schissler et al. propose a solution for higher-order diffractions, however, their approach loses some energy because combinations of diffraction and reflection are not computed (Schissler, Mehra, & Manocha, 2014).

In this section, we describe a new method for detecting and calculating the diffracted paths from arbitrary 3D geometries. Our diffraction model is based on the Geometrical Theory of Diffraction (GTD). GTD considers only sound paths were the angle of incidence equals the angle of diffraction. This results to only one ray being considered for the calculation of sound diffractions. Such ray models have been presented by Salomons (Salomons E. , 1997) and Min and Qiu (Min & Xiaojun, 2009). They both use the Hadden-Pierce solution for the calculation of the diffraction coefficient of each diffracting point. The diffraction coefficient can cause change in the sound pressure of the path as well as the phase. Our contribution is the introduction of a novel algorithm

for detecting diffracted sound paths to any order from collections of parallel edges, as well as a wave-based computational method based on recent research, which can be easily incorporated into our overall calculation method.

3.2.1 Diffraction Path Detection

Considering the limitations mentioned above, we had to develop a general method for detecting sound diffractions for any order and any 3D setup. For this thesis, a method for detecting sound diffractions from a set of parallel edges is described below. A more general method applicable for collections of non-parallel edges exists and successfully used in Olive Tree Lab but it has not been published yet and it is not used in the context of this thesis.

3.2.1.1 Calculating Diffracted Path from Multiple Parallel Edges

To calculate the diffracted sound path created by a single edge, we use Keller's law (Keller, 1962) which dictates that the angle of incidence of a diffracted path is equal to the angle of diffraction. Therefore, we can safely assume that the path can be represented by a line segment folded around an edge, forming angles of equal size between the edge and the two parts of the folded segment. To calculate the exact diffracting point that can be used to indicate where a hypothetical diffracted line segment, which is connecting the source and the receiver, will be folded over a diffracting edge, we use the method outlined in Figure 15 and described in the following steps.
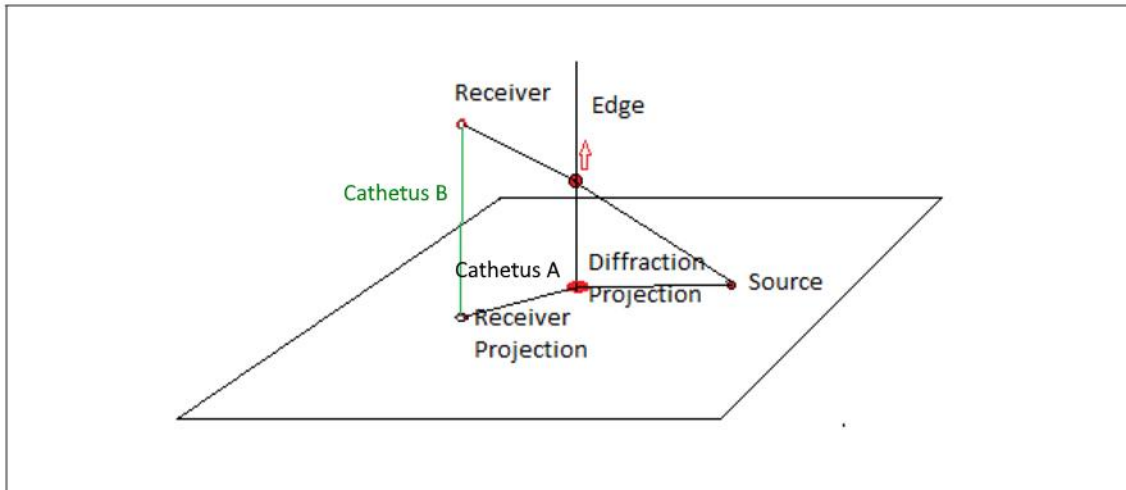
Figure 15. Calculation of diffracted paths.

a. We use the source location and the diffracted edge vector to define a plane that is perpendicular to the diffracted edge.

b. We define three points on the plane 1) the projection of the receiver 2) the projection of the diffracted point, this being the intersection of the diffracted edge with the plane 3) the projection of the source on the place, this being equal to the source location since the source is on the plane.

c. We add the distance between the source, the diffraction projection, and the receiver projection. This distance is considered as a cathetus (Cathetus A) of an imaginary right triangle.

d. The line segment connecting the receiver with its projection can be considered as the second cathetus (Cathetus B) of the triangle.

e. Using the proportion of the distance between the source and the diffraction projection, we can estimate the distance that the diffraction projection needs to move on the diffracted edge to meet the diffraction point.

This method can be easily extended to detect diffractions from multiple edges. To calculate the diffraction from multiple edges, we need to project all the diffracting points on the plane and calculate the projected path by adding the distances of the projected points in the sequence of the edges we want to examine. Since the edges are parallel, the plane is the same for all edges.

3.2.1.2 *Calculating Diffracted Path Visibility*

For the diffracted paths calculated in 3.2.1.1, we need to determine the visibility of the path. Two visibility checks need to take place a) a standard line of sight check, using a ray-triangle intersection as described in (Havel & Herout, 2010) b) pass-through-corner check. The pass-through-corner check is necessary since our method considers the adjacent surfaces of the wedge when calculating the sound paths. Therefore, the calculated paths might be passing through a wedge, thus an additional check is needed. Figure 16 and Figure 18 show two such cases, a valid sound diffraction bath and a non-valid one.

To determine if a diffracted point is passing through a wedge, we follow the process outlined below

1. On the plane formed by the diffraction point, the previous path point[2] and the next path point, we define a circle around the diffraction point, with a very small radius e.g. 1 mm, so that the two surfaces of the diffracting wedge are practically infinite planes at that scale.

2. On the circle defined in point 1, we place four vertices at a $\pi/2$ distance from each other.

3. For each point defined in point 2. we construct paths between the previous path point, the current point, and the next path point.

4. If even one of the paths constructed in 3 does not intersect with any of the wedge surfaces, the diffraction path does not pass through this wedge. If all four paths are obstructed by any of the two surfaces, then the diffraction path passes through the wedge.

5. To avoid issues with edge conditions, like the paths passing from the edge of the surface and obstruction not being detected, we rotate all points by 5 degrees and repeat the process from point 3. The path needs not to pass through the wedge, for the path to be considered as valid in both cases. Since there can be only one point on the circle from which a straight line connecting the circle point, the

---

[2] A path point can be any of the valid points on a path, these being a source, a receiver, a diffraction point, or a reflection point.

diffraction point and the next path point, this method is sufficient to cover all cases.

Figure 16 and Figure 17 provide a visual representation of this process
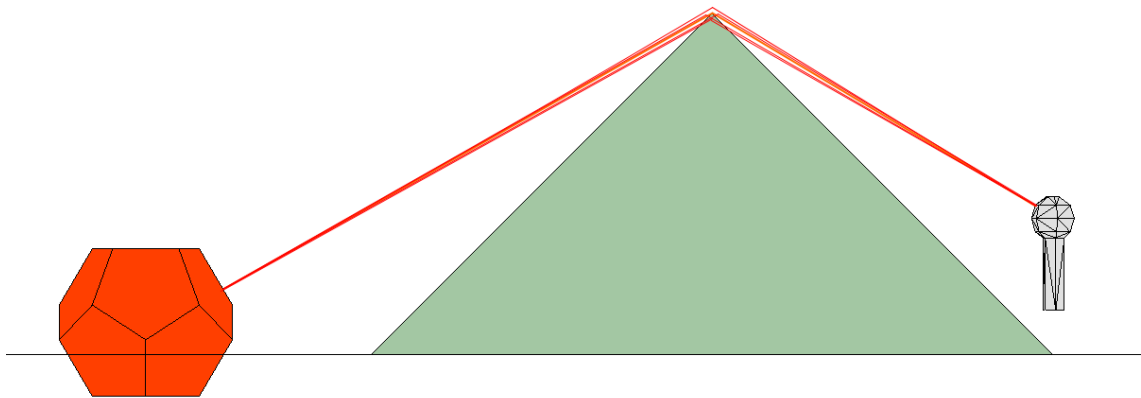
Figure 16. Diffracted path that does not pass through a corner

Figure 16 demonstrates the four sound paths in red, constructed around the actual sound path in orange. Figure 17 is the same as Figure 16when zoomed in around the diffraction point. This case represents a valid diffraction path since there is one red path, the one on top, that has line of sight visibility.
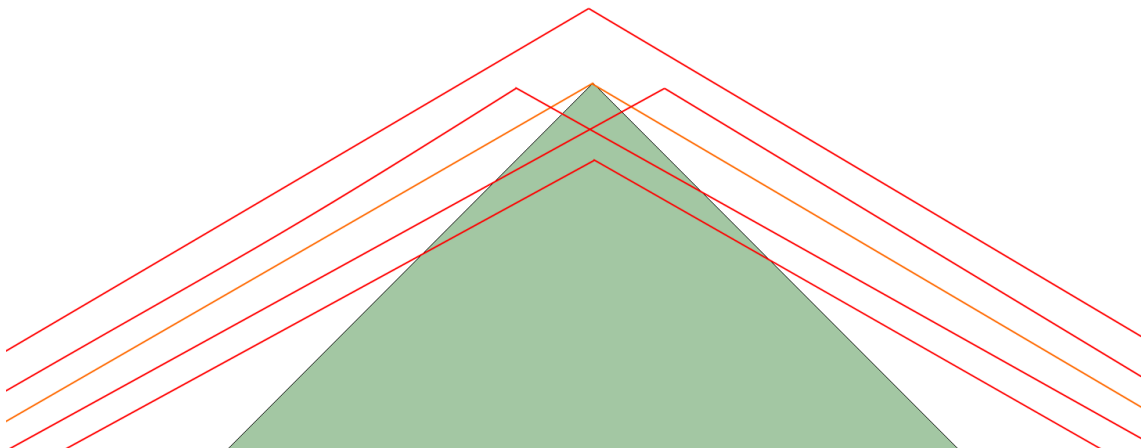
Figure 17. Zoom into **Figure 16**
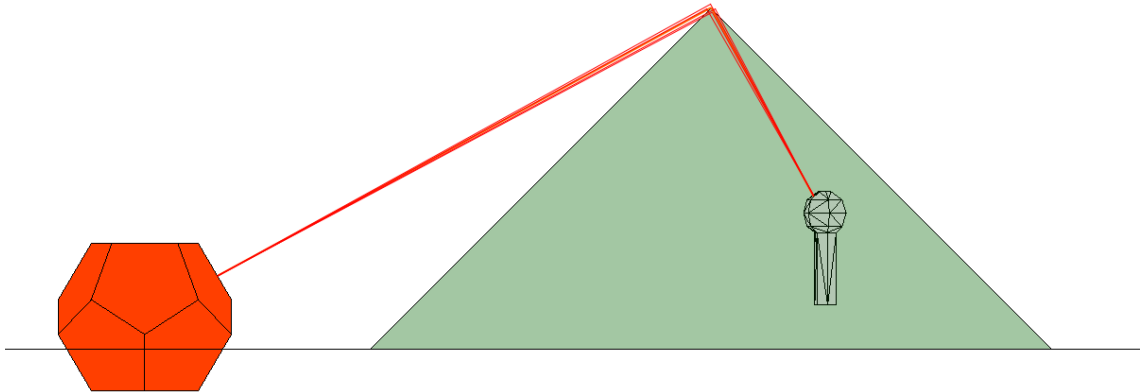
Figure 18. Path that passes through a corner

Contrary to previous figures, Figure 18 visualizes a case where a sound path is not valid as all four red paths are obstructed by a surface. The above procedure is applied in all diffracting points of a sound path.

3.2.2 Reflected-Diffracted Path Detection
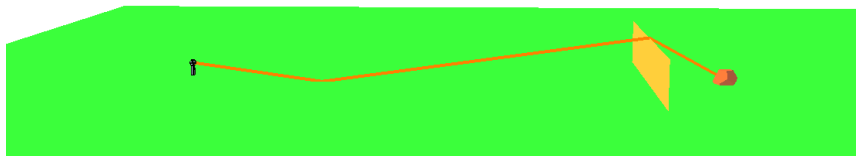
Figure 19. Reflected diffracted path over a sound barrier.

A sound path consisting of both a sound reflection and sound diffraction is a common scenario. An example is a sound path leaving a source, hitting the ground, and then crossing a barrier to reach a receiver. The configuration in Figure 19 demonstrates such a case.

A general solution for calculating all reflected diffracted paths would be to combine the methods described in 3.1.1 and 3.2.1 and obtain all possible reflected diffracted paths. Essentially, using the image source method we can extend the calculation to calculate bother the direct reflections caused by an image source as well as the sound paths created by the image source and diffract from the environment edges. However,

implementing such a general solution would expand drastically the required computation time for sound rendering making our method impractical. Therefore, we decided to implement a more limited method for our calculation engine that would be able to provide us with the most important reflected diffracted sound paths. Our method focuses on detecting reflected diffracted paths from edges that already have a diffracting path to the receiver since there is a higher probability for these edges to send reflected-diffracted sound paths to the received ones as well. Therefore, we first detect the diffracted paths and then we use the edges of the diffracted paths to check diffractions passing through these edges coming from image sources from nearby planes.

Our solution consists of the following high-level steps

1. We detect all diffraction paths in the 3D environment.
2. We construct a list of edges having a diffracting path.
3. For each surface in the environment, we find the mirror source and then perform the following checks for each edge of point 2
   a. We check if there is a diffracting path between the mirror source, the edge, and the receiver. If yes, we connect the source, the reflecting point where the path intersects the plane, the diffracting point detected on the edge and the receiver.
   b. We check if there is a diffracting path between the mirror source, the image of the edge and the receiver. If yes, we connect the source, the reflecting point where the path intersects the plane, the image of the diffracting point detected on the image of the edge (it should be located on the actual edge) and the receiver.

Figure 20 helps in visualizing the process described in 3a and 3b. In Figure 20 we can see the mirror source of the sound source in red created in the ground. Then, we can see the sound diffractions created by the mirror source, the edges, and the receiver. At the point where these sound diffractions intersect with the ground, a reflection point is

added and connected to the actual sound source.
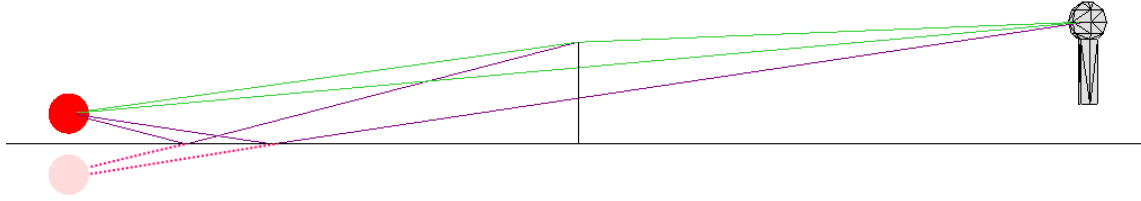
Figure 20. Reflected-diffracted path detection.

3.2.1 Diffraction Calculation

3.2.1.1 Diffraction from a Single Edge

To calculate the diffraction from a single diffracting, we use the solution of Hadden and Pierce (Hadden & Pierce , 1981). The equation for calculating the sound pressure of a path diffracting from a single edge becomes

$$p(f) = p_{1(f)} \frac{e^{jkr}}{r} D$$

Equation 23

Where D is the diffraction coefficient and is calculated using the following equation

$$D = -\frac{1}{\pi} \sum_{v=1}^{4} A(\Phi_n) F_v(A(\Phi_n)) Q_n$$

Equation 24

With F_v being the Faddeeva function and

$$A(\Phi_n) = \left(\frac{v}{2}\right)(-\beta - \pi + \Phi_n) + \pi H(\pi - \Phi_n)$$

$$v = \pi/\beta$$

$$\Phi_1 = \zeta$$

$$\Phi_2 = 2\beta - |\theta_r - \theta_s|$$

$$\Phi_3 = \theta_r + \theta_s$$

$$\Phi_4 = 2\beta - |\theta_r - \theta_s|$$

$$Q_1 = 1$$

$$Q_2 = Q_s Q_r$$

$$Q_3 = Q_r$$

$$Q_4 = Q_s$$

where $H(\pi - \Phi_n)$ is the Heaviside step function

$$H(x) = \begin{cases} 1 \ for \ x \geq 0 \\ 0 \ for \ x < 0 \end{cases}$$

Q_r and Q_s are the spherical wave reflection coefficients of the source side and received side surfaces, respectively.

And $\zeta, \beta, \theta_r, \theta_s$ are defined in Figure 21
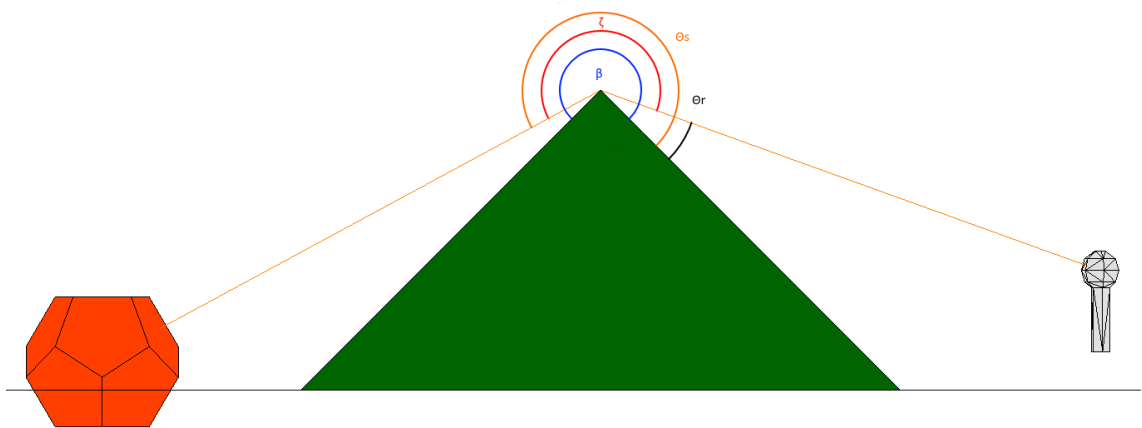
Figure 21. Diffracted path angles.

3.2.1.2   *Diffraction from Multiple Edges*

To extend the calculation described in the previous section to consider sound diffraction over multiple wedges, we use the work on Min and Xiaojun (Min & Xiaojun, 2009). In the case of multiple diffractions, Equation 12 becomes

$$p(f) = p_{1(f)} \frac{e^{jkr}}{r} \prod_{l=1}^{m} Da(E_{l-1}, E_l)$$

Equation 25

Where

$$a(E_{l-1}, E_l) = \begin{cases} 1 \text{ if the edges } E_{l-1} \text{ and } E_l \text{ are separated} \\ 1/2 \text{ if the edges } E_{l-1} \text{ and } E_l \text{ are connected} \end{cases}$$

And n is the number of diffraction points

3.2.2 Reflected-Diffracted Path Calculation

For calculating the sound pressure of a path consisting of both reflections and diffractions, Equation 16 and Equation 25 are merged to create the following

$$p(f) = p_{1(f)} \frac{e^{jkr}}{r} \prod_{i=1}^{n} Q_i(\theta) \prod_{l=1}^{m} Da(E_{l-1}, E_l)$$

Equation 26

Where n is the number of reflection points and m is the number of diffraction points

3.3 Atmospheric Phenomena

3.3.1 Atmospheric Absorption

When sound travels through the air, a part of the sound wave energy is lost due to absorption from the atmosphere. This happens because some of the energy is converted into heat as the wave propagates. The amount of energy lost is related to the temperature, humidity, and atmospheric pressure. To calculate the amount of sound pressure lost due to atmospheric absorption, we need to calculate the absorption coefficient. The absorption coefficient is given by the following equation (Salomons E. , 1997)

$$a = 8.686 f^2 \tau_r^{\frac{1}{2}} (1.84 \times 10^{-11} \rho_r^{-1} + \tau_r^{-3}[b_1 + b_2])$$

Equation 27

67

where $\tau_r = T/T_{20}$ and $\rho_r = p_r/p_r$ are dimensionless quantities, with T being the temperature in Kelvin, T_{20}= 293.15 Kelvin and $p_r = $ 101 325 Pa

b_1 and b_2 are given by

$$b_1 = 0.1068 \exp\left(-\frac{3352}{T}\right)/(f_{r,N} + f^2/f_{r,N})$$

Equation 28

$$b_2 = 0.01275 \exp\left(-\frac{2239.1}{T}\right)/(f_{r,O} + f^2/f_{r,O})$$

Equation 29

where $f_{r,N}$ and $f_{r,O}$ given by

$$f_{r,N} = \rho_r \tau_r^{\frac{1}{2}}(9 + 280h \exp(-4.17[\tau_r^{1/3}]))$$

Equation 30

$$f_{r,O} = \rho_r[24 + 40400h(0.02 + h)/(0.391 + h)]$$

Equation 31

With h being the molar concentration of water vapor in the atmosphere expressed as a percentage, given by the following equation

$$h = r_h\rho_{sat}/\rho_r$$

Equation 32

With r_h representing the relative humidity as a ratio of the water vapor pressure. ρ_{sat} is given by the following expression

$$\rho_{sat} = 10^{C_{sat}}$$

Equation 33

And

$$C_{sat} = -6.8346\left(\frac{T_{01}}{T}\right)^{1.261} + 4.6151$$

Equation 34

Where $T_{01} = 273.16\ K$ being the triple-point temperature of water.

Incorporating atmospheric absorption into our model Equation 26 becomes

$$p(f) = p_{1(f)} \frac{e^{jkr}}{r} a \prod_{i=1}^{n} Q_i(\theta) \prod_{l=1}^{m} Da(E_{l-1}, E_l)$$

Equation 35

3.3.2 Atmospheric Refraction

In the chapters and sections above, we described the abstraction of sound propagating in rays. The rays we draw assume a propagation in straight lines from one point to another. The straight lines assumption is safe if the atmospheric conditions are the same in the entire space under consideration or the distances are small. For sound propagation in outdoor environments and long distances, these assumptions do not hold true. In long distances there are variations in atmospheric conditions, affecting the propagation of sound waves, making the straight-line assumption to be false and calculations to yield unrealistic results. The cause of this behavior is the refraction of sound resulted from temperature and wind gradients.

To allow our geometrical model to deliver more accurate results for longer distances in outdoor conditions, we extended our calculations to consider sound refraction from temperature and wind gradients. For the case of a positive gradient and downward sound refraction we based our work on the ray model presented by L'Esperance et al. (L'Esperance, Herzog, Daigle, & Nicolas, 1992) and we extended it to consider obstructing structures by applying the relevant line of sight checks as well as to calculate sound paths that combine sound refraction and sound reflection. For the case of negative sound speed gradient and upward sound refraction, we used a method proposed by West et al. (West, Walkden, & Sack, The Acoustic Shadow Produced by Wind Speed and Temperature Gradients Close to the Ground, 1989). In the sections below we describe the two models in more detail.

3.3.2.1 Refracted Paths with Positive Gradient

Figure 22. Refracted paths from moderate positive diffraction.

The ray model proposed by L'Esperance et al. (L'Esperance, Herzog, Daigle, & Nicolas, 1992) allows the calculation of curvature of existing sound paths as well as the calculation of additional reflections resulting from the bending of the sound waves. Figure 22 shows the effect of moderate positive refraction with the bending of existing sound rays and Figure 23 shows the effect of strong positive sound refraction with the generation of new reflected sound paths.
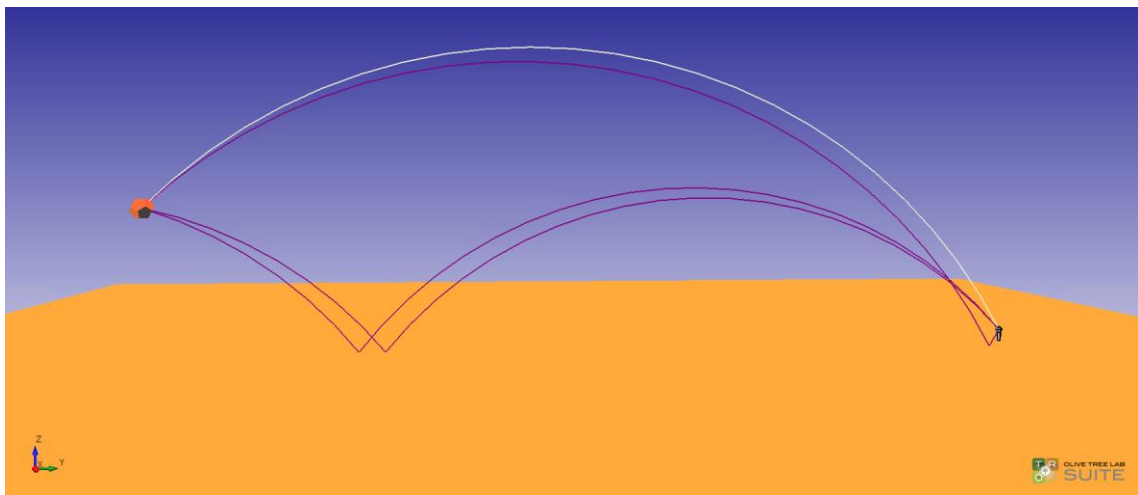
Figure 23. Refracted paths from strong positive diffraction.

To estimate the bending of the sound paths we need to calculate the sound speed gradient profile. The input parameters required to calculate a logarithmic sound speed profile in our model are: the temperature at ground level (T), the temperature at a height

z defined by the user, the wind speed $u(z_u)$ at a height z_u, the roughness constant (z_0) and the wind direction (φ) defined as the clockwise angle from the north with the downwind condition blowing from south to north.

In cases of a logarithmic sound speed profile the sound speed is described with the following equation (L'Esperance, Herzog, Daigle, & Nicolas, 1992)

$$c(z) = A\ln\left(\frac{z}{z_0} + 1\right) + Bz + c_0$$

Equation 36

Where A and B are given by

$$A = \frac{u(z_u)\cos\theta}{\ln\left(\frac{z_u}{z_0} + 1\right)}$$

Equation 37

$$B = \frac{dT}{dz}\frac{10.025}{\sqrt{T + 273.15}}$$

Equation 38

angle θ is the wind direction relative to the propagation of sound between the source and receiver and $\frac{dT}{dz}$ is the linear temperature gradient.

We approximate a logarithmic sound speed profile with a linear sound speed profile using the method proposed by Harmonoise (Plovsing, B; Kragh, J, 2006). This method involves finding the radius of curvatures of the logarithmic (A) and the linear (B) parts of the profile and combining them as follows

$$r_{A,B} = \frac{1}{\dfrac{1}{r_A} + \dfrac{1}{r_B}}$$

Equation 39

Where

$$r_A = sign(A)\frac{R}{8}\sqrt{\frac{2\pi c_0}{|A|}}$$

Equation 40

$$r_B = sign(B)\sqrt{\left(\frac{c_0}{|B|}\right)^2 + \left(\frac{R}{2}\right)^2}$$

Equation 41

The effective linear sound speed gradient can then be found using

$$a = \frac{1}{r_{A,B}\cos\varphi}$$

Equation 42

Where φ is given by

$$\varphi = \sin^{-1}\left(\frac{\sqrt{R^2 + (z_r - z_s)^2}}{2r_{A,B}}\right) + \tan^{-1}\left(\frac{z_r - z_s}{R}\right)$$

Equation 43

R is the horizontal range between the source and receiver while z_s and z_r are the source and receiver heights, respectively.

Having calculated the sound speed gradient, we can now calculate the curvature of the sound rays by finding the radius of an arc that is connecting the source and the receiver by using the following method:

1. We find a plane placed at a height z using Equation 44.
2. We project both source and receiver on the plane.
3. We find the center c of the arc circle using Equation 45.

$$z \begin{cases} \dfrac{\min(source\ height, receiver\ height)}{a} \ for\ a > 0 \\ \dfrac{\max(source\ height, receiver\ height)}{a} for\ a < 0 \end{cases}$$

Equation 44

$$c = (r_z{}^2 + sr_z{}^2 - s_z{}^2)/(2sr')$$

Equation 45

Where

r_z a vector from the receiver point to the projection of the receiver point on the plane

s_z a vector from the source point to the projection of the source point on the plane

sr_z a vector from the source point project to the receiver point projection on the plane

By having the vector c and the source and receiver locations, we can define an arc with c as the circle's center and estimate the length of the ray connecting the source and the receiver. The same process is also followed for estimating the reflected sound paths. In this case, the calculation of the curvature takes place between each pair of points, where the preceding point replaces the sound source, and the succeeding point replaces the receiver point.

In cases of moderate sound gradients, the reflection points are detected using the standard image source process. In cases of strong, positive sound gradients, additional reflection points might occur. These additional reflection points can be found using the following fourth-order equation (Embleton, Thiessen, & Piercy, 1976)

$$n(n + 1)x^4 - (2n + 1)Dx^3 + [b_R^2 + (2n^2 - 1)b_s^2 + D^2]x^2 - (2n - 1)b_s^2 Dx + n(n - 1)b_s^4 = 0$$

Equation 46

Where

$$b_i^2 = \frac{z_i}{a(2 + az_i)}\ for\ i = S\ or\ R$$

Equation 47

In Equation 46, n is the number of reflections and the unknown is the horizontal distance between the source and the first reflection at the ground. This equation must be solved for n = 0, 1, 2, 3... (the number of reflections at the ground), until there is no real solution for x, i.e. as long as 0 < x < D.

The model of L'Esperance et al. assumes propagation over the ground without any obstructions for the sound rays. We extend the model with line-of-sight checks between an arc and any surface in the 3D geometry. Figure 24 demonstrates the refracted paths between a source and a receiver over the ground without any obstructions.
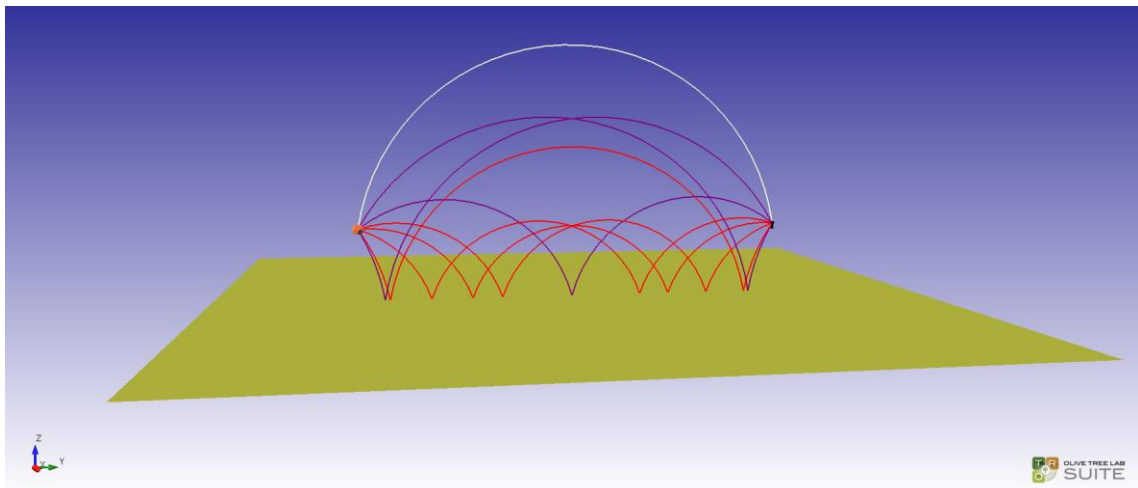
Figure 24. Refracted paths between a source and a receiver over the ground without any obstructions.
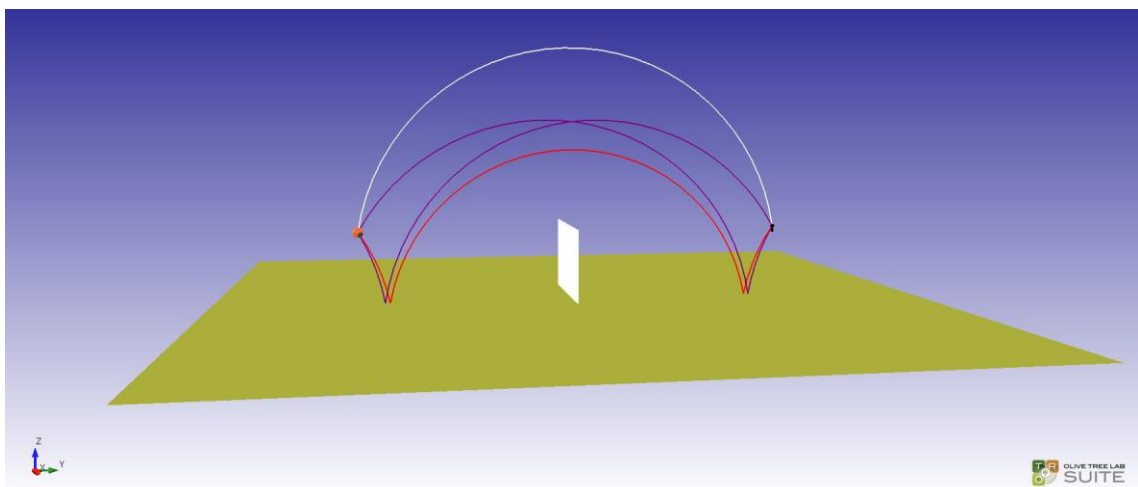
Figure 25. Refracted paths between a source and a receiver over the ground with obstructions.

In Figure 25 we can see the same setup with the inclusion of a sound barrier in-between the source and the receiver.

3.3.2.2 Refracted Paths with Negative Gradient

The same principles of physics apply when a sound speed gradient becomes negative. In this case, the sound paths will bend in an upwards direction. If nothing is obstructing the sound path from reaching the receiver, the same calculations as above apply. However, in cases of a strong negative gradient, the sound path is obstructed by the ground and no valid sound path reaches the receiver, even if the received is in an acoustical shadow zone. This happens when the gradient is negative, and the following condition is true

$$D > (2\frac{z_S}{a})^{1/2} + (2\frac{z_R}{a})^{1/2}$$

Equation 48

In this case, the ray model proposed by L'Esperance cannot be applied and we use the diffraction solution proposed by Berry and Daigle (Berry & Daigle, 1988). In this case, valid sound paths cannot be detected, and the sound pressure is evaluated by the following equation

$$P(r,z) = \frac{\pi e^{j\pi/6}}{l} \sum_n H_0^{(1)}(k_n) \times \frac{A_i\left[b_n - \left(\frac{z_S}{l}\right)e^{\frac{2i\pi}{3}}\right]A_i\left[b_n - \left(\frac{z_R}{l}\right)e^{\frac{2i\pi}{3}}\right]}{A_i'[b_n]^2 - b_n[A_i(b_n)]^2}$$

Equation 49

Where

$$b_n = \tau e^{i\pi/3} = (k_n^2 - k_0^2)l^2 e^{2i\pi/3}$$

Equation 50

Are the zeros of the expression

$$A_i'(b_n) + q e^{i\pi/3} A_i'(b_n) = 0$$

Equation 51

Where

$$q = \frac{jk_0\rho lc}{Z_G}$$

$$\tau = (k^2 - k_0^2)l^2$$

$$l = (R/2k_0^2)^{1/3}$$

$$R = 1/a$$

With

$$k_0 = \omega/c(0)$$

3.3.2.3 Calculating Diffracted-Refracted Paths

L'Esperance et al. sound refraction model presented above presents a method of calculating the effect of sound diffraction considering the presence of sources above a ground surface. The model yields satisfactory results for open plane setups where the line of sight between sources and receivers is not obstructed by any big obstacles. When obstructions occur between sources and receivers, then we need to account for sound refraction for diffracted sound paths as well.

Ourcontribution in this part is the extension of the sound refraction model to combine the diffraction detection algorithm presented in 2.3.4.2. To consider for sound refraction for diffracted paths, we apply the sound bending method explained in this section on diffraction paths located on a plane vertical to the ground. The steps applied are the following:

1. We detect the refraction paths as explained above.
2. We disregard the rays that intersect with obstructing objects.
3. We detect sound diffraction paths around the obstructing objects.
4. For sound diffractions that are located on a vertical plane to the ground, we apply the sound bending calculation to the points of the sound path and we bend the paths accordingly.

Figure 26 demonstrates such a case. In this figure we can see a source, a receiver and a barrier occluding the direct path between them. We can also see the refracted sound paths that reach the sound receiver. The refracted sound paths that were intercepted by the barrier are neglected. The path that was diffracted from the top

edge of the barrier was bent according to the sound speed gradient of the environment.
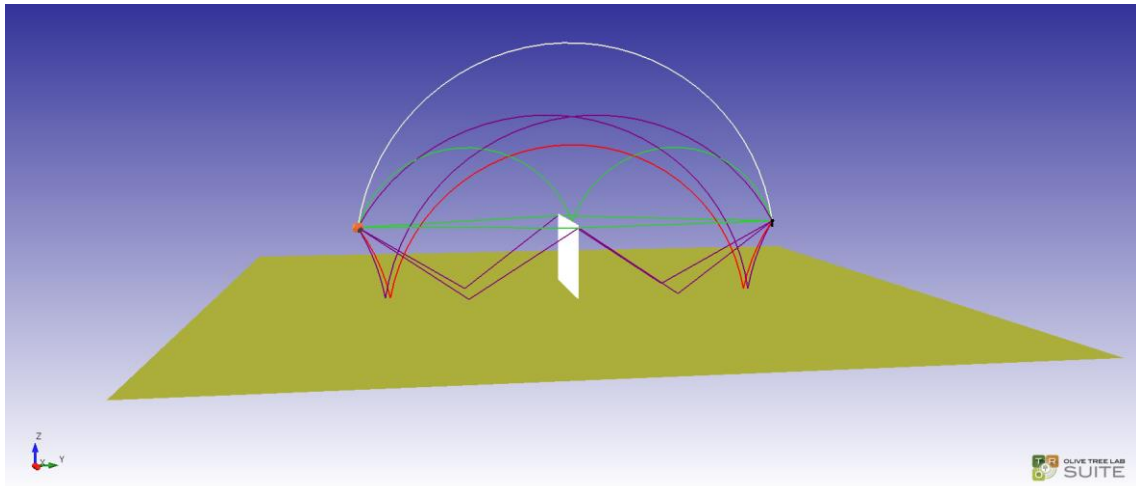
Figure 26. Refracted sound diffractions.

Our method has limitations like a) it is applied only on sound diffractions located on a plane vertical to the ground. We are not aware of any ray-based model that could consider sound diffraction by lateral diffraction paths b) sound reflections, which are caused by the refraction between diffraction points, are neglected. Only the bending of the sound path is calculated. But due to the attenuation caused by both the sound reflection and sound diffraction, we hypothesize that the impact of such sound paths on the sound field would be of marginal importance.

3.4 Results Validation

The accuracy of our calculations and the importance of our contribution in improving the accuracy of calculations have been investigated in the following projects:

a. We attempted to reproduce room resonances in a room and compare them with published measurements (Economou & Charalampous, 2016) .

b. We compared our model with the widely adopted calculation model proposed by ISO 9613-2 (Economou & Charalampous, 2012).

c. We used our model to investigate the effects of sound diffraction on the acoustics of ancient theaters (Economou & Charalampous, 2013).

d. We used our model to simulate and predict a well-known, wave-based effect noticed in modern theaters, the seat dip effect (Economou & Charalampous, 2016).

e. Our work was used to predict the sound field caused by wind turbines (Bigot, Economou, & Economou, 2017).

The above application projects are described in the following subsections.

3.4.1   Room Resonances using WBGA

To investigate the improvements achieved in calculating the effect of sound reflections by our calculation model when compared to traditional geometrical approaches, we calculated room resonances, a purely wave-based phenomenon, which has been calculated using only numerical methods up to now. We compared simulated results to actual measurements taken by Bolt (Bolt, 1939). Bolt, in his effort to measure sound distribution within a nonrectangular room, devised an apparatus that enabled him to vary the angles of the walls of a scaled room model made of brass plates, which are highly sound-reflective materials. The height of the model was small compared to the sound wavelength used and therefore no normal modes with vertical components could develop. Essentially, the model was a 2-dimensional model where axial and tangential modes of vibration were investigated. The source was-flush mounted on the hard "ceiling", and the microphone was located on the floor (we assume at zero height). Rather than moving the microphone around the model, he devised an apparatus that enabled a microphone to be fixed at a tabletop while the model moved about the microphone, with the tabletop acting as the room's hard "floor". At the same time, a drawing board in conjunction with a microphone positioning recording system was used to record the trajectory of the microphone, which according to the same paper, a 0.1" (2.54mm) change in space would have a sound level variation as much as 10 dB. The size of the original model, a trapezoid, had the dimensions given in the figure below, but it was smaller by a factor of 10 (Figure 27). The frequency range investigated in the experiments varied between 886Hz and 2302 Hz; the range the source could provide adequate and linear sound.
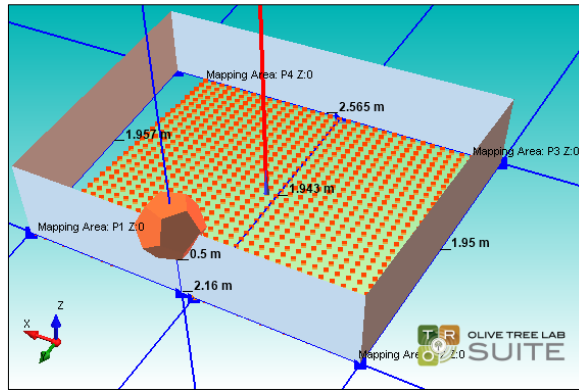
Figure 27. 3D model setup.

The 3D model setup is shown in Figure 27. Our model is larger by a factor of 10 than the original scale model, therefore, the results in the digital model are examined at frequencies divided by a factor of 10. Our calculation engine mapping feature is limited to the standard 1/3rd frequencies, therefore, since during the 1939 experiments, the frequencies used have been chosen arbitrarily and there is no exact correspondence between our mapping and Bolt's mapping. Also, digital mapping can only be made in rectangles; therefore, it was mostly confined to the center of the trapezoid. A 30x30 matrix of receivers was used in mapping for validation purposes.
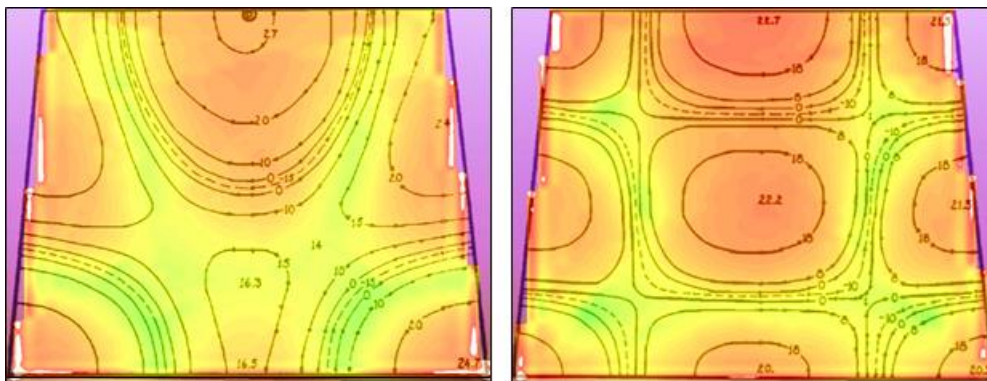
Figure 28. Comparison of our algorithm calculations (colored sound level plot) and Bolt's sound measurements (contour lines). In green the lowest sound pressure levels and in red the highest.

All walls were hard, which corresponds to a flow resistivity of 20MPas/m^2. In the calculations, 8 orders of reflections were used.

In Figure 28, we can see the comparison of our calculations with Bolt's sound measurements. The colors indicate the relative sound levels, and the contour lines

79

represent the measurements taken from Bolt. On the left, the sound measurement mapping is at 1721 Hz while the colored mapping is calculated at the 1/3rd octave band of 200 Hz. The sound measurement mapping on the right is at 2302 Hz while the colored mapping is in the 1/3rd octave band of 250 Hz. In red and green, high, and low sound levels are indicated, respectively. Based on Figure 28, we can observe a correspondence between measurements and calculations, especially if one takes into consideration the following:

- During the experiments only a single frequency was used while for the simulation, 4 frequencies within the 1/3rd octave band were used (mapping in 1/12th octave).
- The 1/3rd octave bands center frequencies values do not correspond to the frequency values reported by Bolt.
- As reported by Bolt in the same paper, microphone positioning was overly sensitive to sound level changes. This means that frequency deviations (wavelength) cause equally abrupt changes in level.

In Figure 29 a 3D mapping on the left is in the 1/3rd octave band of 200 Hz. The mapping on the right is in the 1/3rd octave band of 250 Hz. The figures correspond to the images of Figure 28 above and represent in 3D the mapping results while allowing the visualization of resonances in sound distribution within a 2D trapezoidal room and determining the nodes and anti-nodes, as well as their levels and spread.
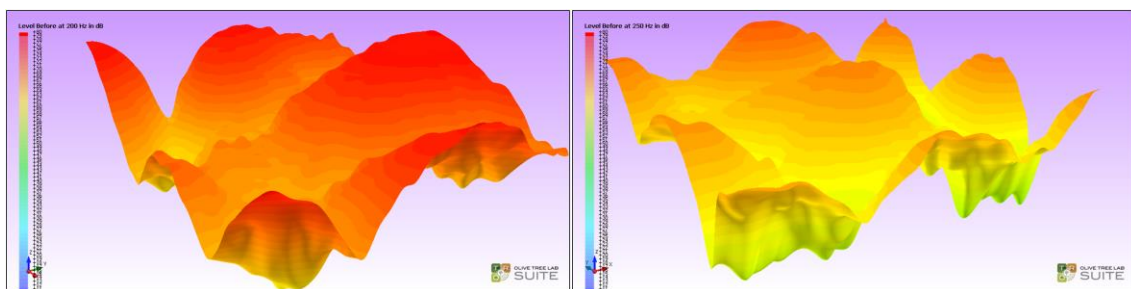
Figure 29. Left - 1/3rd octave band of 200 Hz. Right - the 1/3rd octave band of 250 Hz.

Morse and Bolt (Morse & Bolt, 1944) present another set of testable configurations and measurements based on a cross-sectional sound distribution (Figure 30. On the left, there are the planes (sections A,B,C), where sound mapping was carried out. These

correspond approximately to the sections Bolt is referring to in his experiment. On the right, mapping results in red superimposed on the data, according to Morse & Bolt (Figure 29) (Morse & Bolt, 1944)**.**
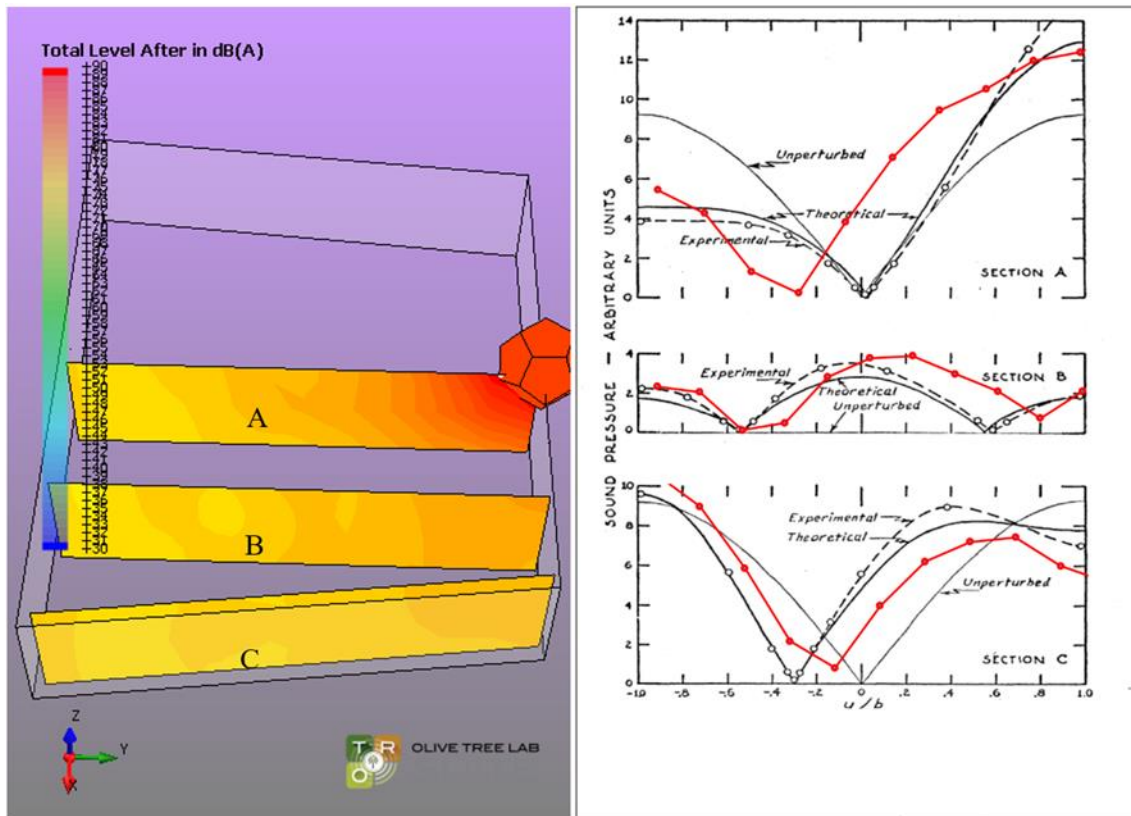
Figure 30. Comparison of calculations (left) and measurements for the Morse and Bolt model (right).

Even though the results show some deviations from the measurements. we can attribute these differences to measurement and modelling uncertainties, leading us to the conclusion that our calculation model could be used effectively for the calculation of room resonances.

3.4.2 WBGA vs ISO 9613-2

To see the improvements in the accuracy of our calculation model, we have compared our results with the method proposed by ISO in ISO 9613-2 (International Standards Organization, 1996) for calculating attenuation of sound during outdoor propagation. We implemented ISO 9613-2 and then compared the results of ISO 9613-2 with our

model by using cases based on sound measurements taken from a report presented by DELTA (Danish Electronics Light & Acoustics, 2006).

Distance S - R					
4.5 m	Case 13	Case 17	Case 33	Case 36	
50 m		Case 91			Case 92
100 m	Case 77				
120 m					Case 40

Table 3. Models chosen from the DELTA report.

Table 3 presents the cases we chose from the DELTA report to model and run the calculations on. Figure 31, Figure 32 and Figure 33 present the results of our simulations. For each case, the following information is presented from the top right moving counterclockwise:

a) The case setup showing the heights of source and receiver from the ground as well as the heights and widths of sound barriers in place
b) The calculated excess attenuation from both calculation models compared to sound measurements
c) 3D representations of the models inside the software tool
d) 3D sound mapping plots demonstrating the excess attenuation levels around the sound receivers.

The results of our model match well with the measurement results, even though we anticipated a better agreement. Deviations from the measurements are attributed to measurement and modelling uncertainties, like the exact value of the materials' flow resistivity and the exact location of the geometry objects. As mentioned above, there is limited information on the details of how the Nord 2000 validation data were obtained in order to fine tune the 3D models used for these calculations. Concluding, this experiment shows that a wave-based sound propagation model is more suitable for predicting sound propagation in outdoor environments than the energy-based method proposed by ISO 9613-2.
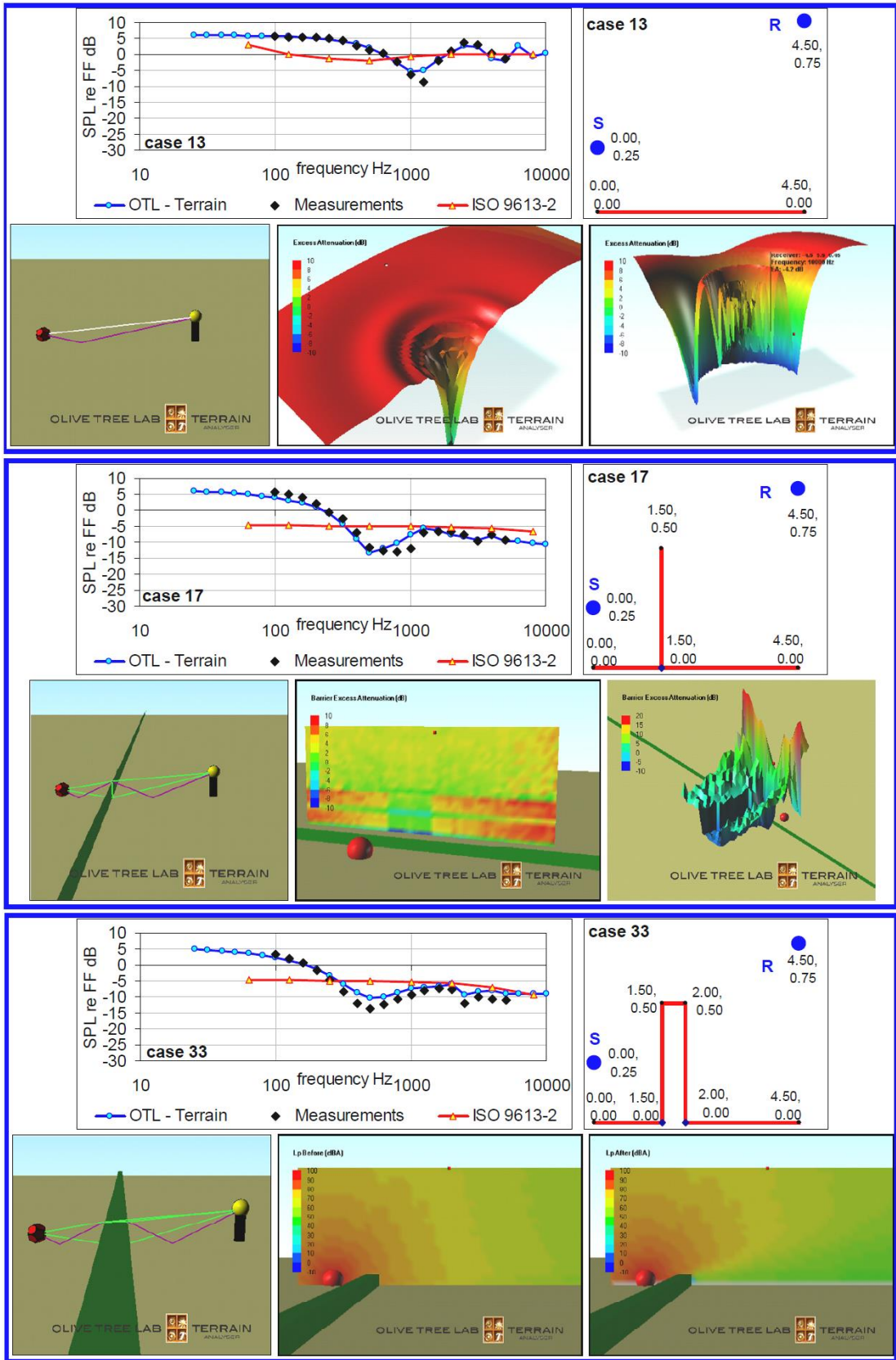
Figure 31. Results for a short distance non-barrier case (top), thin barrier case (middle) and a thick barrier case (bottom)
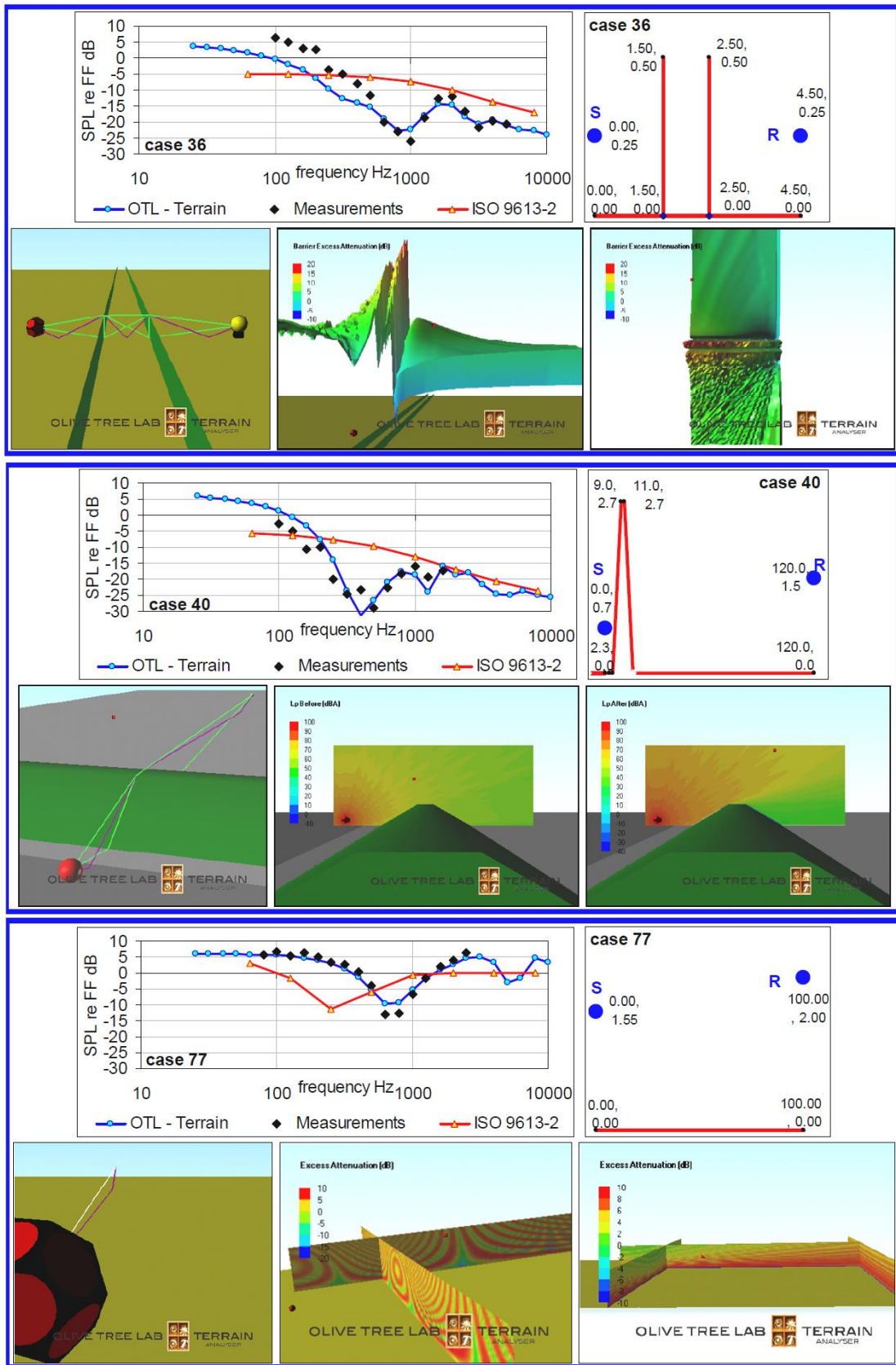
Figure 32 . Results for a double thin barrier case (top), a thick wedge case (middle) and a long distance no-barrier case (bottom)
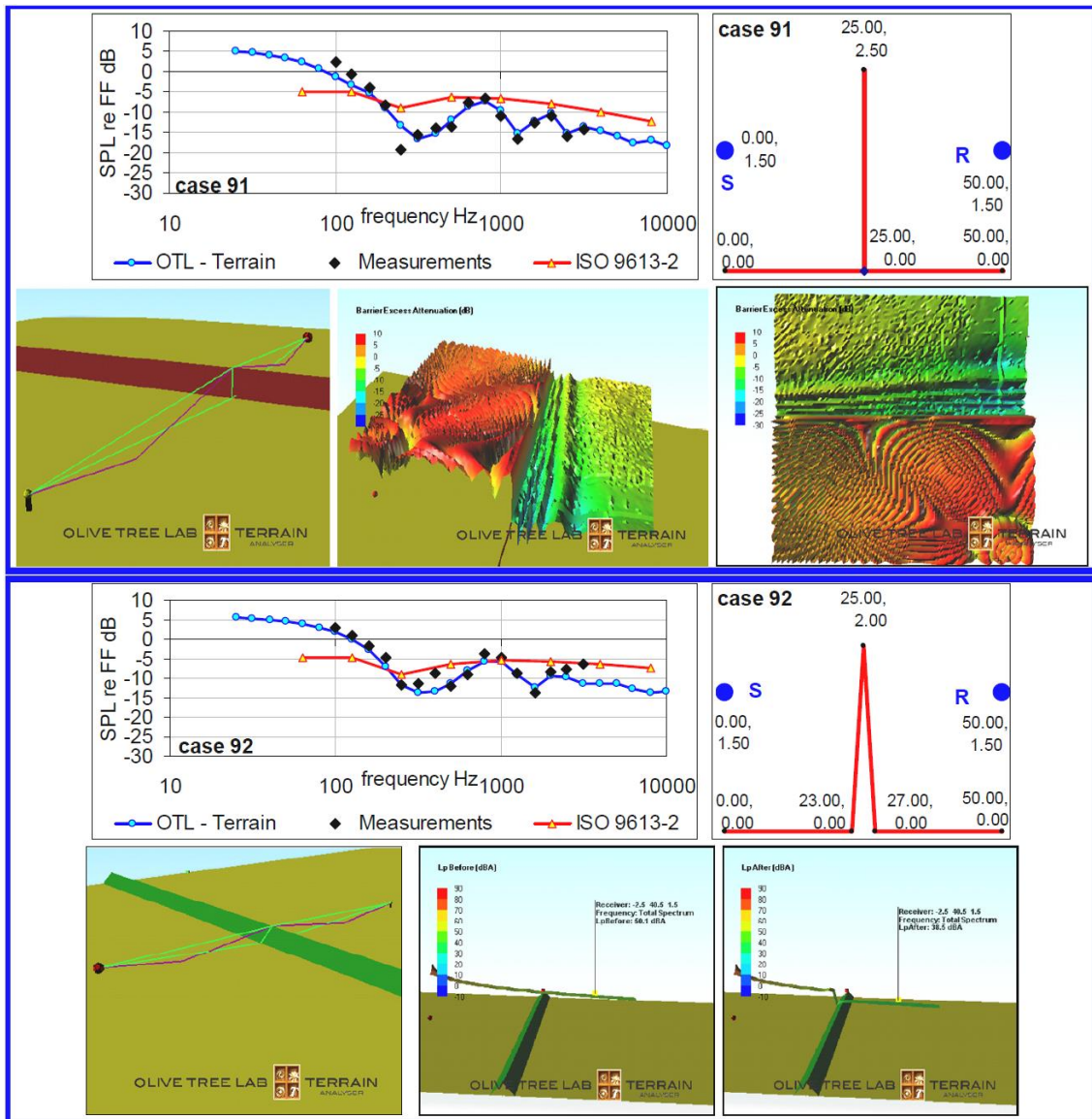
Figure 33. Results for a single barrier case (top) and a thin wedge case (bottom)

3.4.3 The Effect of Sound Diffraction on Ancient Theaters Acoustics

The acoustics of ancient theatres is a widely studied field of acoustics. At the same time, the geometrical properties of ancient Greek and Roman theatres are ideal for evaluating an advanced sound diffraction calculation model because of the numerous edge-forming steps found in such theatres, which directly affect the sound field of the listener at any position inside the theatre. To evaluate the accuracy of our diffraction calculations, we calculated the sound field and the acoustical properties of ancient theaters. One of the contributions of our work, compared to previous work on geometrical sound diffraction, is that we take into account diffraction paths not only in occluded areas but in non-

occluded as well. The space above an ancient theatre's seats receives a large amount of diffracted sound from the theatre's cavea. Since this has not been taken into consideration for ancient theater acoustics in past studies, we decided to investigate the contribution of sound diffraction on the sound field of ancient theatres.

The project involved two major phases a) reproducing sound measurements taken in ancient theatres b) isolating the diffracted component from the sound field and assessing its contribution. For the project, we have chosen the Kourion theatre in Limassol, Cyprus, for which we made sound measurements and produced a 3D model based on its cavea imprint. The exact process followed is described in detail in the following sections.

3.4.3.1 Modeling of Kourion Theatre Geometry

The modeling of a space for simulation purposes determines the accuracy of the simulation results. The imprint of Kourion theatre geometry (or any other ancient structure, for that matter) has limitations since surfaces are modelled as smooth and level while, due to time erosion, they are uneven and rough, as Figure 34 shows.
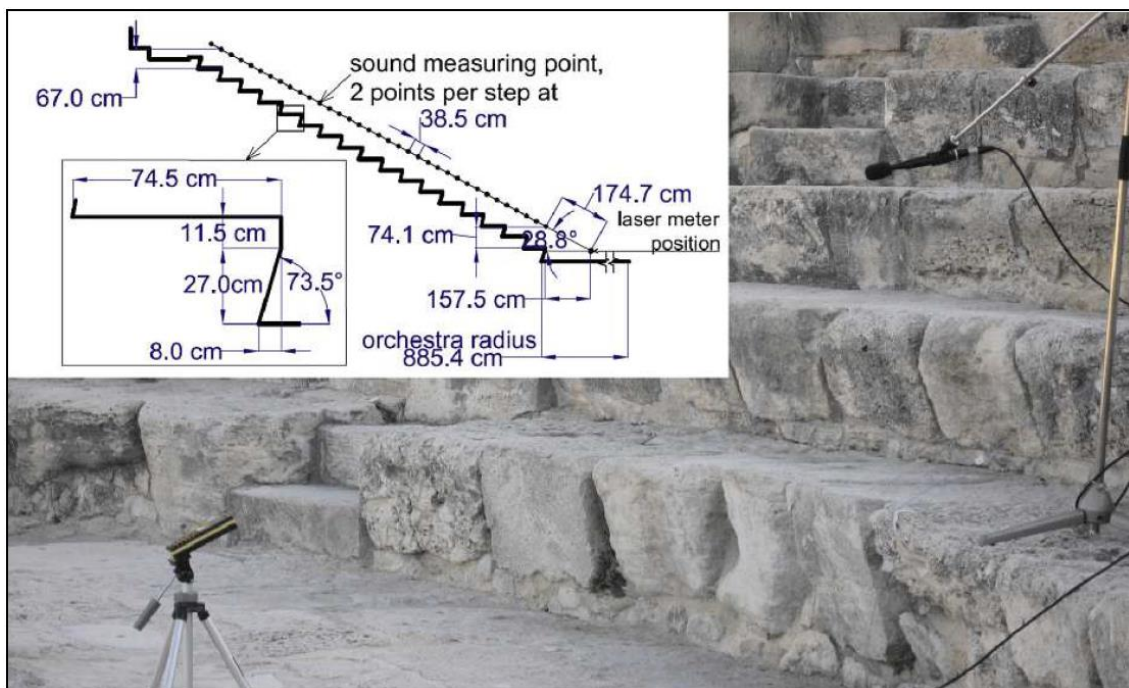
Figure 34. Cavea section modeling.
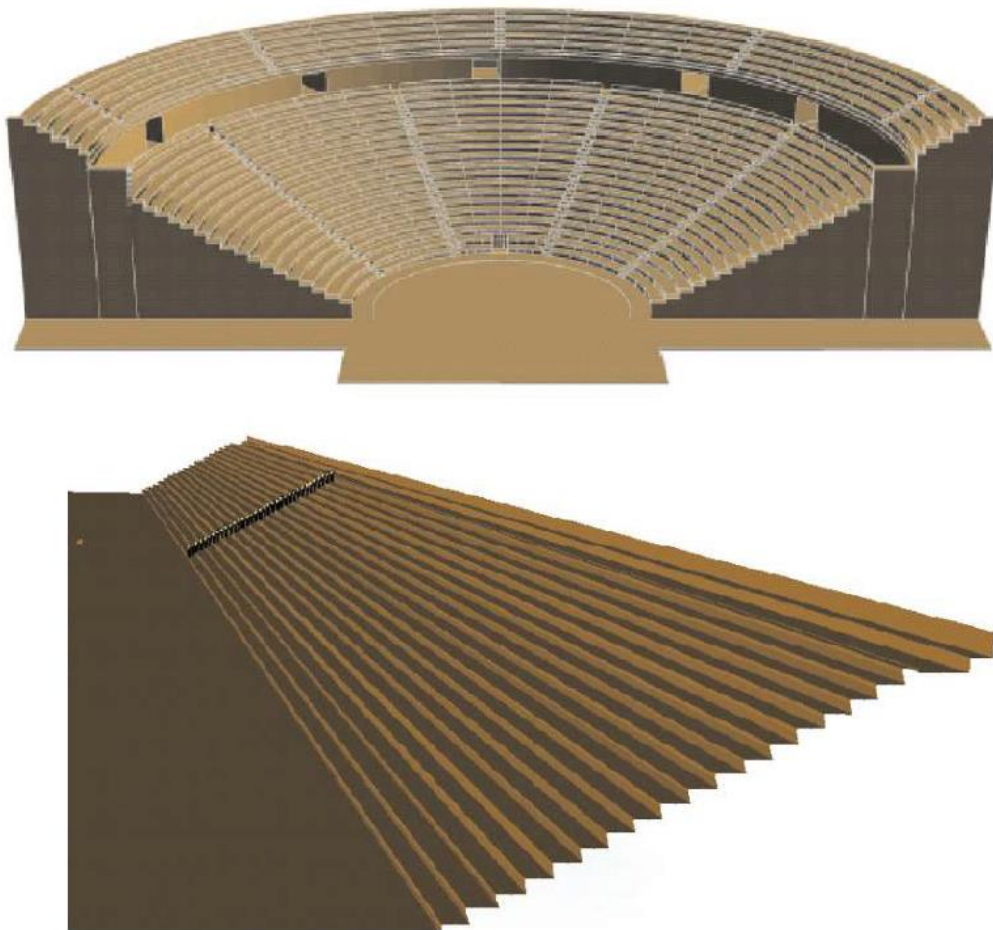
Figure 35. Straight lines case(bottom) which is equivalent to a semicircular theatre(top). The two cases are equivalent only if the sound source is placed at the exact center of the theatre's scene. This equivalency is not applicable for any other location of the sound source.

The imprint and modeling of the sections of the cavea was made as follows. Firstly, the exact center of the orchestra was defined and then its radius was measured. Using a laser distance meter (at Kourion and a tape measure at the Heritage), the section of the theatre over which sound measurements would be taken was created by measuring the dimensions of each audience step. Once the section was constructed and based on the Ray Equivalency Theorem (see Appendix), a three-dimensional model was created by the extrusion of the section (see Figure 35). In brief, the Ray Equivalency Theorem states that if the sound source is placed at the exact center of the theatre's scene then the semicircular model of the theatre can be substituted with an equivalent model consisting of straight lines of seats created by the extrusion of the theater's section. This

equivalency is not applicable for any other location of the sound source. Figure 35 demonstrates the two equivalent cases, a semicircular theatre and the equivalent model consisting of straight lines of seats.

3.4.3.2 Sound Measurements
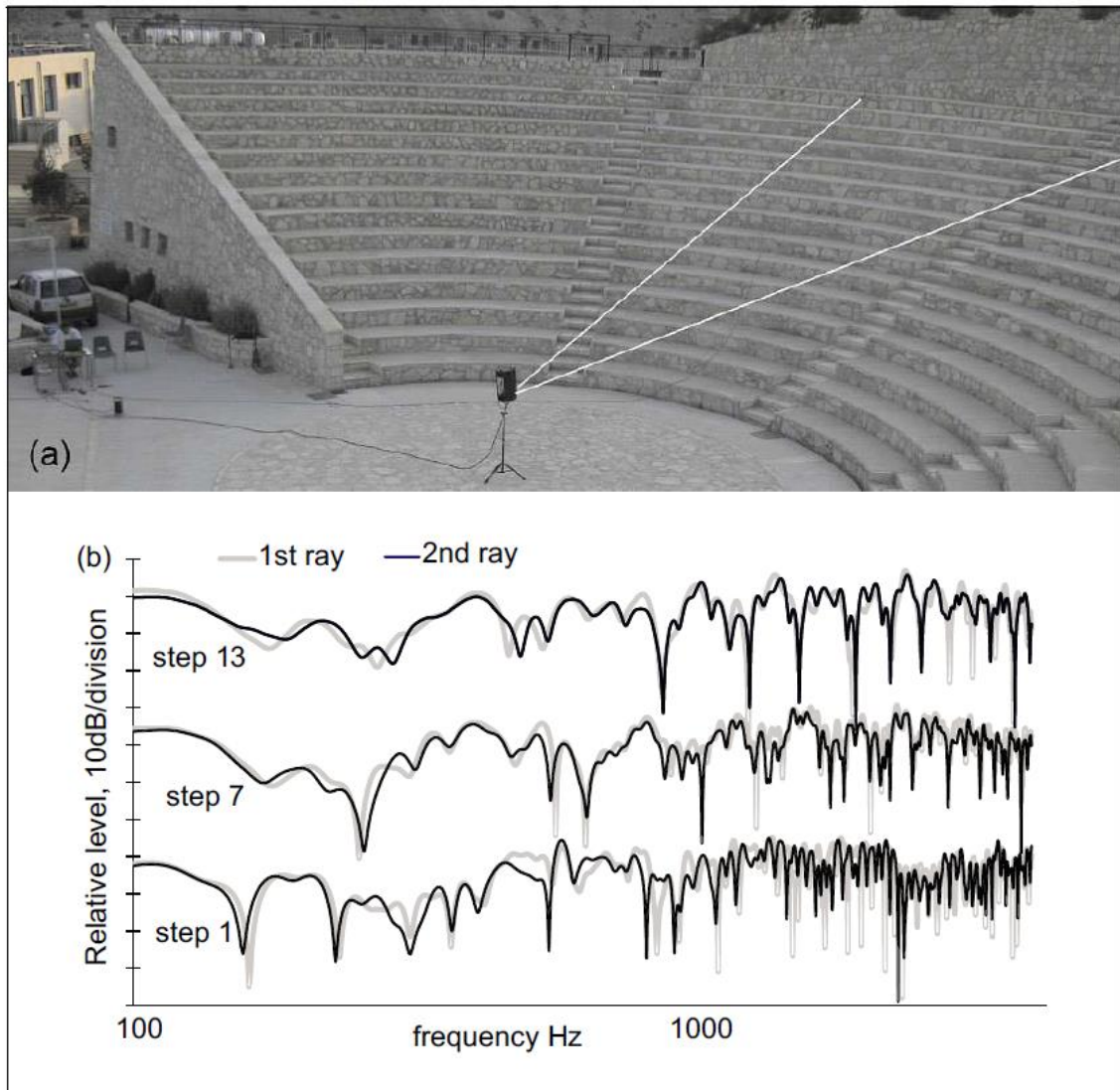
Figure 36. Sound measurements comparison between 1st and 2nd ray.

The next step was to establish at the Heritage Private School Theatre a protocol of measurements to be followed at Kourion, to determine whether the source would be suitable for the measurements at Kourion and to provide evidence that the Ray Equivalency Theorem applies. Sound measurements were taken at three-step heights (1st, 7th and 13th out of total of 13) at two cavea positions, i.e., on two different rays over the cavea from the center of the orchestra, as shown in Figure 36. The source used

was a two-way 10" active constant directivity speaker unit (70 Hz to 18 kHz of unknown crossover frequency). With the use of a commercially available acoustic measurement software application, WinMLS, the driver was fed with a sine sweep sound within the frequency range of 50 Hz to 20 kHz. Sound measurement results on two cavea rays, shown in Figure 36, give indications of the applicability of the Ray Equivalency Theorem since the sound measurement results match very well for the two rays.

As a monument, Kourion receives a lot of visitors throughout the day and one needs a permit from the Department of Antiquities in order to carry out any work there. Faced with these facts and in order to secure minimum atmospheric effects, which were monitored with a portable weather station, measurements took place between 6.30 am and 9.00 am. The microphone position for each sound measurement was established using a laser distance meter. A laser meter was placed in the orchestra, sending a beam at a height of 75 cm above each step, corresponding to the height of a seated person, as shown in Figure 34. The laser beam was used to position the microphone at intervals of 38.5 cm, corresponding to approximately two measuring points on each step at heights which varied (step dimensions are irregular) between 70 and 103 cm above the steps. Each microphone position height was then measured from the level of the corresponding step.

3.4.3.3 Calculation Results

The results of the Kourion measurements are shown below in terms of EA versus frequency and EA versus distance. EA was used in the presentation of results since sound pressure levels are biased by sound source and microphone response. In all simulations, second-order reflections were used, the maximum order detected by our model for all 35 receivers. CATT and EASE, two commercially available software packages, were used with the semicircular geometry of Kourion as a model to verify that only 2nd order reflections are possible in the theatre. Up to second-order sound diffractions were used, since the effect of higher orders of sound diffractions may be neglected without degrading accuracy (Kim, Kim, Kang, Kim, & Kim, 2005). All surfaces were treated as hard and were given a flow resistivity value of 20,000 kPa s/m2. The analysis was carried out in 1 Hz resolution between 50 and 10000 Hz.
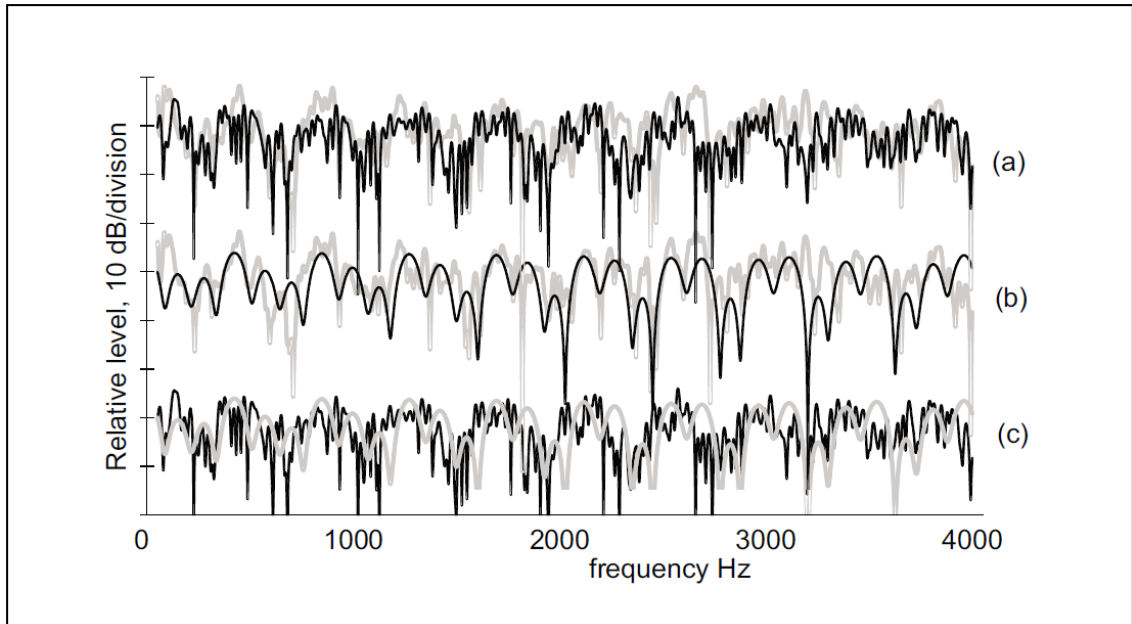
Figure 37. EA results extracted from Kourion measurements, compared to simulation results, with and without diffraction, in relative levels (ref FF). (a): Measured (grey) vs. simulated with diffraction (black), (b): Measured (grey) vs. simulated without diffraction (black), (c): Simulated with (grey) and without (black) diffraction.
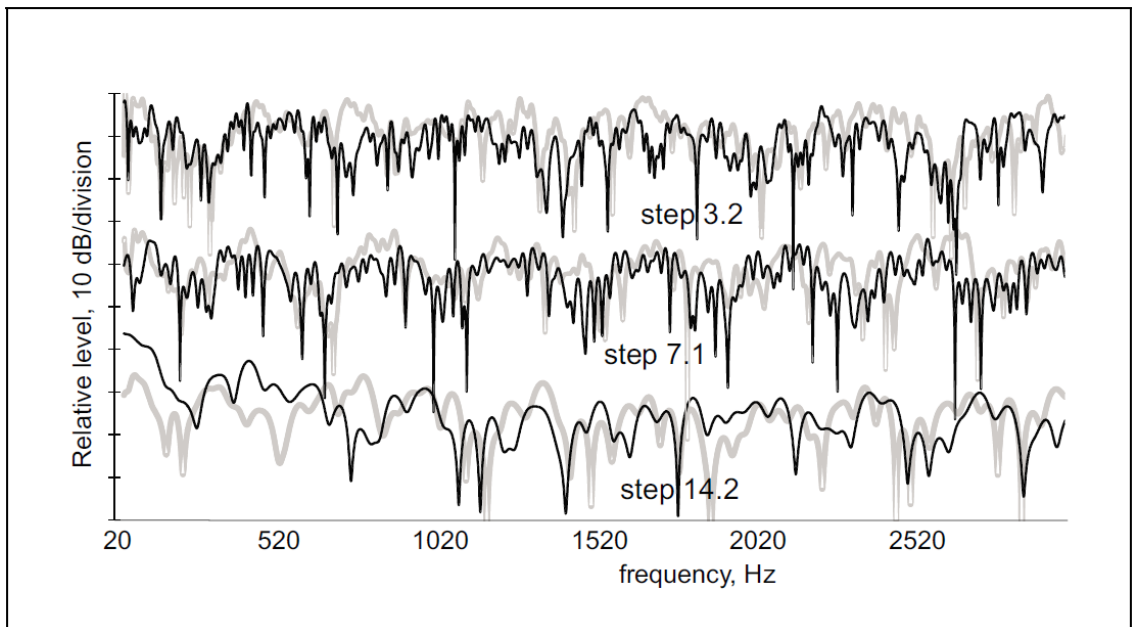
Figure 38. Sound measurements (in grey) and simulation results including second-order diffraction at three Kourion steps, 3rd, 7th, 14th, out of a total of 17.
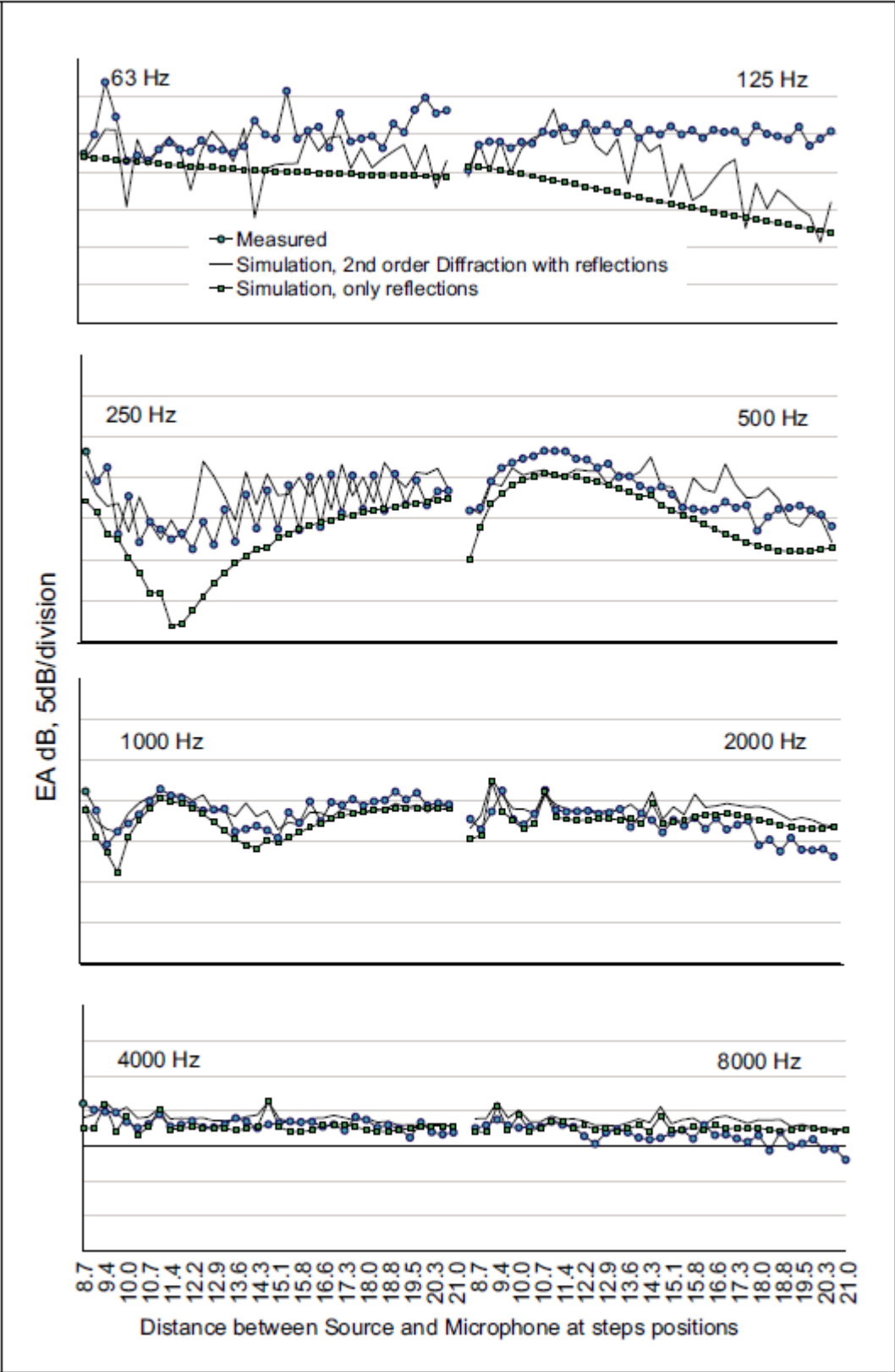
Figure 39. EA against distance (at intervals of 38.5 cm) in selected 1/3rd octave bands. Sound measurements versus simulation results with and without diffractions.

Figure 37 shows in graphical form the Excess Attenuation results extracted from the Kourion measurements, as well as the simulation results, with and without diffraction. They help demonstrate the effects of including diffraction in sound simulations. The results refer to the 7th step microphone position from the center of the orchestra (S - R distance, 13.234 m). The frequency axis is linear to show differences more clearly.

Figure 38 shows the results in terms of EA from sound measurements and simulations including second-order diffractions at three steps, the 3rd (close to the orchestra), the 7th and the 14th step out of a total of 17 steps at Kourion. Source - receiver distances are 10.043 m, 13.234 m and 18.405 m respectively. For presentation purposes, the curves are shifted in level. The frequency axis is linear to show differences more clearly.

To visualize how sound is filtered as it propagates over the cavea, EA is plotted against distance (at intervals of 38.5 cm) in 1/3rd octave bands. Figure 39 shows the EA extracted from measurements and simulation results with and without diffractions. Again, for presentation purposes, the curves are shifted in level (ref FF, for the selected 1/3 octave band results shown), while the X-axis represents the receivers' distances from the source as they are located on a section of the cavea.
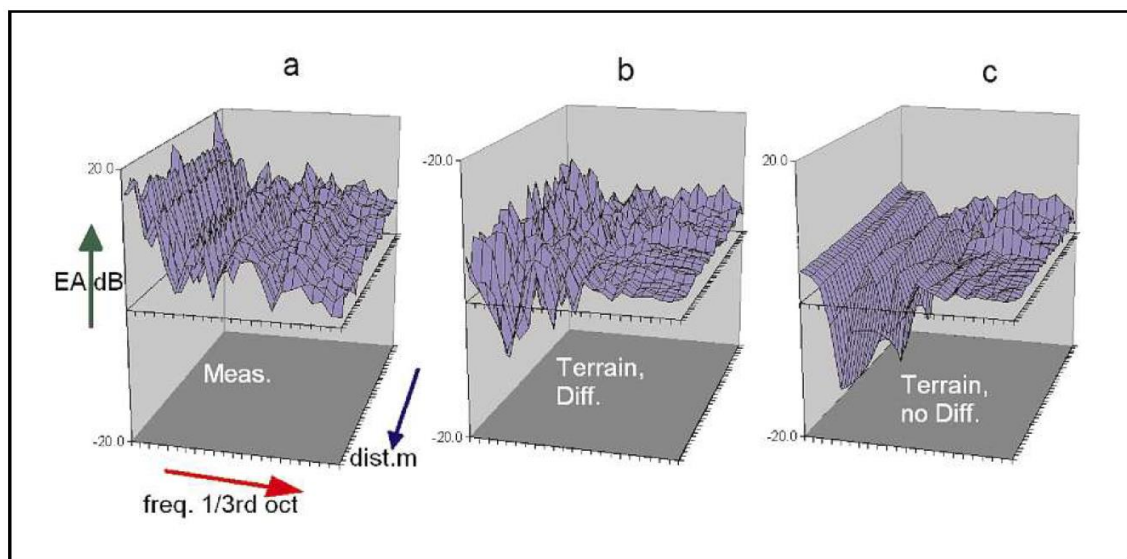
Figure 40. Excess Attenuation results versus distance and frequency (in 1/3rd oct. bands): (a) - measured, (b) - simulated with diffractions, (c) - simulated without diffractions.

Figure 40 shows the above Excess Attenuation results versus distance and frequency: Left measured, middle simulated with diffractions, right simulated without diffractions. Arrows show an increase in frequency and distance values.

In addition, Figure 41 shows the broadband relative sound pressure level, versus distance, plotted on a logarithmic axis. Also shown in dashed lines are the theoretical distance attenuation trends of arbitrary values for comparison purposes, −6 dB per doubling of distance.
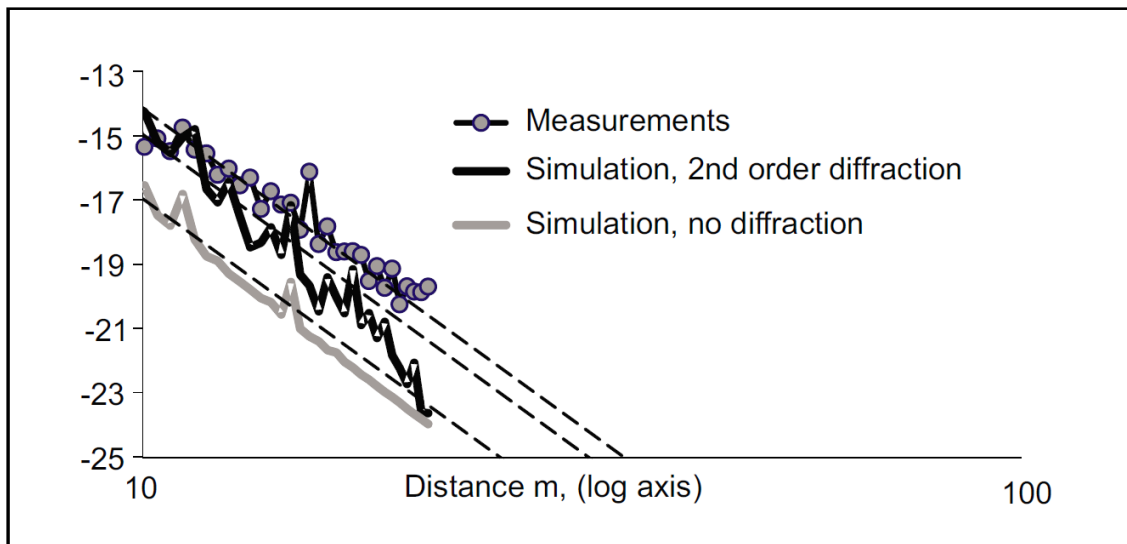
Figure 41. Total broadband sound pressure level versus distance (log axis).

3.4.3.4   Discussion and Conclusions

This project demonstrates that diffraction calculations are vital in acoustically simulating ancient theatres or open-air spaces. Diffraction effects provide the finer structure of the acoustical response of the theatre. Open-air theatre acoustical simulation results without diffractions give a crude frequency response without details and ignore interference effects due to the sound diffractions that take place in real life. A close examination of the results shows that the measurements response is irregular and has details, while the simulated reflections response (without diffraction) is smooth and rounded. The same trend applies to simulated results with and without diffraction. Sound diffraction shapes the detail over the rounded reflections response, and it is responsible for the "embroidery" detail. Furthermore, calculations without diffractions underestimate overall sound level contributions from theatre structures. Simulations of open spaces without sound diffractions assume that energy is concentrated on rays

which after some reflections are eventually lost to the environment. On the contrary, simulations with diffractions or scattering include additional sound paths that offer part of their energy to the theatre before vanishing to the environment.
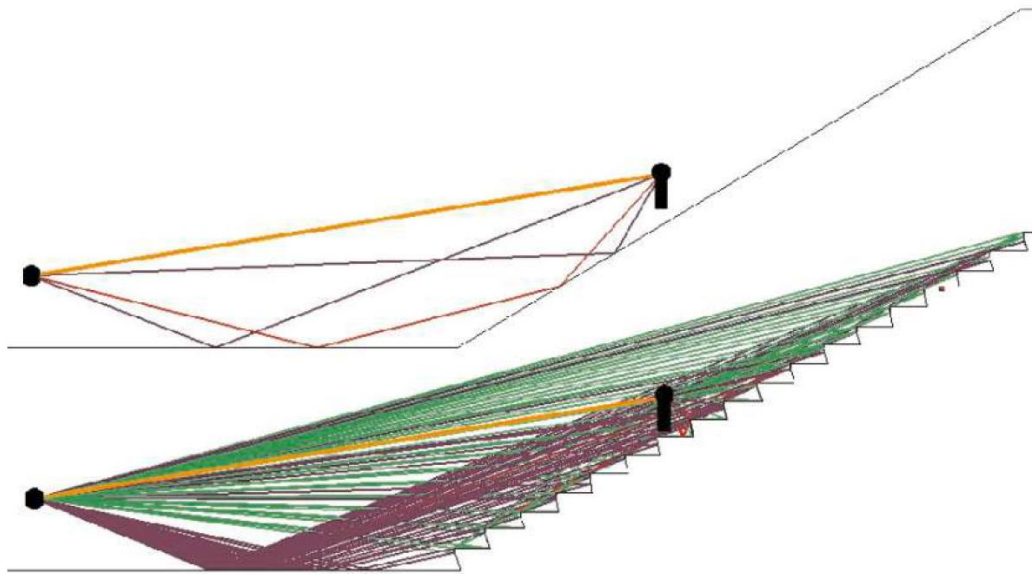
Figure 42. Comparison of sound propagation over two types of caveae, smooth (top) versus stepped seating (bottom).

Figure 42 shows a comparison of sound propagation over two types of caveae, smooth versus stepped seating. The figure shows direct sound with three reflections off the orchestra and the smooth cavea (diffraction was ignored) and direct sound, reflections and diffractions off the orchestra and the stepped cavea.

In effect, sound diffraction provides a more diffused field and most probably yields reverberation times that one would not anticipate in open spaces. Studies of the "periodically-rough ground effect" (Bashir, Attenborough, Taherzadeh, & Hill, 2010) and the "seat-dip effect" observed in enclosed auditoria (Bradley, 1991) (Davies & Cox, 2000) (Takahashi, 1997) bear resemblances to the study of open ancient theatres with stepped seating. All cases have in common multiple edge diffraction. In the "diffraction-assisted rough ground effect" and the "seat-dip effect" studies is observed that the periodical placement of obstacles over a ground or floor shifts the EA maxima to lower frequencies. EA maxima, shown as dips in the frequency response, are attributed to the

destructive interference of direct sound with diffracted-reflected-diffracted sound from the ground or floor. To examine such a phenomenon in open ancient theatres, the cavea was simulated as smooth and the results were compared to simulations with stepped seating. Figure 42 shows sound paths from a smooth and a stepped seating cavea. In the case of the smooth cavea, there are four paths: the direct sound, two first-order reflections and one second-order reflection. Diffraction was ignored. In the stepped seating case, direct sound and multiple reflections and diffractions up to second order are shown. In both cases flow resistivity is assumed to be 20,000 kPa s/m2.
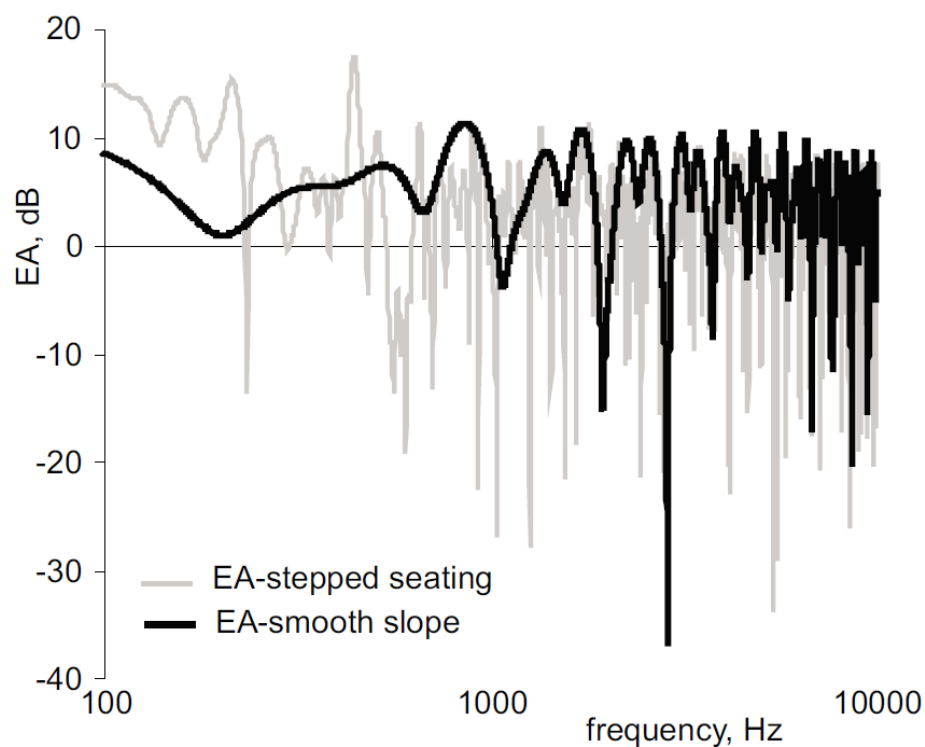
Figure 43. Comparison of EA over two types of caveae, smooth versus stepped seating.

The EA spectra of both cases are shown in Figure 43, where there are indications of a shift of EA maxima to lower frequencies. The difficulty in verifying such indications arises from the fact that there are three ground reflections present, whereas in a diffraction-assisted rough ground effect, for example, there is only one ground reflection involved. However, this was not investigated further, since it is beyond the scope of this work.
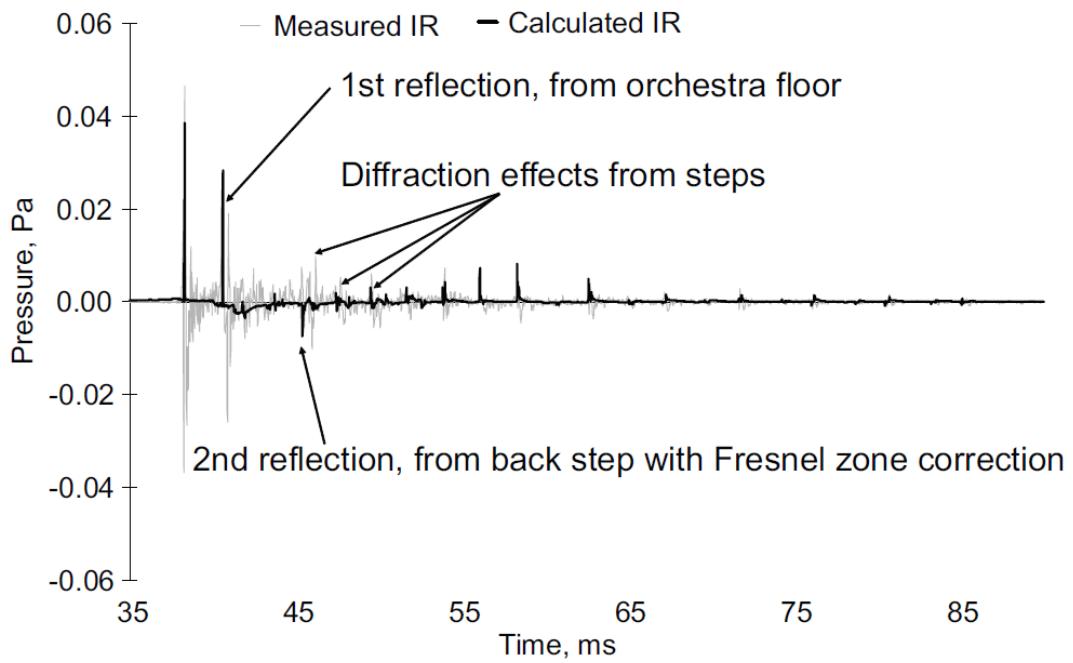
Figure 44. Measured versus calculated IR at step position 7.1 with Fresnel zone reflection correction.
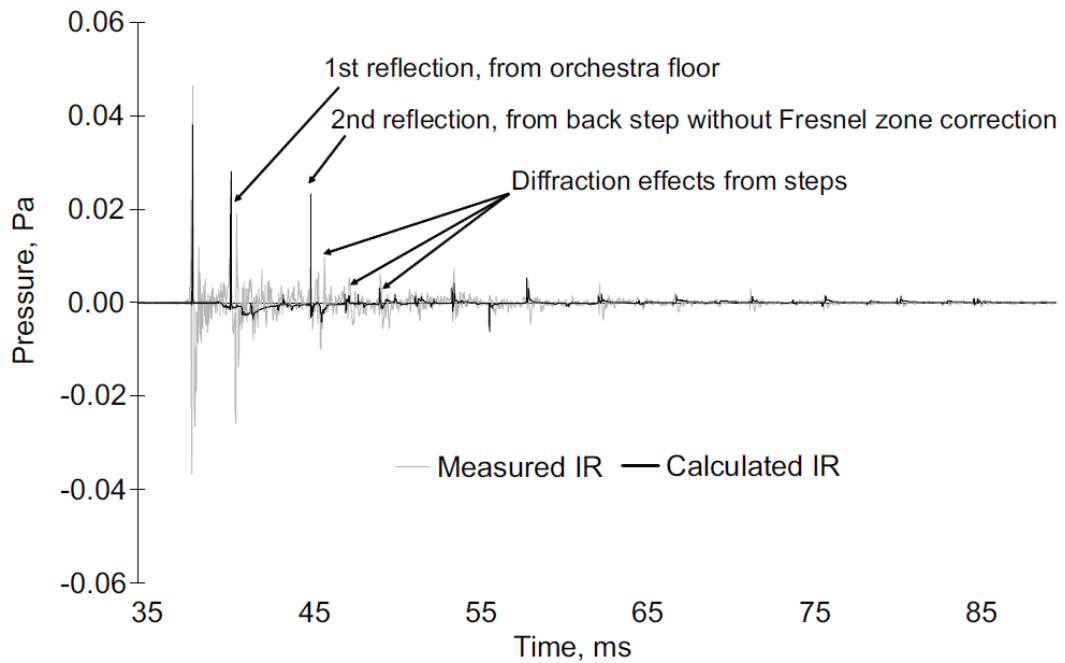
Figure 45. Measured versus calculated IR at step position 7.1 without Fresnel zone reflection correction. It is evident that the Fresnel zone correction simulates results more accurately.

Even though there is a fair match between the measured and simulation results, there are also discrepancies between them, which are more evident in the low-frequency range. These differences may be attributed to many factors, as discussed above, but also to the limitations of the methods implemented by our model. A further example demonstrating deviations in simulating the actual space, source, receivers and its geometrical modeling is found in the time domain results shown in Figure 44 and Figure 45. Even though the time of arrival of direct sound and diffractions match fairly well between measurements and simulations, the orchestra floor reflection is shown to be earlier than the measured reflection. This indicates that the acoustic center of the speaker unit must not be the one assumed based on the unit dimensions, but one that is found a bit higher. Based on this example, it is also possible that the distance correction applied to EA might include an error, which could have shifted the simulated results upwards and away from the measured results (see all comparison results). Based on the findings of this work and for the specific geometry of open theatres, it seems that sound predictions and simulations could come close to real life sound fields, provided that they include sound diffraction effects. Simulations with sound diffraction in high-frequency resolution analysis provide the finer structure of sound fields; provide the missing details from calculations without diffraction effects; unveil the structure of diffused sound fields; and provide the inevitable increase in sound level as a result of more sound contribution by diffracted sound paths.

It is known that for engineering purposes 1/3rd or 1/1 octave band analysis might be adequate. However, for in-depth acoustical studies, high-resolution analysis is essential. The study of open spaces, such as ancient theatres by the method of simulation, is much more demanding than closed spaces since acoustical effects are more evident due to the non-returning waves escaping into the environment, i.e., they do not linger on to cover up details of sound fields frequency and time response. This work is limited in examining the acoustical properties of ancient theatres without an audience. The acoustical properties of ancient theatres with an audience, including diffraction effects, could be the subject of future work. The degree of diffraction effects in a theatre with an audience, that alters its sound field, remains to be seen. Any additional work should also be carried out in the time domain since certain psychoacoustical phenomena and criteria

might be refined or redefined based on parametric studies using simulations with sound diffraction.

3.4.4 The Seat Dip Effect

A well-studied effect in acoustics is the attenuation of low-frequency sound at grazing incidence over surfaces characterized by roughness, either of periodic or non-periodic structure (Tolstoy, 1982) (Biot, 1968) (Twersky, 1957) (Attenborough, Li, & Horoshenkov, 2007). This effect, known as the seat-dip effect, is also observed in theatres and halls. In effect, the total sound pressure is made up of the direct sound wave, scattered and reflected waves off seat rows and floor. According to Attenborough, (Attenborough, Li, & Horoshenkov, 2007) periodical space roughness, provides multiple attenuation maxima while randomly spaced roughness provides one broadband attenuation maximum. This happens because periodically placed objects over a surface, like in the case of theatre seating over a floor, which is coherently scattering sound, thus providing dip-interference effects in the frequency domain.

Theatre seating is made of periodically spaced objects. The seat dip effect was first observed at the beginning of the 1960s (Schultz & Watters, 1964) (Sessler & West, 1964). An overview of the theatre seat dip effect is given by Bradley (Bradley, 1991) while an updated reference list is given by Tahvanainen et al. (Tahvanainen, Pätynen,, & Lokki, 2015). Seat dip attenuation varies between 80 and 300 Hz depending on seat height and row spacing (Tahvanainen, Pätynen,, & Lokki, 2015). This phenomenon is more pronounced within the first 20ms of the impulse response and in seating areas where sound arrives free from reflections.

The study of seat dip phenomenon using models is mainly done using numerical methods (Lokki, Southern, & Savioja, 2011) or analytical models (Takahashi, 1997) (Ando, Takaishi, & Tada, 1982). As far as we are concerned, wave-based geometrical acoustics have never been used in the analysis of this phenomenon.

3.4.4.1 Analyzing the Seat Dip Effect (SDE) and its components

Ishida (Ishida, 1995) presented a very insightful study of the SDE. He used two barriers between source and receiver to analyze the sound paths which make up the SDE. In general, when a barrier shields the sound path between source and receiver, the

diffracted path has no phase change, while in the opposite case when there is a direct sound between a source, a receiver and a barrier, the diffracted path has a phase reversal and becomes negative. Figure 46 shows on the left, a barrier blocking a direct sound while on the right there is a direct sound between source and receiver over a barrier. The inset graphs on the left of each picture show the frequency response, while the graphs on the right of each picture show the time response with the impulses and directions for the two cases.
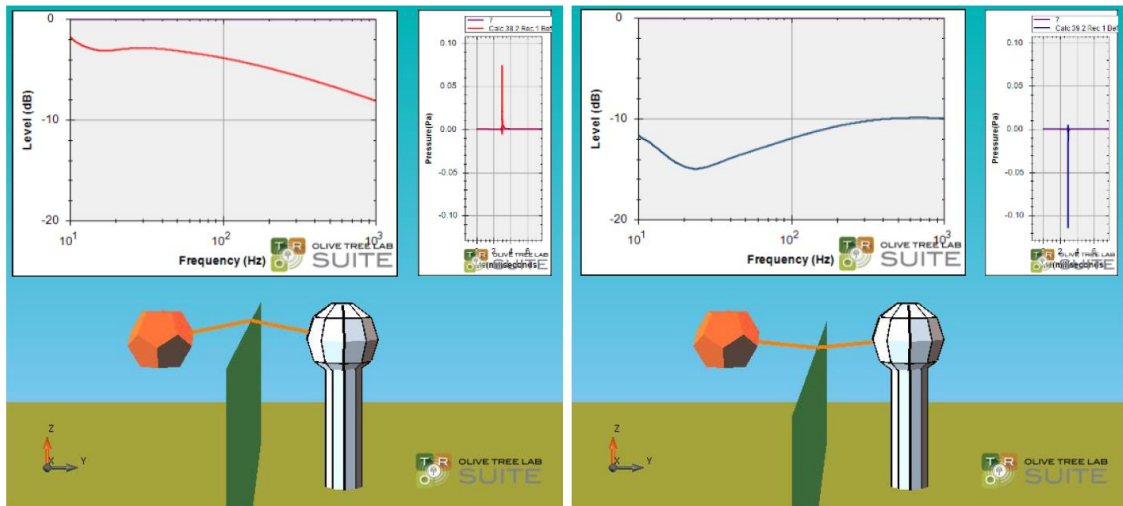
Figure 46. Left - A barrier blocking direct sound, Right – Direct sound between source and receiver over a barrier
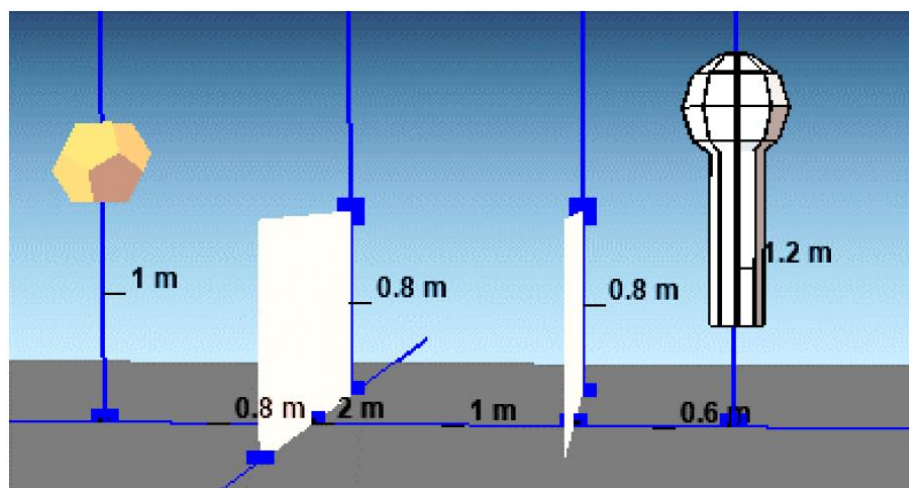
Figure 47. Ishida's experimental setup

Figure 47 shows Ishida's experimental setup. The model was 1/4th of full scale with seat (barrier) spacing of 1.0m and seat height of 0.8m. Figure 48 shows the individual

contribution of the first seven sound paths including combinations of diffracted -
reflected paths off the floor. The direct sound path is not shown.
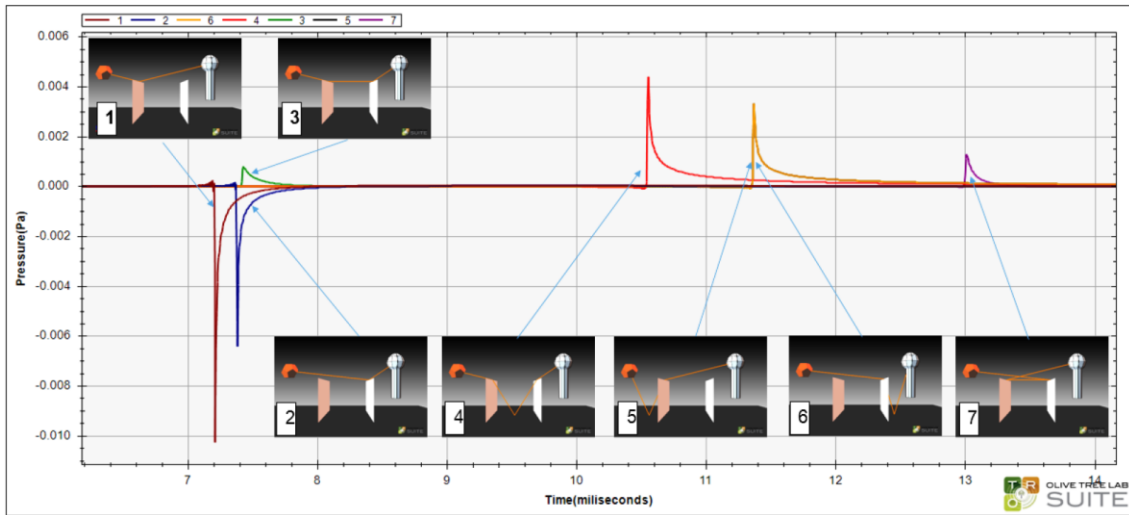
Figure 48. The individual contribution of the first seven sound paths including combinations of
diffracted - reflected paths off the floor in the time domain.

Figure 49 shows the same but in the frequency domain. The calculations include in each
case the contribution of the direct sound.
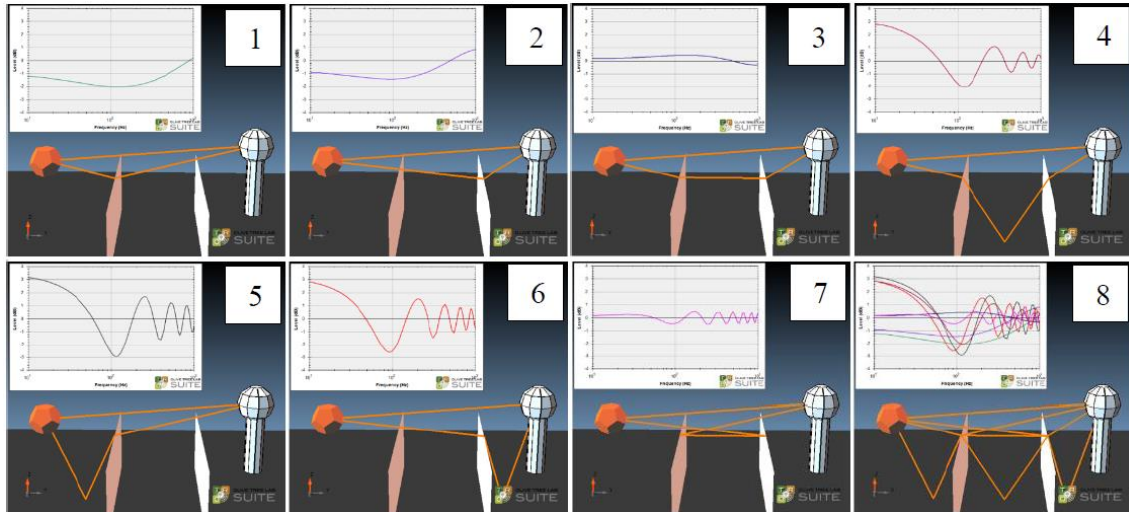
Figure 49. The individual contribution of the first seven sound paths including combinations of
diffracted - reflected paths off the floor in the frequency domain.

Figure 50 below on the left, shows that for a calculation with three orders of diffraction
and 3 reflections in between diffractions, the calculated number of paths is 156. The
inset figure shows the combined effect of all 156 paths with a dip around 95 Hz. The

figure in the middle shows the first eight sound paths between source and receiver with the dip located around 100 Hz. The figure on the right shows the barriers with the effect of a 20cm underpass and the dip calculated around 145 Hz. Ishida's measurements without underpass show a dip around 135 Hz, compared to our calculations at 110 Hz, middle picture of Figure 50. Ishida's measurements with an underpass, showed the dip to be close to 200 Hz, compared to our calculations at 135 Hz, right picture of Figure 50.
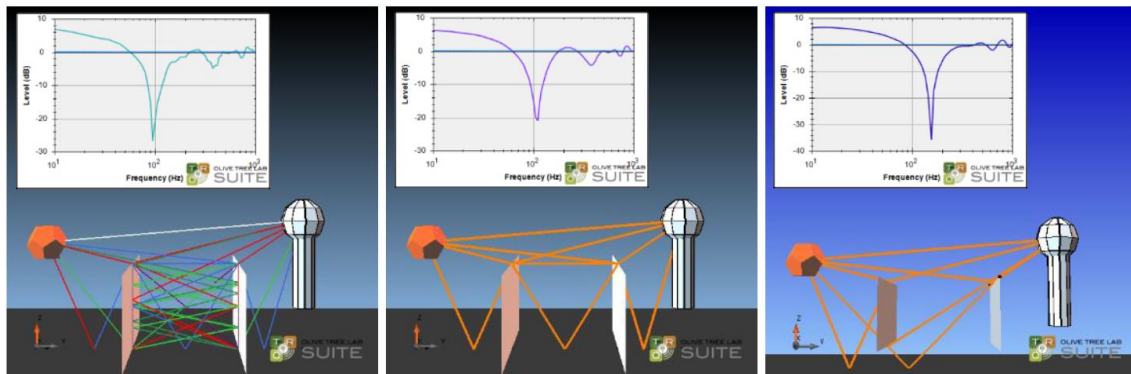
Figure 50. Left - Calculation results with 3rd order diffraction and three reflections in between diffractions, producing 156 paths. Middle - First eight sound paths between the source and receiver. Right - Barriers with the effect of a 20cm underpass. Inset figures - The combined effect of these paths.

Finally, based on the same setup, the effect of making the floor sound absorptive was also examined. For the hard floor calculations, all surfaces had a flow resistivity of 20 MPas/m2 corresponding to a sound absorption coefficient, αstat=0.010 at 100Hz, according to the Delany and Bazley method (Delany & Bazley, 1970). For the sound-absorbing floor calculations, the floor surface had a flow resistivity of 200kPas/m2 (αstat=0.087 at 100 Hz). It could be observed that the dip with a sound-absorbing floor is not as deep as the one calculated with a sound-reflecting floor. This configuration was not investigated by Ishida in his paper to provide a comparison. Figure 51 demonstrated the configuration and results.

For validation purposes, we present in Figure 52 the results from the 1982 paper by Ando (Ando, Takaishi, & Tada, 1982). On the left, the 3D full-scale model is used, which corresponds to the experimental 1/10 scale model by Sessler and West (Sessler & West, 1964), some of the first researchers to conduct experiments on the SDE when it
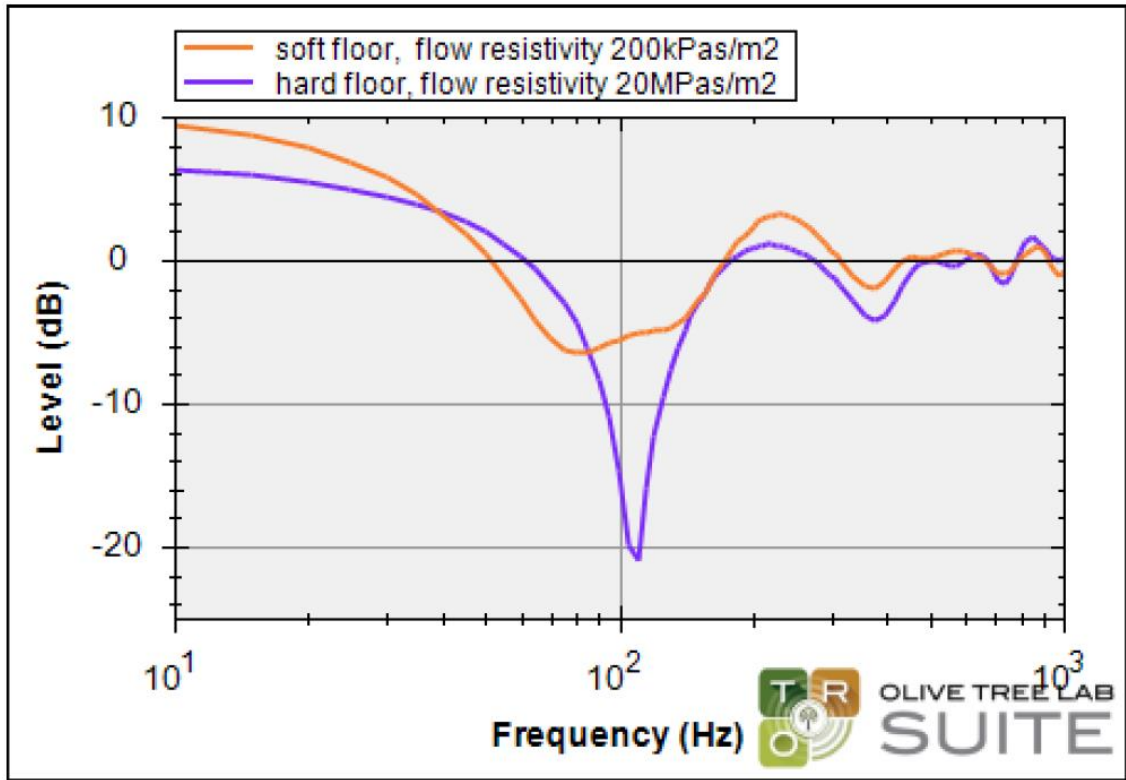
Figure 51. Calculations with hard floor and soft floor.

FIG. 2. Comparison between the sound pressures measured and those calculated, in reference to that of the direct sound. OOO: Tone-burst measurements with the 1/10 scale model (after Sessler and West[3]). .....: Continuous-wave measurements with the 1/10 scale model (after Sessler and West[3]). ——: Calculations with the boundary condition of the measurements, ($d_1 = 76$ cm).
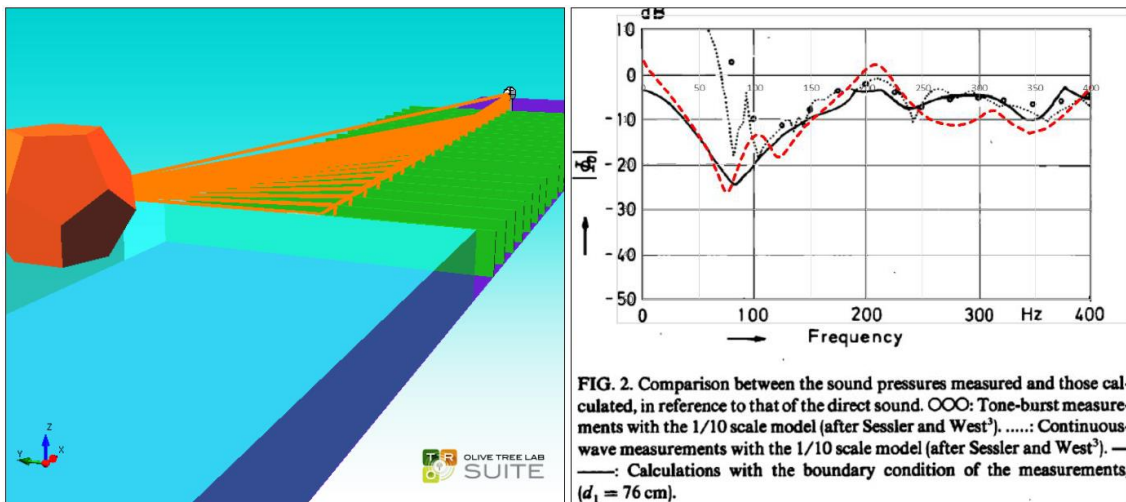
Figure 52. Left - The 3D full-scale model used for our calculations showing the source and 20 rows of seats with a spacing of 82 cm. Microphone height 110 cm. Right - Ando's results compared to experimental data. Our calculations are superimposed as a red curve over the original graph by Ando.

102

was first observed during the period 1960 - 64. Ando used their results to compare his calculation methodology with measured data. Our calculations are superimposed as a red curve over the original graph by Ando.

The model of the theatre used for additional validation purposes, is the Pattichion Theatre completed in Limassol, Cyprus in 2015. Figure 53 shows on the left a 3D model of the theatre, while on the right a photograph of it.
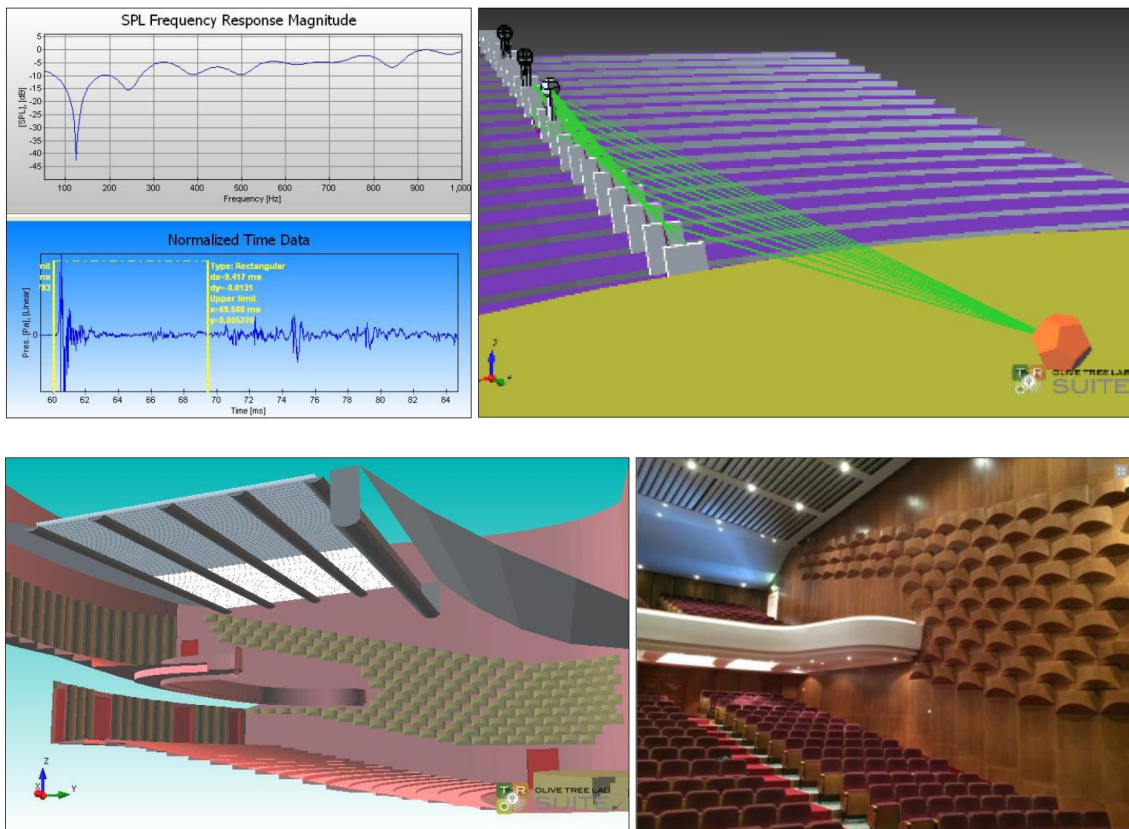
Figure 53. Left - 3D model of the Pattichion theatre. Right – Photograph of the theatre.

Figure 54 below shows the measured seat dip effect close to the middle of the 10th row after applying approximately a 10ms rectangular window to the measurement results. Since the seat dip effect is more pronounced in the first 20ms, the only participating surfaces in the 3D model, are the seats, the steps and the stage of the Pattichion theatre. The source height is 2.00m from the bottom of the stage, while the receiver at 3.40m. There are 19 seat rows in the theatre having a distance of 86cm between each row, while each row has 28 seats. The floor has two seat slopes which are, 10cm/step for the first 8 rows and 16cm/step for the rest.
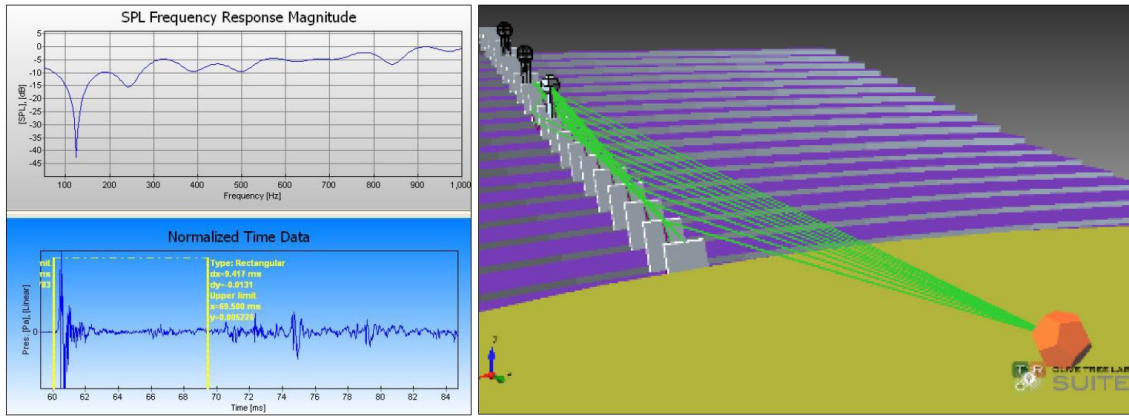
Figure 54. Left - Measured SDE and the windowed impulse response. Right - The model showing the sound rays to the microphone of the 10th row of seats, the steps and the stage.

Figure 55 shows a comparison between the measured and calculated results. From the graph, it may be seen that the measured seat dip effect is located at around 120Hz while the calculated SDE is found around 105 Hz.
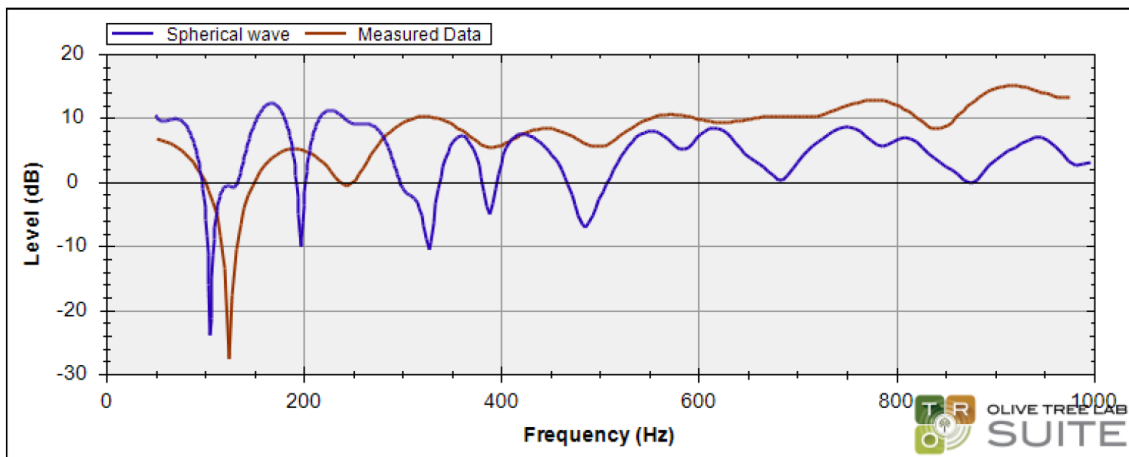
Figure 55. The SDE effect calculated using spherical wave propagation and how it compares to the measured results.

Figure 56 below shows a comparison between the calculated SDE using spherical wave propagation used in our model and plane wave propagation. It may be seen that plane wave propagation fails to capture the seat dip effect and it shows the importance of using the spherical wave reflection coefficient in calculating sound reflections.
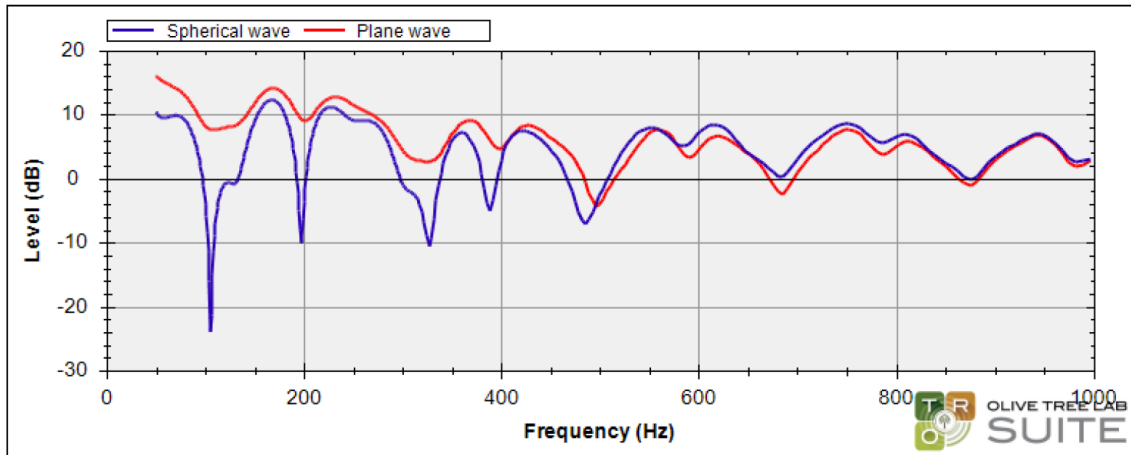
Figure 56. The SDE effect calculated using spherical and plane wave propagation.

3.4.4.2 Conclusions

The above results demonstrate that WBGA provides an accurate and fast alternative solution in studying wave phenomena in theatres such as the seat-dip effect. Any discrepancies reported above between calculated and measured results are expected since sound interference phenomena depend on the geometries of the experiments as well as the details in sound measurement procedures.

We have demonstrated that the WBGA approach has certain advantages over other wave-based methods. These are:

1. WBGA can very easily isolate each sound path or a group of paths and show their contribution both in the frequency and time domain over and above, to auralize isolated paths.
2. WBGA is faster than other numerical methods
3. WBGA is in many cases equally accurate as numerical methods
4. WBGA visually assists the understanding of physical processes

We have also demonstrated that geometrical acoustics using plane waves for reflection coefficient calculation cannot calculate accurately sound wave phenomena such as the seat-dip effect. In contrast, WBGA with spherical wave propagation can better reproduce this effect.

Finally, sound rays in WBGA simulate sound propagation in a three-dimensional environment with a possibility of eventually including all phenomena deemed important in acoustics. They carry information on how to lose intensity with distance, how to

reflect, diffract and transmit when they encounter objects and how to interact with the atmosphere.

3.4.5 Wind Turbine Noise Prediction

To evaluate the accuracy and efficiency of our model in outdoor calculations, a joint project between us and SIXSENSE Environment took place, aiming to compare the calculation results of our model with measurement results from wind farms. Wind farms where chosen as they are the ideal case study for evaluating the effects of atmospheric absorption and atmospheric refraction. The results of our calculation model were first compared against the benchmarks cases in (Attenborough, et al., 1995) which we will refer to as the 1995 benchmark cases, and some of the benchmark cases in (WP2 Team, 2002), which we will refer to as the Harmonoise benchmark cases. The 1995 benchmark cases include analytical solutions for linear sound speed profiles, but they only apply for monochromatic frequencies. The Harmonoise benchmarks cases are made in a 1/3 octave frequency resolution and include comparisons to the modern engineering prediction scheme Nord2000 (2019). They also include logarithmic sound speed profiles, thus allowing us to test the capabilities of our model in linearly approximating logarithmic sound speed profiles. An outlook of the benchmark cases used follows. Popular commercially available noise mapping packages like CadnaA (CadnaA – state-of-the-art noise prediction software, 2020), SoundPlan (SoundPlan, 2020) and LimA (Environmental Noise Modeling and Mapping Software – Predictor-LimA, 2020) do not account for the effect of sound refraction, therefore we did not compare our calculations with theirs.

3.4.5.1 1995 Benchmark Cases

The 1995 benchmark cases consist of four cases corresponding to different atmospheres: a homogenous atmosphere with uniform sound speed (Case 1), a non-homogenous atmosphere with a strong positive linear sound speed gradient of 0.1 (Case 2), a non-homogenous atmosphere with a strong negative linear sound speed gradient of -0.1 (Case 3) and a composite sound speed profile (Case 4), which was not used as it exceeds the capabilities of our model. Full details and descriptions of the cases can be found in (Attenborough, et al., 1995). In the original study, only the analytical, fast field program (FFP) and parabolic equation (PE) methods of all the cases were presented.

The original paper intended to develop benchmark cases of extreme atmospheric conditions but without the inclusion of effects such as turbulence, rough ground or uneven terrain. This would allow simple versions of new numerical methods to be tested against these benchmarks before being expanded to include other physical phenomena.

In the three cases considered, calculations were performed for source-receiver ranges of up to 10000 m. The calculations were performed for three monochromatic frequencies: 10, 100 and 1000 Hz. Here we present the results for Case 2 and Case 3 at a range of 10000 m and a frequency of 100 Hz. The receivers were separated by 25 m.

The ground impedance was described using the Delany and Bazley 1 parameter model with a Flow resistivity of 205000 Pa s m^{-2} as opposed to the 4-parameter model used in the benchmark paper. The parameters used in the model are summarized in Table 4.

Parameter	Value
Density of air (ρ_0)	1.205 kg/m^3
Atmospheric Pressure	1 atm
Relative Humidity (RH)	70 %
Temperature (T_0)	22 ºC
Ground Flow Resistivity (σ) (D&B)	205000 Pa s m^{-2}
Source Height (h_s)	5 m
Receiver Height (h_r)	1 m
Range (R)	10000 m
Frequency (f)	100 Hz

Table 4. Parameters used for 1995 Benchmark Cases

1.1 Harmonoise Benchmark Cases

Our calculation model was compared against Case 1.1 of the Harmonoise benchmark cases. This case consists of a flat ground with uniform impedance for different Source-Receiver heights and Ranges. In total there are 144 different subcases. The atmospheric conditions used in the subcases under investigation are summarized in Table 5 below.

Index m	Atmospheric condition	Sound speed profile

m = 2	Linear sound speed Profile, no turbulence	$a = 0.05$ s^{-1}, $c(z) = c_0 + az$
m = 3	Logarithmic sound speed profile, no turbulence	$b = 1$ ms^{-1}, $c(z) = c_0 + b\ln(1+z/z_0)$
m = 5	Logarithmic sound speed profile, no turbulence	$b = -1$ ms^{-1}, $c(z) = c_0 + b\ln(1+z/z_0)$

Table 5. Atmospheric conditions used in the Harmonoise Benchmark subcases

Due to a large number of subcases in case 1.1 the subcases were narrowed down to the ones consisting of a non-homogenous atmosphere, the ones that did not include atmospheric turbulence (thus the ones which have an index m = 2, 3 and 5). The subcases consist of a locally reacting ground (grass), a range of 2000 m and a source/receiver height combination of $h_s = 0.5$ m with $h_r = 1.5$ m and $h_s = 5$ m with $h_r = 4$ m. These source/receiver height combinations were chosen to test the linear approximation of a logarithmic profile when the sources and receivers are close to the ground and far from the ground.

Thus, the list of subcases considered is: C11_2132m and C11_3232m where the index m corresponds to the atmospheric conditions m = 2, 3 and 5. The parameters used for all the subcases are outlined in Table 6 below.

Parameter	C11_21322	C11_21323	C11_21325	C11_32322	C11_32323	C11_32325
Source height (m)	0.5	0.5	0.5	5	5	5
Receiver height (m)	1.5	1.5	1.5	4	4	4
Range (m)	2000	2000	2000	2000	2000	2000
Speed of sound (ms^{-1})	340	340	340	340	340	340
Roughness constant (m)	0.1	0.1	0.1	0.1	0.1	0.1
Ground Flow Resistivity (Pa s m^{-2})	200000 (Grass)	200000 (Grass)	200000 (Grass)	200000 (Grass)	200000 (Grass)	200000 (Grass)

Table 6. Modelling Parameters used in the Harmonoise Benchmark Cases

Our calculation model is compared to Basic and Engineering models, which are given below with their acronyms. The Basic models are, the Crank-Nicholson Parabolic Equation method (CPE TNO), the Green's Function Parabolic Equation method (GPE CST), the Fast Field Program (FFP CST) and for the subcases with a linear sound speed profile the Meteo-BEM (MBE CST) model. The Engineering models are the Nord2000 propagation model (N20 DEL) and the CRAYL model (CRA DEL). The distinction between Basic and Engineering models was made in (WP2 Team, 2002) and it applies to the rest of the work. More details of these models can be found in (WP2 Team, 2002).

3.4.5.2   *1995 Benchmark Cases Comparison*

Good agreement was found between our model and the FFP, PE and analytical solutions used in the 1995 Benchmark Cases. Figure 57 demonstrates a calculation comparison with Case 2 on the left and Case 3 on the right. In Case 2 which represents the downward refracting atmosphere, our calculations follow the trend quite well, although the minima and maxima are significantly sharper than the 1995 Attenborough Case, especially at large ranges. Nevertheless, in a more realistic scenario, these minima and maxima would most likely be smoothed out by turbulence. In Case 3, there is a discontinuity present at a range of about 400 m indicating that the receiver is now in the shadow zone where the transmission loss drops sharply.
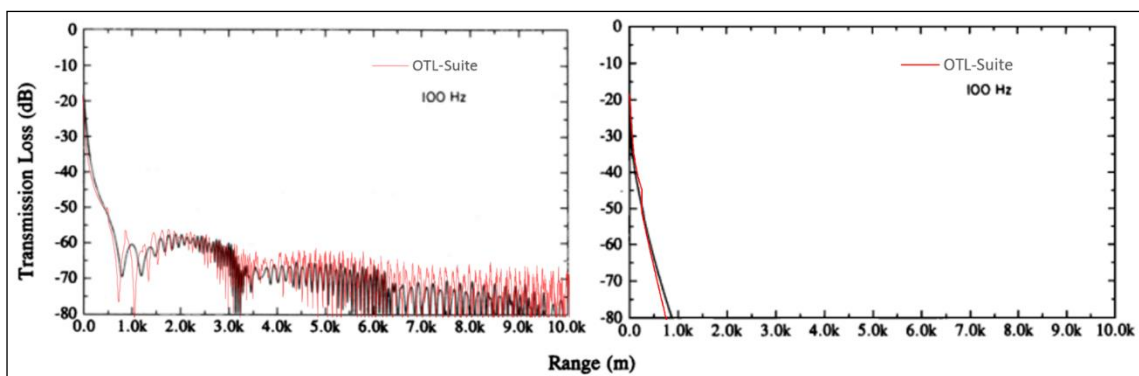
Figure 57. Comparison between our calculations (red line) and 1995 benchmark cases (black line). The left graph is for the case of a strong positive linear sound speed gradient of 0.1 s-1 while the right graph is for the case of a strong negative sound speed gradient of -0.1 s-1. Both curves show transmission loss vs distance at 100Hz. Calculated graphs are superimposed on published data**.**

Figure 58 below shows some of the sound ray paths from the source to receivers located at a range of 5000-7000 m.
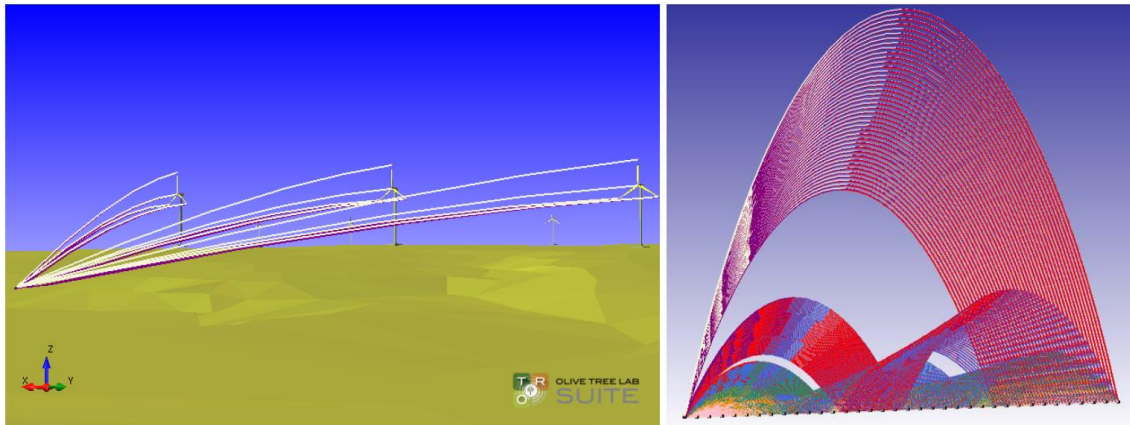
Figure 58. Left - View of the 3D model for 3 wind turbines. Right - Some of the sound ray paths between source and 80 receivers for the 1995 benchmark case 2. The receivers are located at a range of 5000 – 7000 m**.**

3.4.5.3   *Harmonoise Benchmark Cases Results Comparison*

The results for the Harmonoise Benchmark subcases are shown in Figure 59 below. Calculations, obtained using our model, are plotted using the purple line. For the subcases where the source and receiver are close to the ground (0.5 m and 1.5 m respectively) a good agreement with both basic models and engineering models is found for the case with linear refraction (Subcase C11_21322). Once a logarithmic profile is assumed, the results of our model and the engineering models deviate from the basic models (Subcase C11_21323) significantly. There is always a frequency shift between the interference minima. This is to be expected because since our model and the engineering models use a linear approximation for the logarithmic profile, the path length and time differences will be different leading to a shift of the interference minima.

For the subcases where the source and receivers are further away from the ground (5 m and 4 m respectively) there is a better agreement between our model and the basic models for the logarithmic cases (subcases C11_32323) in the low frequencies although there are still high deviations. This is to be expected because of the shape of the logarithmic curve. As the source and receiver move away from the ground, the linear approximation better matches the logarithmic one.

There is also a discrepancy between our model and the engineering models in all of the subcases. This can be explained by the fact that the engineering models are single bounce models that only consider two paths whereas OTL-Suite implements a multiple bounce model. The discrepancy occurs because at long ranges there will be a significant number of paths for downward refractions which the single bounce models of the engineering models do not take into account.

For subcases C11_21325 and C11_32325 where the receivers are in the shadow zone there is a large deviation between the engineering models and the basic models with OTL-Suite displaying a closer agreement with the basic models.
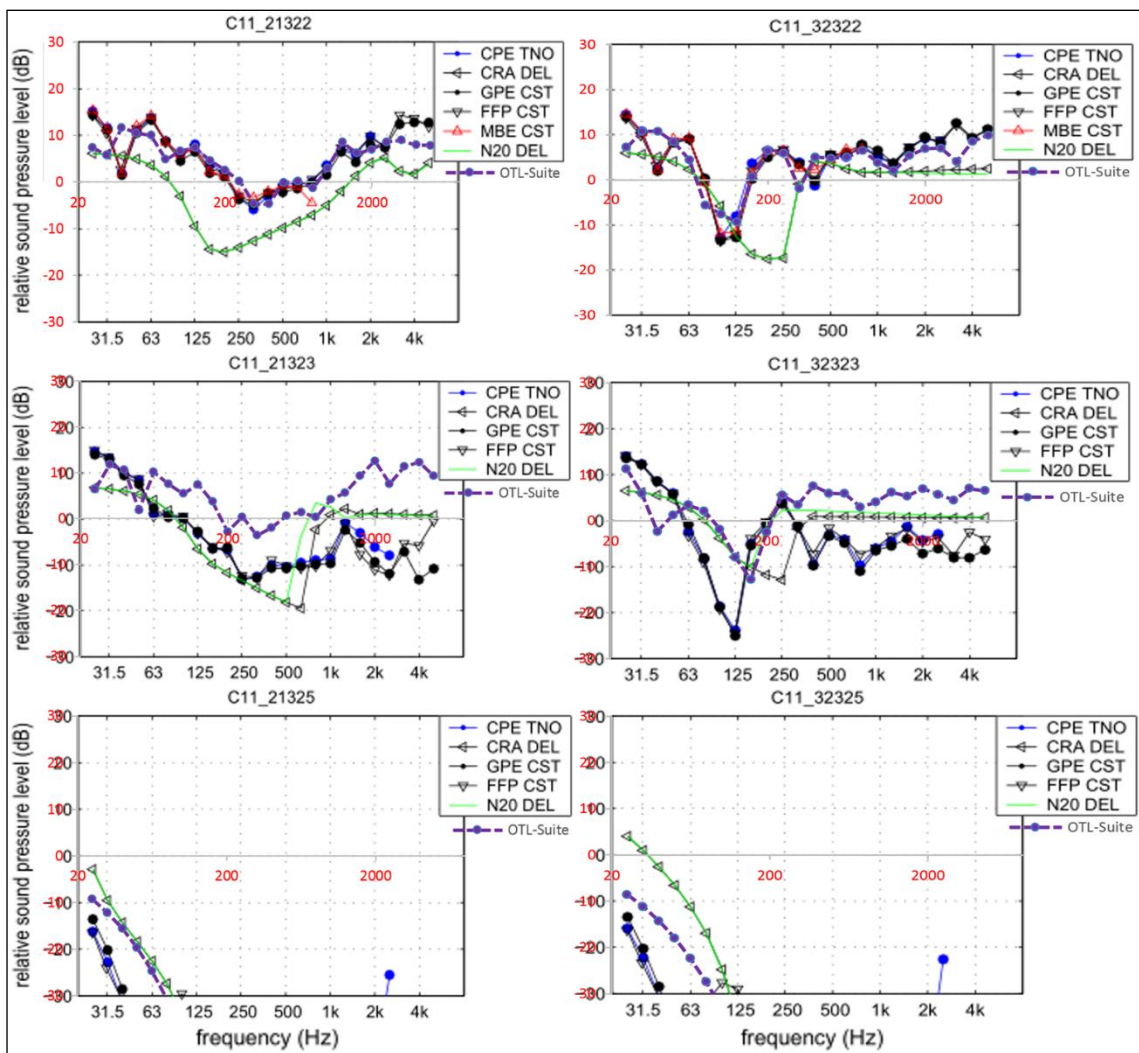
Figure 59. Our calculations (purple dashed line) vs Harmonoise Benchmark subcases. Calculated graphs are superimposed on published data.

3.4.5.4 Comparison with Sound Measurements

For the case of wind turbine noise, the comparisons between our calculations and measurements were made in 2 steps. In the first step, we used the loudspeaker measurements, which were made in the framework of the validation of Nord2000 (Plovsing & Kragh, 2009). This step is interesting because the loudspeaker was positioned at a height of 50m, which is comparable to the height of the noise sources of a wind turbine. The parameters used for these cases are detailed in Table 7.

Parameter	Delta Case 1	Delta Case 2	Delta Case 3	Delta Case 4
Source Height (m)	50	50	50	50
Receiver Height (m)	2	2	2	2
Ranges (m)	456	1020	412	912
Temperature at Ground ($^{\circ}$C)	4	4	4	4
Temperature Height z (m)	10	10	10	10
Temperature at Height z ($^{\circ}$C)	4.25	4.25	4.25	4.25
Wind Speed Height z_u (m)	10	10	10	10
Wind Speed at Height z_u (ms^{-1})	4.2	4.2	4.2	4.2
Wind Direction relative to Sound Propagation Direction (degrees)	0 (downwind)	0 (downwind)	180 (upwind)	180 (upwind)
Roughness Constant (m)	0.015	0.015	0.015	0.015
Ground Flow Resistivity (Pasm^{-2})	400000	50000	50000	50000

Table 7. Parameters used for the DELTA validation cases.

In the second step, our calculations were compared to noise measurements around a wind farm consisting of 6 wind turbines (hub height 80m). This test case was chosen because in some meteorological configurations (high wind shear in stable atmospheric conditions) the background noise is more than 10 dB lower than the WTN noise, even at ranges of 500m from the wind turbines. High wind shear also has the advantage that it results in a low wind speed near the ground reducing the wind disturbance on the microphone.

Due to the unpredictable range of atmospheric parameters in any given situation we propose a scatter plot of dB(A) values vs the atmospheric parameters for validating atmospheric acoustics.

3.4.5.5 *Comparison with loudspeaker measurements by DELTA*

In this test case, the loudspeaker was placed at a height of 50m. The noise source's amplitude and directivity are known to be enabling the calculation of the excess propagation effect (the difference between the total sound level and direct sound) in 1/3 octave frequency resolution. Although (Plovsing & Kragh, 2009) used a ground Flow Resistivity of 200000 Pasm^{-2} there is great uncertainty about the modeled ground, therefore the value of the Flow Resistivity was adjusted to 400000 Pasm^{-2} for DELTA Case 1 and 50000 Pasm^{-2} for DELTA Cases 2, 3 and 4 in order to match the first interference minimum.

Figure 60 below presents the results of two ranges (approximately 500m and 1000m) for both downwind and upwind conditions. There is a good agreement for downwind propagation, and a good agreement in the upwind propagation. This is consistent with the comparisons with the Harmonoise benchmark cases described in Harmonoise Benchmark Cases Results Comparison.

It is difficult to analyze this case further, because of the reliability of the input data; some of the parameters, like temperature and roughness, had to be extrapolated from the graphical sound speed profiles available in (Plovsing & Kragh, 2009).
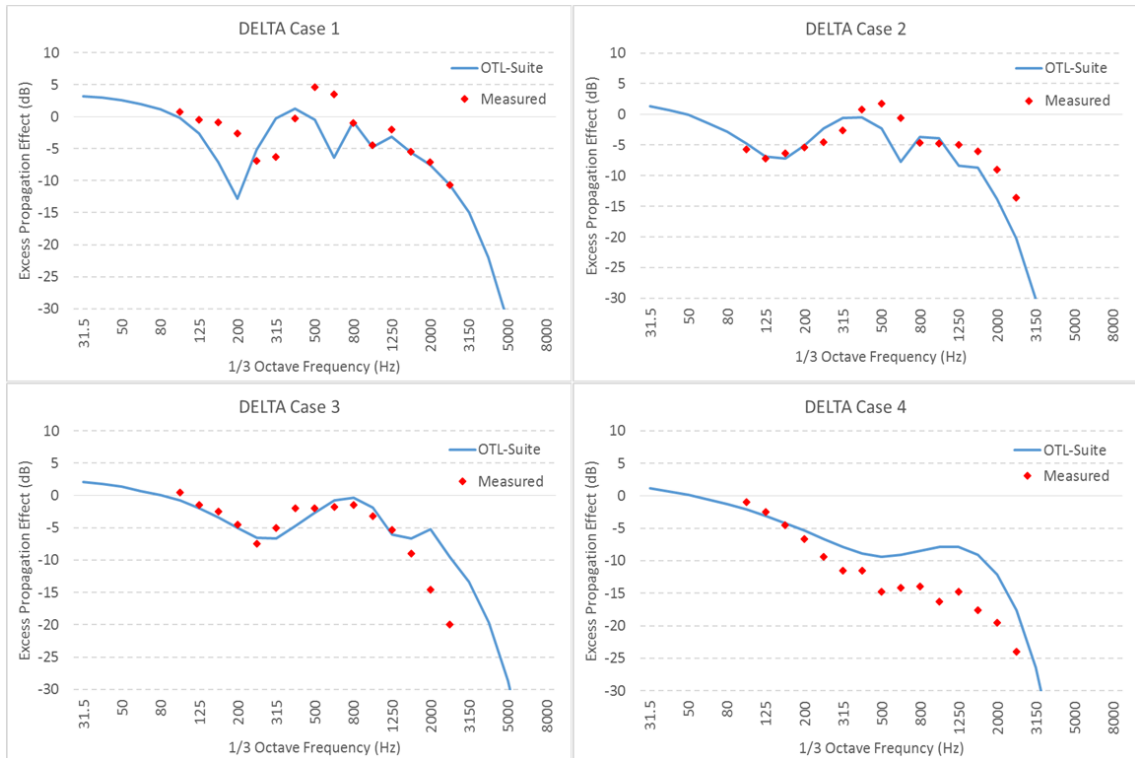
Figure 60. Measured and predicted excess propagation effect. Delta cases 1 and 2 are for downwind conditions while Delta Cases 3 and 4 are for upwind conditions. The source - receiver horizontal range is approximately 500 m for cases 1 and 3 and approximately 1000 m for cases 2 and 4.

3.4.5.6 Comparison with Noise Measurements around a Wind Farm

The wind farm that was investigated consisted of 6 wind turbines with a hub height of 80m and a rotor diameter of 90m. The meteorological measurements recorded were a) wind speed and wind direction at heights of 2m, 10m and the hub height of 80m b) temperature c) humidity and d) atmospheric pressure at heights of 2m and 10m. The microphones were positioned at a height of 1.5m and horizontal ranges of 150m and 500m from the wind turbines; measurements were done in a 1/3 octave band frequency spectrum and full audio spectrum for some locations.

Noise measurements are presented in L_{eq} for a horizontal range of 150m from the wind turbines and L_{50} for large ranges. The wind turbine is modelled as a point source. The sound power level of the source is available from measurement reports. There are three cases taken into consideration with the parameters outlined in Table 8 below.

Parameters	WTN Case 1	WTN Case 2	WTN Case 3
Source Height (m)	80	80	80
Receiver Height (m)	1.5	1.5	1.5
Range (m)	150	500	500
Temperature at Ground (°C)	10.7	4.1	3.6
Temperature Height z (m)	10	10	10
Temperature at Height z (°C)	10.732	4.382	3.757
Wind Speed Height z_u (m)	10	10	10
Wind Speed at Height z_u (ms^{-1})	6.8	5.0	4.4
Wind Direction relative to Sound Propagation Direction (degrees)	Downwind	Downwind	Upwind
Roughness Constant (m)	0.05 (shear factor 0.16)	0.91 (shear factor 0.28)	1.33 (shear factor 0.31)
Ground Flow Resistivity (Pasm^{-2})	225000	225000	225000

Table 8. Parameters used for the OTL-Suite model to compare against WTN measurements

The Excess Attenuation is first calculated in narrow frequency bands starting at 20 Hz in steps of 5 Hz until 500 Hz, where the steps switch to 20 Hz until at 10000 Hz. The frequencies of the Excess Attenuation are then combined into the center frequencies of a 1/3 Octave spectrum ranging from 25 Hz to 10000 Hz. The direct sound, which includes the source characteristics, is then added to the Excess Attenuation in the 1/3 Octave spectrum to obtain the Sound Pressure Level. This is then also combined into a 1/1 Octave spectrum and then given in dB(A) values.

Our model allows users to calculate the Excess Attenuation at extremely high resolutions (from 0,001 to 100.000 Hz at 0,001 Hz increments, in constant frequency steps or constant percentage steps). The resolution chosen here is a compromise between accuracy and performance.

A first comparison is presented in Figure 61 below for WTN Case 1, in a 1/1 Octave band frequency spectrum and 1/3 Octave band frequency spectrum in downwind conditions. We can see a good agreement between calculations and measurements at a range of 150m of the wind turbine, with almost the same interference minimum at about

125 Hz. This means that the sound power level taken as input data and the propagation model work fine, even in the point source approximation.
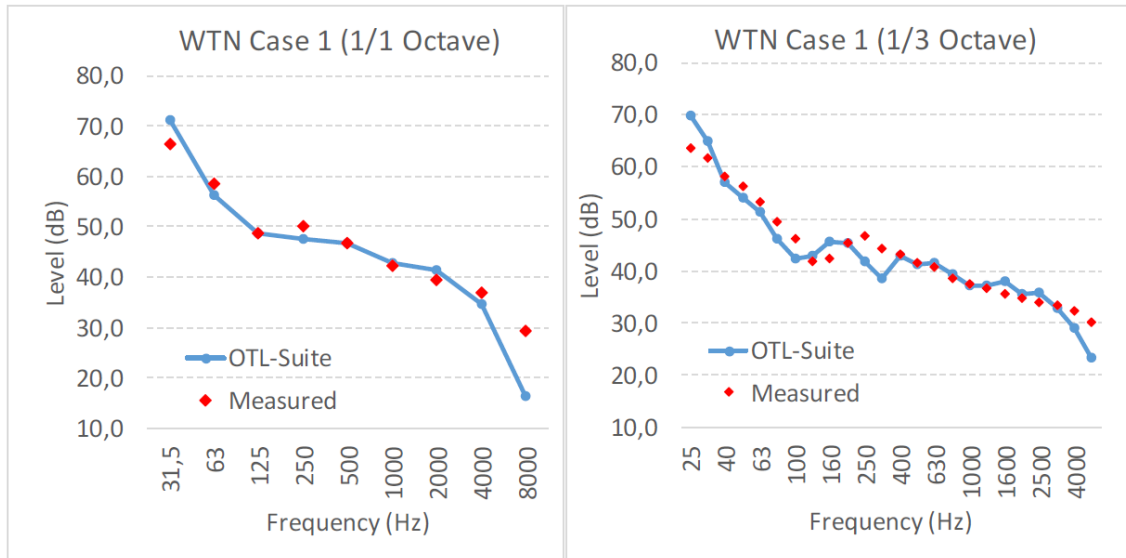
Figure 61. Measured and predicted noise level for WTN Case 1 in 1/1 band and 1/3 band. Downwind conditions with a range of 150m.

Figure 62 below presents the results for WTN Case 2, at a range of 500m from a wind turbine in downwind conditions. Calculations are presented in the 1/3 Octave band frequency spectrum and for a set of 10-minute meteorological data in dB(A). We can see a good agreement in the 1/3 Octave frequency spectrum with some small differences in the low frequencies under 40 Hz, which were also visible at a range of 150m. There is a particularly good agreement on the dB(A) scatter plot.
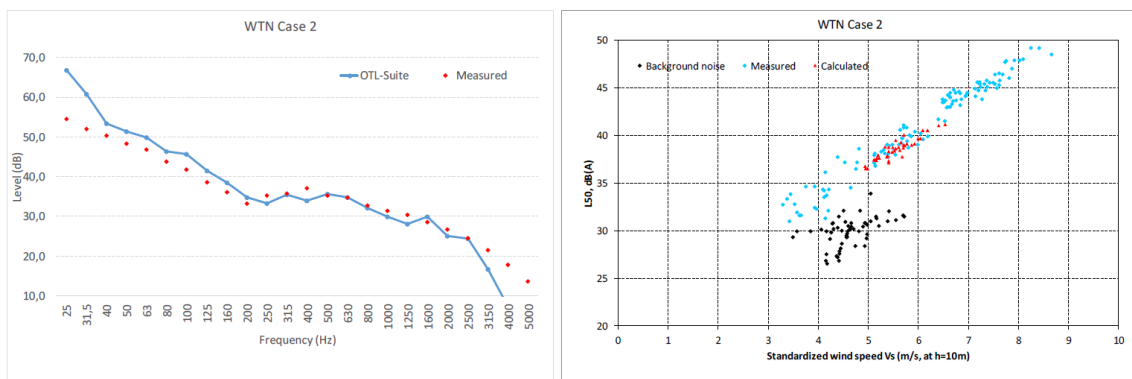
Figure 62. Measured and predicted noise levels for WTN Case 2 (left). Measured and predicted Noise Levels for Case 2 in dB(A) for a set of 10-minute meteorological data. Downwind conditions with a range of 500m (right).

Figure 63 below presents the results for WTN Case 3, at a range of 500m from a wind turbine in upwind propagation. On the left graph, we can see measured and predicted noise levels for Case 3. On the right graph, we can see measured and predicted noise levels for Case 3 in dB(A) for a set of 10-minute meteorological data.
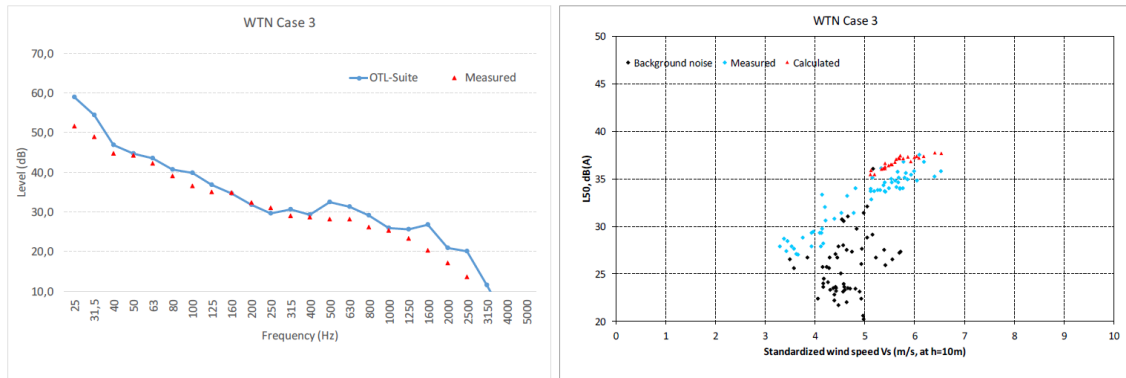
Figure 63. Measured and predicted noise levels for Case 3 (left). Measured and predicted Noise Levels for Case 3 in dB(A) for a set of 10-minute meteorological data. Upwind conditions with a range of 500m (right).

We can see some differences between measurement and calculation in the spectrum calculations, but quite a good agreement in the dB(A) scatter plot. However, the calculation results in dB(A) seems to correspond to the maximum of the measured values. This is consistent with the comparisons between our calculations and the benchmark cases in Sections 3.4.5.2 in 3.4.5.3. Our model seems to overestimate the high frequencies at long ranges compared to the basic models. It should also be noted that if the receiver is in the shadow zone for upwind conditions, our model will use the default XY plane as the ground and ignore the imported rough ground model. A rough ground would most likely further attenuate the sound pressure levels. Nevertheless, the calculated results are within an acceptable range to the measured ones.

3.4.5.7 Conclusions

The conclusion of this work is that the complexity of atmospheric dynamics cannot be fully represented by a single practical engineering model. This is already demonstrated in the Harmonoise validation reference. The main source of discrepancy between measured and predicted data in ray models is the approximations used in calculating sound speed profiles. However, for engineering purposes, accuracy must be traded with calculation time and our model can deliver a good approximation of the measurement

results in acceptable calculation times. Ray models, implemented with multiple reflection paths, seem to be better suited as a compromise between accuracy and calculation time. Furthermore, sound ray paths allow for the visualization of sound propagation.

Future work in this area could include the study of subsonic noise propagation which allows calculations of infrasound. Noise sources could be modelled as moving dipole and quadrupoles sources instead of monopoles, allowing for more realistic calculations, including the calculation of modulation effects. It would also be worthwhile to compare more measurements with further developments of WBGA to include phenomena such as the semi-analytical model for full logarithmic sound speed profiles (Salomons E. M., 1994), the effects of caustics (Salomons E. M., 1998) and the more recent model of the effect of turbulent scattering of acoustical energy into the shadow zone (Lam Y. W., 2009).

4 Speed Improvements Using Intelligent Prioritization

In Chapter 3, we presented a model that improves the accuracy of geometrical acoustics methods and we demonstrated these improvements by comparing our calculations with other models as well as measurements. In this chapter, our focus is shifted into improving the performance of sound detection algorithms, which take most of the time during an auralization calculation. Our improvements are based on an intelligent prioritization of path detection. This work is focused on reflection detection, but we conject that our findings apply to any tree traversal detection algorithm. This chapter is divided into three parts a) the investigation of the effect of tree traversal type on the sound path detection algorithm performance b) the implementation of an algorithm based on intelligent prioritization and c) the application of prioritization in our model for room acoustics calculations.

4.1 Effect of Traversal Type on Algorithm Performance

This part of our work is focused on investigating the effect of tree traversals on sound rendering algorithms based on geometrical acoustics (Charalampous & Michael, 2014). The motivation behind this investigation was to see if we can change the performance of a tree traversal algorithm by changing the traversal type. We compared three different traversal types using an image source algorithm and we compared the number of image sources detected on four different geometrical models based on the time the algorithm runs.

4.1.1 Tree Traversals in Geometrical Acoustics

As explained in chapter 2, tracing techniques can be represented in computational terms as a tree data structure. In the case of the image source method, an image of the source is created for each reflecting surface, forming this way the first level of nodes in the tree. Following on, all images in the first level of the tree are used to create second-order images, representing second-order reflections. This process continues until an interruption criterion is met, such as the maximum depth of the tree, the distance of an image source to the receiver or any other criterion set by the algorithm. The sound at the listener is computed based on the reflections derived by the tree traversal. In a similar way, all other tracing techniques could be represented as trees. Beams and frusta

intersect with polygons, which then become new nodes that recursively shoot new beams and frusta until an interruption criterion is met. The same logic applies for ray tracing and particle tracing algorithms. The tracing problem can be represented in the form of a tree traversal problem. This fact implies that the solution could be found by using a tree traversal algorithm. Tree traversal algorithms are widely studied in the domain of artificial intelligence and a lot of variants exist but they are mainly divided into two major categories, depth-first tree traversals and breadth-first tree traversals (Russell & Stuart, 1995).

In the case of geometrical acoustics, the tree to be traversed can be either constructed during or before tracing. This decision has important implications in the algorithm's performance. Preconstructed trees require memory allocation for the entire tree and predefined termination criteria like the depth of the tree. Also, preconstructed trees imply static geometries. On the other hand, dynamically constructed trees require less memory and allow dynamically set termination criteria but the dynamic creation of the nodes results in a performance overhead in the case the calculation is repeated many times for the same tree. Following on, a more detailed description will be given for each category, as well as for a subcategory of breadth-first variants, called "best-first approaches".

4.1.1.1   Depth-first Tree Traversal

A depth-first tree traversal algorithm is an algorithm where the nodes of the tree are expanded in depth as far as possible e.g. until an interruption criterion is met, before the algorithm backtracks to the previous nodes (Knuth, 1999). Depth-first algorithms come in many types, like preorder, postorder and inorder, defined by the order that the root is examined in relation to the left and right sub-tree. The most common type used in geometrical acoustics is the preorder depth-first approach. Figure 64 demonstrates the order in which the nodes of the tree are examined in the case of a depth-first preorder traversal.

The main benefit of a depth-first algorithm occurs in the case of dynamic tree construction. When a tree is constructed dynamically, implying that child nodes are added only after a parent node has been visited, then the memory requirements of this algorithm are minimal, as the only traversal related information needed to be stored in

memory at any time are the parent nodes of the visited node at each moment. This makes depth-first traversal memory efficient as well as fast because no search queue needs to be maintained. However, the main disadvantage of depth-first is the need for an a priori set termination criterion. Without a termination criterion, the tree will expand forever on the leftmost path of the tree. Consequently, the programmer or the user needs to set beforehand a termination criterion for the algorithm. This is a drawback for a real-time approach as we will show later.
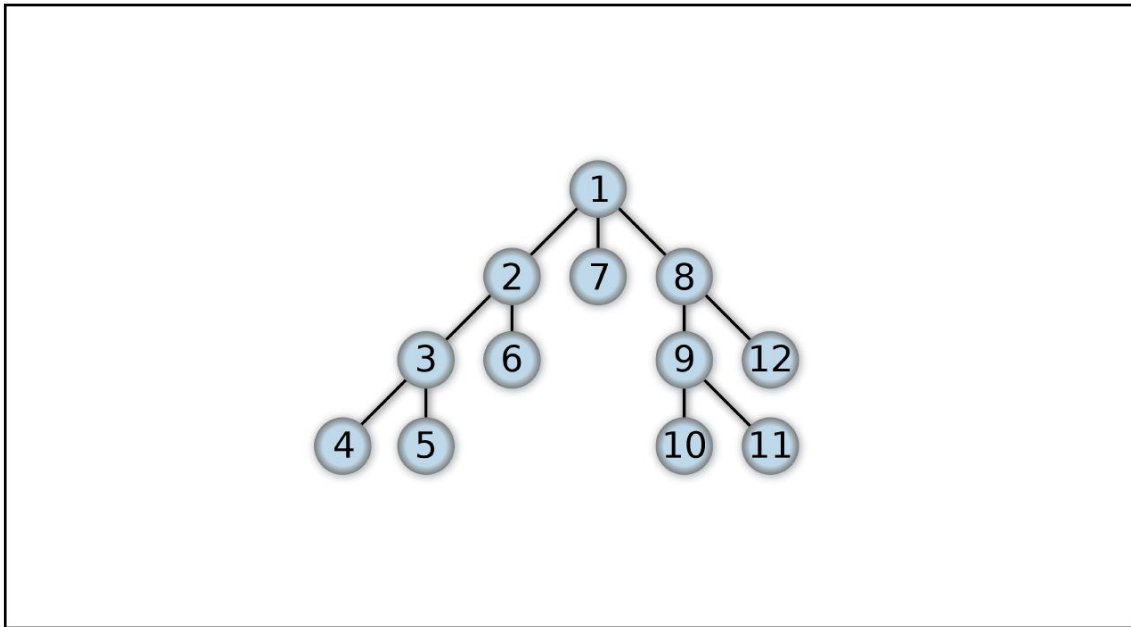
Figure 64. Representation of a depth-first preorder traversal.

4.1.1.2 *Breadth-first Tree Traversal*

In breadth-first tree traversal, the algorithm searches the tree in the following way. At the beginning, it first visits the root node. Then, it finds all the child nodes and adds them in a queue for examination. Following on, it recursively takes a node from the queue, examines it, and adds all its child nodes in the queue. This process results in an order of visiting nodes as the diagram shown in Figure 65. The main benefit of a breadth-first algorithm is that it can traverse all the width of the tree without an explicit a priori set termination criterion. Contrary to a depth-first algorithm, a breadth-first algorithm could traverse an infinite tree in infinite time, without a termination criterion. On the other hand, a major drawback of breadth-first search is the management of the queue. As the depth of the search deepens, the queue gets exponentially larger, making

the algorithm memory inefficient and unpractical for searches that require traversals in tall trees.
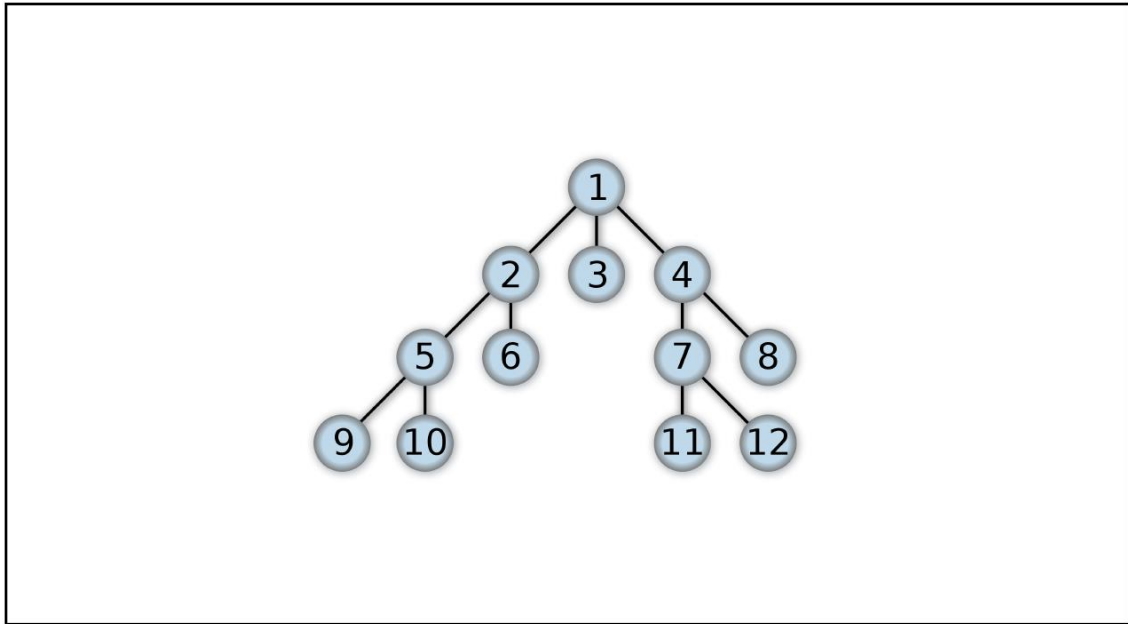
Figure 65. Representation of a breadth-first traversal.

4.1.1.3 Best-first Tree Traversal

Best-first tree traversal is a mutation of breadth-first tree traversal. It follows the same principles as breadth-first, except that its queue is a priority queue. In a priority queue, nodes are not de-queued in "First In First Out" (FIFO) order but they are based on a priority function. The outcome of the priority function depends on the node that it evaluates, the problem to be solved, the information gathered by the search up to that point on any extra knowledge we might have about the problem (Russell & Stuart, 1995). This way the algorithm expands each time the most promising node, based on a specified rule.

4.1.2 Validation of Tree Traversals

We have used our image source algorithm for the detection of specular reflections in three variants, for each respective traversal as described above, to evaluate the qualitative differences of the three different types. The image tree is constructed dynamically at run time. Thus, we avoid preconstructed trees that impose a priori boundaries on the search process. We ran the algorithms on four configurations with

different geometrical characteristics and we compare the results. The aim of the comparison was to investigate how these algorithms compare in detecting valid images over time and how the traversal type affects the outcome. We decided to make this type of comparison to evaluate the different approaches in relation to real-time requirements where time constraints can significantly affect the outcome of the search process.
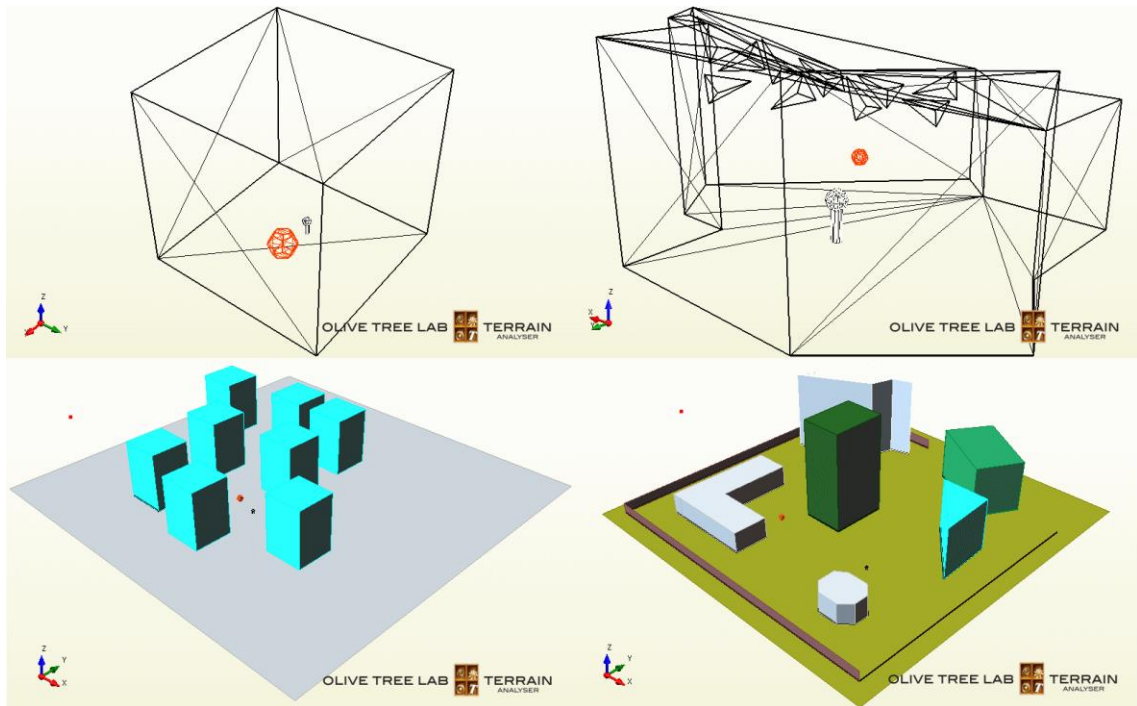
Figure 66. Configurations. Top Left: Cubic Room (6 polygons). Top Right: Choir Room (58 polygons). Bottom Left: Urban Environment (42 polygons). Bottom Right: Outdoor Environment (44 polygons)

We chose four different geometrical configurations shown in Figure 66, aiming at representing the best way possible typical scenarios where real-time sound propagation calculations could take place. Following on, we present the results for each case. For the depth-first approaches, we have set a termination criterion based on the maximum reflection order, as this is a requirement for a sensible execution of the algorithm, as described above. In order to compensate for the need to set a maximum reflection order in the depth-first case, we ran the algorithm with three different maximum orders and compared the outcomes with the other two cases to evaluate how this decision affected the performance. Then, for breadth-first and best-first search, we took the number of valid images detected by the depth-first search with the highest termination order and set it as a termination criterion i.e. if depth first execution for the highest order yielded

1200 valid images, then we executed the breadth-first and best-first algorithms until 1200 images were detected. Charts in Figure 67 Figure 68 Figure 69 and Figure 70 show the results of running the algorithms for each environment respectively. Charts in Figure 68 Figure 69 and Figure 70 have been trimmed up to a specific time to allow better visualization.

4.1.2.1 Priority Function

For the case of the best-first algorithm, we had to use a priority function to guide the algorithm. We decided to use a heuristic priority function, based on information gathered from the parent nodes of each evaluated node. The selection of the priority function was based on the empirical observation that in closed rooms, surfaces with lower order reflections tend to have more higher order reflections than surfaces with no lower order reflections. For example, it was observed that a surface reflecting a first order reflection to the receiver had more probabilities to reflect a second order reflection a well when compared to a surface that did not have a first order reflection.

As a result, the priority function used is the following

$$f(n) = 10VAi + Pio$$

Equation 52

where VAi (Valid Ancestor images) is the number of nodes that are ancestors to the node under investigation, that created valid reflections to the receiver and Pio (Parent image order) is the reflection order of the parent node. We consider VAi as a good indicator of the importance of the current node because the more valid parents a node has, the more likely the node is valid too. The factor of 10 is added so we can add the parent image order as the last digit to be used in the case of equality. For example, if for two nodes the VAi equals to 3 and the one represents a 6th order image and the other a 7th order image, then the node at the lowest order will have a priority of 35 while the highest order one will have a priority of 36. Thus, the 6th order node will be assigned a priority. This priority function has been selected for its ease of implementation and from empirical observations that it provides a decent prioritization, without implying that this is the best possible priority function.

4.1.2.2 Cubic Room

The first model under investigation was a cubic room with dimensions of 10m X 10m X 10m. We chose to start with a cube as the simplest common geometrical structure resembling an indoor situation. The lowest bottom corner was at (0,0,0) and the opposite one at (10,10,10). We set the source at (4,5,1) and the receiver at (6,5,1). The maximum reflection order was 8, 9 and 10 for the depth-first searches. The maximum number of valid images for breadth-first and best-first was 1180. Figure 67 presents the results obtained for the three depth-first searches, the breadth-first, and the best-first search. We observe that depth-first searches have a linear pattern in the increase of valid image sources per time. On the other hand, in the case of breadth-first and best-first searches, we note that the rate of increase slows down over time. At this stage, it is important to highlight the difference in the performance of the three depth-first variants. A change in the maximum order termination criterion could change the performance of the algorithm by a great amount when comparing the valid image sources detected over time.
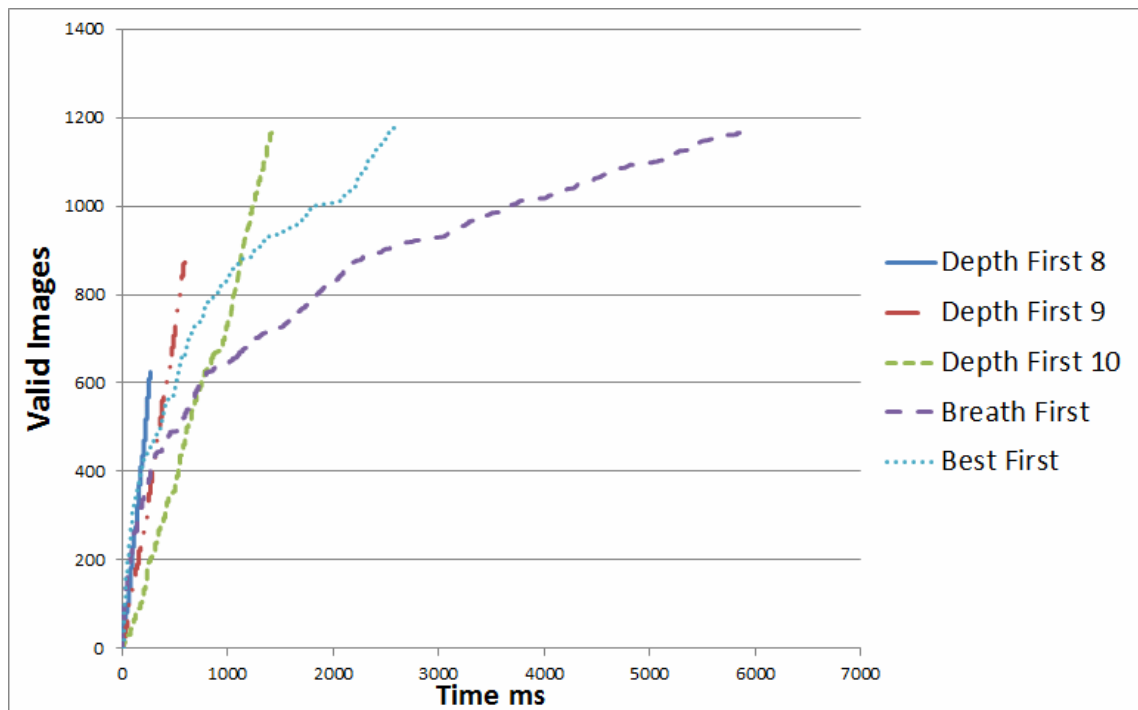
Figure 67. Images per time of execution. Cubic Room.

We will provide a detailed explanation of this phenomenon in the discussion section. When it comes to comparing best-first and breadth-first searches, as it would be

intuitively expected, best-first search outperforms breadth-first search. This is because best-first search is guided by the priority function. The general delay to reach the same number of images as the depth-first search is attributed to the management of the queue required in both cases.

4.1.2.3 Choir Room

The next space under investigation is a choir rehearsal room, as seen in Figure 66. The searches have been run with the same mindset as in the cubic room. The termination orders for the depth-first searches were 4, 5 and 6 orders respectively. The maximum paths for the breadth-first and the best-first searches were 337. In the case of the choir room, we can discern similar patterns as in the cubic room case. depth-first searches grow in a rather linear way and the performance is affected by the termination criteria while the performance of best-first and breadth-first deteriorates over time. Best-first still outperforms the breadth-first algorithm.
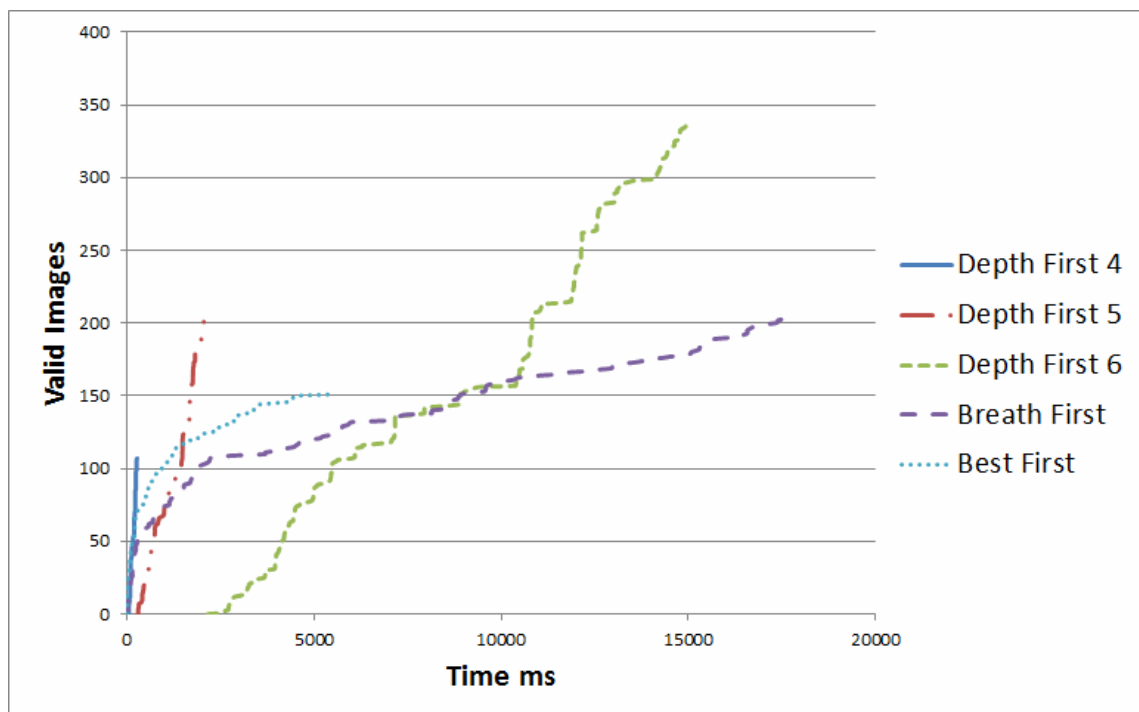
Figure 68. Images per time of execution. Choir Rehearsal Room.

4.1.2.4 Urban Environment

In the case of the urban environment, we choose a model that carries typical characteristics of environments found in urban topologies. More specifically, in a

modern urban setting, we can observe many cuboid-shaped structures aligned almost in parallel, with a lot of faces facing each other. Figure 66 shows the model used for this scenario. The termination orders for the depth-first searches were 6, 7 and 8 orders respectively. The maximum paths for the breadth-first and the best-first searches were 32.
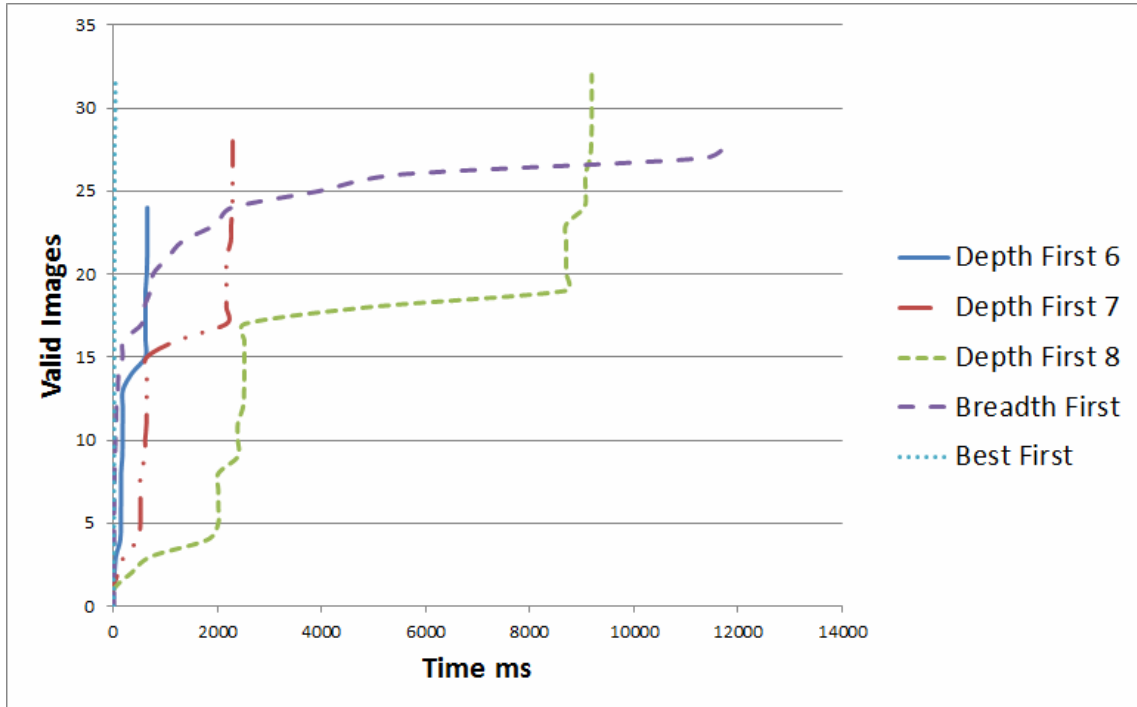
Figure 69. Images per time of execution. Urban Environment.

In this case, we see the patterns of behavior of the search algorithms change. The most important change is the rapid detection of valid image sources by the best-first approach. This is attributed exclusively to the priority function used. Environments of this type have many faces with nearly opposite normal directions. This contributes to the creation of repetitive reflections between these surfaces up to high orders. The priority function described earlier benefits from such occurrences and can detect these repetitive reflections very fast. As a result, we can see the explosion of the images detected by the best-first search in Figure 69. Other important remarks are the sharper growth of breadth-first during the first milliseconds and the sharper slowdown for the rest of the execution as well as the nonlinear behavior of depth-first searches and the dramatic slowdown in the case of setting the termination order to 8.

4.1.2.5 Outdoor Environment

The outdoor environment is an environment where various buildings are distributed through the space in a rather random way. This type of environment could resemble an industrial site or an army camp. The termination orders for the depth-first searches were 5, 6 and 7 orders respectively. The maximum paths for the breadth-first and the best-first searches were 56.
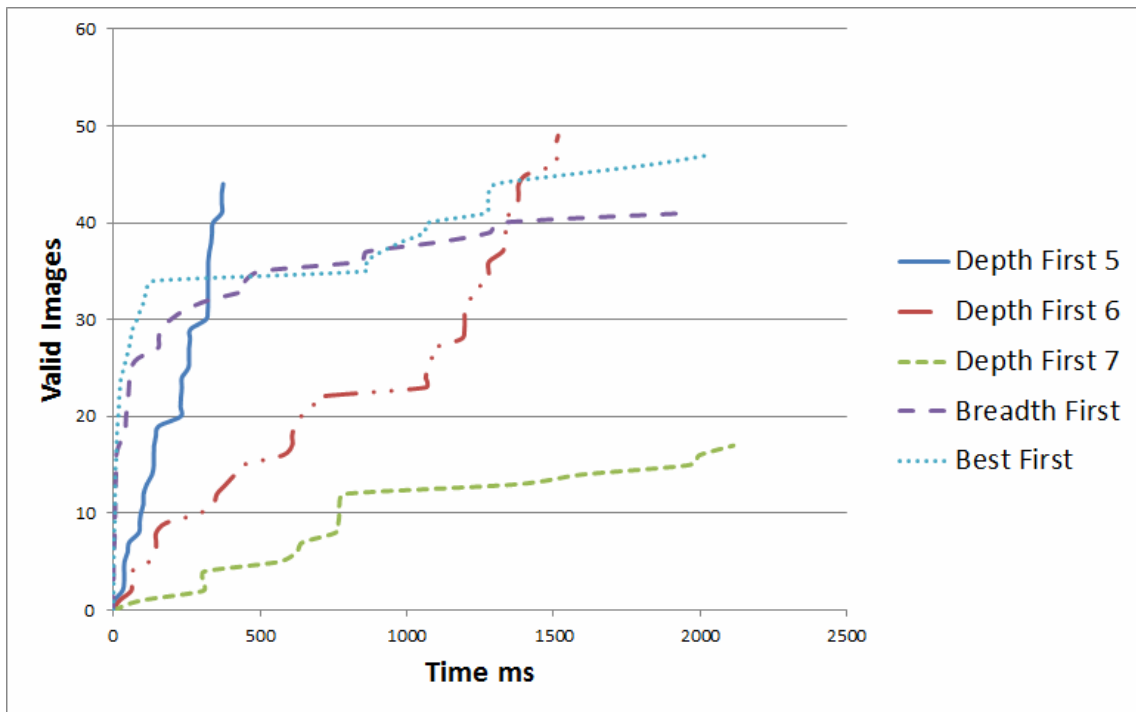
Figure 70. Images per time of execution. Outdoor Environment.

In this case, we can again see the following a) the rapid increase of both best-first and breadth-first algorithms during the first milliseconds of execution, b) the rapid decrease in their performance after a certain point c) the fact that best-first is outperforming breadth-first most of the time, except a small interval between 500 and 1000 ms and d) the fact that depth-first searches are highly influenced by the highest order termination criterion.

4.1.2.6 Discussion

The main outcome of this research is that different traversal algorithms have different behavior patterns, and this fact can be a catalytic factor for their applicability in different scenarios. In this section, we will discuss the algorithms used in this study by

highlighting the benefits and advantages of each algorithm as well as the pros and cons, as these have been concluded by the test cases described above.

Beginning with the depth-first search, we can point out its advantages which are a) simplicity in implementation b) memory efficiency c) the fastest traversal of the entire tree. Depth-first is simpler in implementation that the other two approaches as it requires only a recursive function without the need to maintain a queue. This fact also makes it memory efficient. This also results in a faster overall traversal of the entire tree, when compared to the other approaches. On the other hand, the main disadvantages are the following a) it requires a maximum depth to be set beforehand b) the rate of detecting valid image sources in the starting milliseconds of the algorithm is not as high as the other two. This can be explained by the fact that the ratio of valid images over the total number of images is higher at the top of the tree rather at the bottom while this doesn't hold true when you examine the distribution of valid sources from left to right. Thus, breadth-first and best-first have this characteristic shape of a curve, rapidly increasing in the first milliseconds while slowing down at the later stages, in contrast to depth-first which has a linear increase.

Based on the highlighted advantages and disadvantages, the depth-first algorithm is ideal for scenarios where a tree needs to be traversed up to a specified depth known beforehand and adequate time is available. Such a scenario could be for example software applications for room acoustics analysis. On the contrary, depth-first is not ideal for real-time applications such as video games and virtual reality. This is because, in the case of real-time scenarios, very strict time constrains exist and performance over time is an important component. In this case, depth-first suffers from two main weaknesses a) since a higher termination criterion needs to be set from the start, the algorithm can perform faster if a low, cut-off order is set or perform much slower if a high order is set (See for example Figure 70.). b) If the algorithm does not manage to search the entire tree within the real-time constrain, it might lose important low images, since the traversal examines the tree in a left to right order rather than in a bottom down manner.

The advantages and disadvantages of the depth-first approach can deductively lead us to the advantages and disadvantages of the other two approaches, breadth-first and best-first. We can see that even though memory requirements and the excessive slow down

over time make these approaches inappropriate for long-running in-depth searches, it makes them ideal for real-time sound rendering applications. This is because these approaches, having a top down approach in searching the tree, can detect the most important valid nodes, which are usually gathered in the higher part of the tree, in the first milliseconds of the search process. The top down approach is an inherent prioritization of the image sources within the structure of the tree and since prioritization is of major importance in real-time applications, they benefit by such an approach. Moreover, the higher density of valid nodes in the top parts of the tree provides a very good performance benefit to these algorithms during the initial time period of execution. Finally, the absence of a required termination order criterion removes the performance dependence from user decisions.

Furthermore, when the comparison is done between a best-first approach and a breadth-first approach, the use of a priority function offers an obvious benefit. Nodes that can be heuristically evaluated as more important are expanded before others, providing enhanced performance over time when compared to a simple breadth-first implementation. This benefit is vivid in all four comparisons we performed in this case study. As a result, it can be concluded that from the three algorithms compared, the best-first approach seems to have the best behavior when it comes to real-time sound rendering requirements.

4.2 Prioritized Monte Carlo Algorithm

Since we have established that changing the order we examine the candidate image sources can affect the quality of the calculation results, we decided to look further into prioritizing the examination of image sources, in order to improve the performance of path detection algorithms, to fit the needs of real-time execution. In this section, we show how altering the traversal method significantly affects the algorithm's performance. We propose a stochastic Monte Carlo algorithm, which involves optimizations based on prioritization. These optimizations alter the algorithm's behavior, providing better results for real-time purposes.

4.2.1 The Algorithm

Our proposed algorithm is based on a hybrid image source/ray tracing method (Vorländer, 1989), which is extended using prioritization rules. The original method proposed by Vorländer goes as follows:

    a.   A ray is emitted from the source and propagated through space.

    b.   As soon as the ray hits a surface, the surface's image source is generated and recorded.

    c.   The ray is reflected from the surface.

    d.   Steps b and c are repeated recursively until the ray intersects a predefined receiver sphere, as it would in a typical ray tracing algorithm.

    e.   The ray is neglected and the image sources recorded during the ray tracing are evaluated for their validity (Mechel F. P., 2002).

    f.   Steps a to e are repeated for all rays emitted from the source. The valid image sources are used for the estimation of the impulse response. The hybrid method presented above significantly improves the performance of the image source algorithm but when it comes to real-time sound rendering, it has an important drawback. Vorländer's tracing process terminates when:

        i.   the ray intersects the receiver sphere or

       ii.   when it reaches a certain energy level or

     iii.   a predefined traveling distance is covered.

In room-like enclosures, for which this algorithm was designed, this termination criterion works well, because, after some bounces on the wall, the ray eventually intersects with the receiver. But these criteria might not work well in other types of environments, indoor configurations with many rooms and outdoor configurations. The reason is because some rays could be shot in directions from where it is not easy to return to the receiver and until they meet the termination criteria and the tracing is interrupted, a lot of computation time is wasted. Most modern ray tracing implementations use one of the following termination criteria:

    a.   A limit in sound reflections allowed per path, meaning that the propagation of a sound ray is terminated after a certain number of

bounces has occurred and the receiver has not been reached (Taylor M. T., Chandak, Antani, & Manocha, 2009) (Taylor M. , et al., 2012) (Schissler, Mehra, & Manocha, 2014).

b. A minimum energy criterion where the ray propagation is terminated after its energy falls under a certain level (Savioja & Svensson, 2015) (Röber, Kaminski, & Masuch, 2007).

c. A maximum distance criterion where the ray propagation is terminated after the ray surpasses a predefined traveling distance (Dreher, Dutilleux, Junker, & others, 2012).

The termination criteria are usually set arbitrarily, e.g. ten orders of sound reflections or a maximum distance of 1000, without any further discussion or based on a guessed perceptual importance e.g. "sound paths that lose 60 dB are probably not affecting significantly the sound field".

We extend the above method by overcoming the issue of arbitrary set termination criteria and using intelligent adjustment during runtime. A high-level graphical description of the algorithm can be seen in Figure 71. The criteria adjustment takes place during the tracing procedure and it is independent of user preferences.
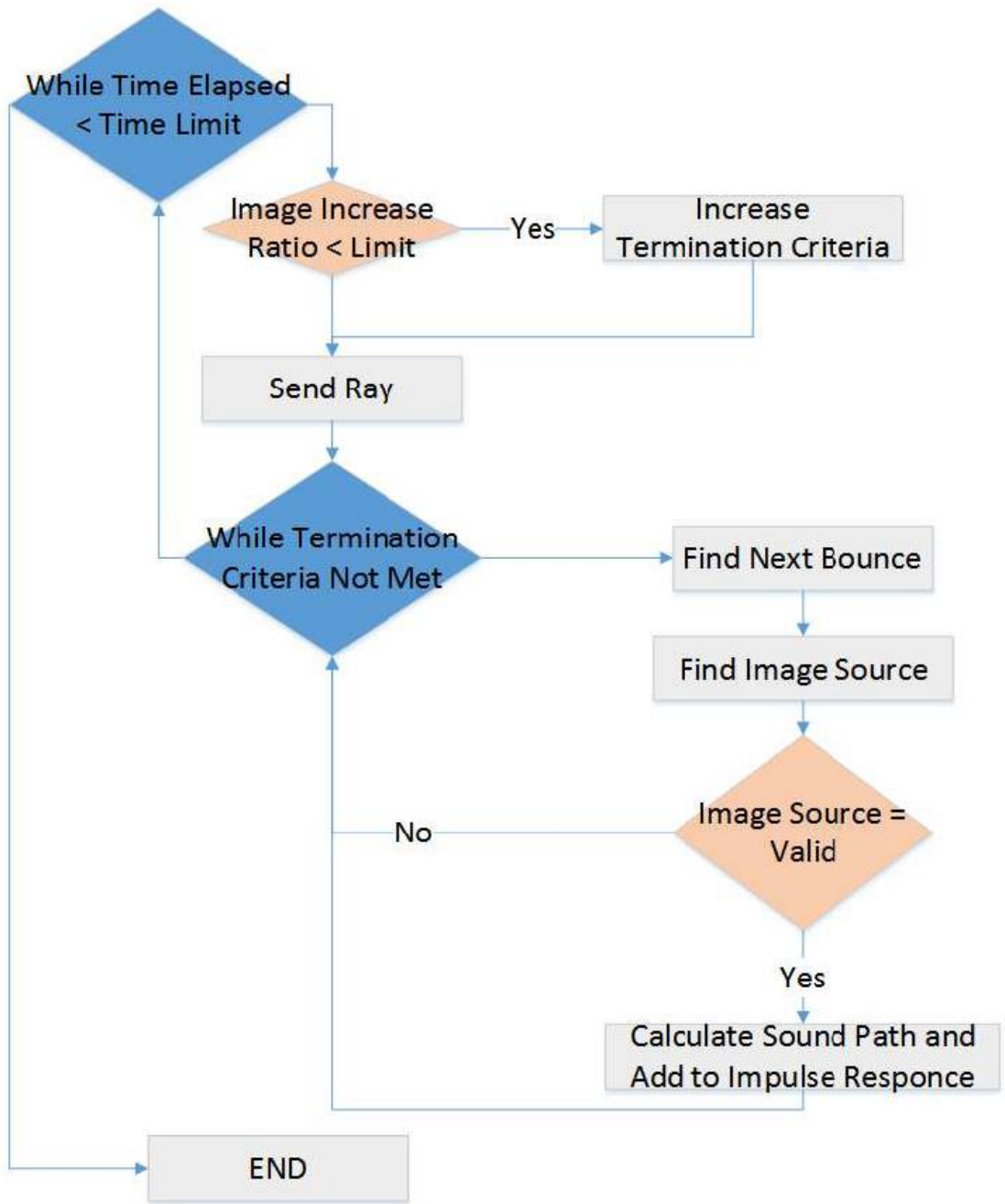
Figure 71. Flowchart of our new prioritized algorithm

4.2.2 Termination Criteria

Our algorithm uses the following three criteria 1) Tree depth (reflection order) 2) Parent validity 3) Sound pressure. In the following paragraphs, we explain in detail each termination criterion and we also explain the procedure of adjusting the termination criteria during runtime.

4.2.2.1 Tree Depth

There are two ways in which the image source order is important in an image source algorithm. Firstly, lower order images are usually stronger than higher order images since they are closer to the receiver and reflect fewer times, therefore losing less energy. Then, it is generally observed that each level of the image source tree has a lower density of valid image sources to total image sources than the previous levels (Vorländer, 1989) (Mechel F. P., 2002) (Mechel F. , 2012). This can be expressed by the following relationship

$$P(V_o) < P(V_{o-1})$$

Equation 53

Where V indicates that an image source is valid and o the image source order. The above expression can be phrased as **the probability of an image of order 0 to be valid is less than the probability of an image of order 0-1.**

Figure 4 and Figure 5 show an example of such a case. Figure 4 shows a simple configuration with a source, a receiver and three surfaces. We have detected the specular sound reflections up to the third order using the image source algorithm and displayed them in a 3D viewport. Figure 5 shows the image source tree of the specific configuration. In color, you can see the valid image sources. Within the node, the image source surface is displayed. The surfaces are represented by a number and are associated with Figure 4. By examining the nodes of the tree level by level, we can observe that the ratio of valid to total images is 3/3 for the first level, 4/9 for the second level and 4/27 for the third level. This behavior generally holds true for any 3D model. More information about this behavior of the image source method can be found in (Vorländer, 1989) (Mechel F. P., 2002) (Mechel F. , 2012)
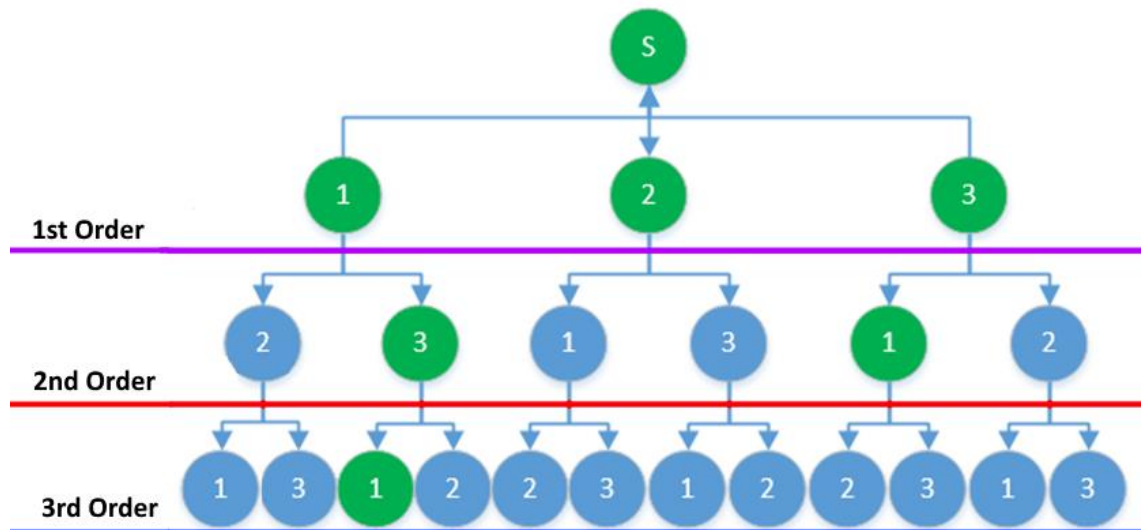
Figure 72. Tree Depth Termination Criterion. Each time the termination criterion for the maximum order is increased, the depth of the searchable tree is increased by one.

We ran a series of experiments to strengthen our claim. We ran an improved version of the image source algorithm (Mechel F. P., 2002) on eighteen different models. The models are displayed in Table 9. We used ten different shapes for our models, a box and nine letter-shaped rooms, to ensure adequate variety in geometrical settings. Then, for eight of the models that feature an occluded area, we used two different source-receiver configurations, one with a line of sight between source and receiver (LS) and one without. After that, for each case, we recorded the percentage of valid to total image sources for each order. The results are displayed in Table 10.

The first termination criterion is extracted by observing Table 11. We can observe that in the vast majority of cases, the valid image source density is higher in lower reflection orders. This means that if more rays explore the higher levels of the tree rather than the lower, there is an increased possibility of detecting valid image sources. In a tracing algorithm, where the rays continue their propagation through the environment until the termination order or the maximum distance criterion is met, when examining higher order images, the probability to generate a valid source decreases. Taking into account also the fact that lower ordered images contribute more to the sound field, as explained above, we start with a low maximum order termination criterion and by progressively adjusting it, we give priority to the higher parts of the tree at the beginning of the execution.
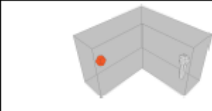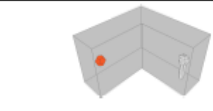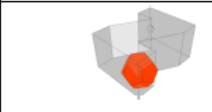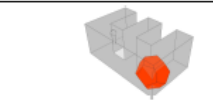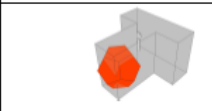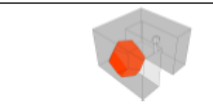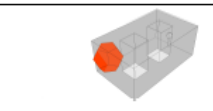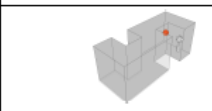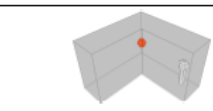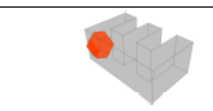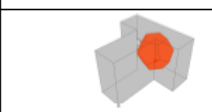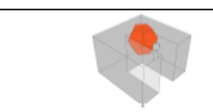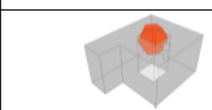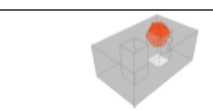
Box		Delta	
Sigma		Gamma	
Zeta		Epsilon	
Tau		Pi	
Ro		Theta	
Sigma LS		Gamma LS	
Zeta LS		Epsilon LS	
Tau LS		Pi LS	
Ro LS		Theta LS	

Table 9. Models used to investigate termination criteria. Source denoted with a red dodecahedron and receiver with a microphone.

Geometry	1	2	3	4	5	6
Delta	100 %	52.0 %	25.7 %	13.2 %	6.7 %	3.4 %
Box	100 %	44.4 %	14 %	6.3 %	1.9 %	1.0 %
Gamma	- %	- %	0.28 %	0.16 %	0.1 %	0.03 %
Sigma	- %	0.7 %	0.07 %	0.04 %	0.005 %	0.001 %
Zeta	- %	0.8 %	0.4 %	0.1 %	0.04 %	0.01 %
Epsilon	- %	0.7 %	0.1 %	0.05 %	0.01 %	0.002 %
Tau	-%	2.2 %	0.9 %	0.3 %	0.1 %	0.02 %
Pi	10 %	0.0 %	0.5 %	0.05 %	0.07 %	0.007 %
Ro	8.4 %	4.3 %	1.2%	0.3 %	0.05 %	0.02 %
Theta	- %	0.9 %	0.2 %	0.06 %	0.02 %	0.004 %
Sigma LS	28.6 %	7.75 %	0.4 %	0.2 %	0.02 %	0.005 %
Gamma LS	87.5 %	17.5 %	6.2 %	1.3 %	0.4 %	0.09 %
Zeta LS	50.0 %	9.0 %	1.7 %	0.4 %	0.1 %	0.02 %
Epsilon LS	35.7 %	8.33 %	1.3 %	0.3 %	0.04 %	0.008 %
Tau LS	60.0 %	14.2 %	2.1 %	0.6 %	0.1 %	0.03 %
Pi LS	50.0 %	14.3 %	2.9 %	0.8 %	0.2 %	0.04 %
Ro LS	45.5 %	11.0 %	1.6 %	0.4 %	0.07 %	0.02 %
Theta LS	50 %	9.3 %	1.2 %	0.3 %	0.04 %	0.009 %

Table 10. Percentage of valid images for each tree level as related with reflection orders.

Geometry	% VP children that are valid	% NVP children that are valid
Box	18.6 %	1.0 %
Delta	35.4 %	4.4 %
Gamma	8.2 %	0.04 %
Sigma	0.6 %	0.002 %
Zeta	2.9 %	0.02 %
Epsilon	4.3 %	0.003 %
Tau	1.8 %	0.04 %
Pi	1.2 %	0.02 %
Ro	4.9 %	0.02 %
Theta	4.7 %	0.005 %
Sigma LS	3.3 %	0.01 %
Gamma LS	8.5 %	0.18 %
Zeta LS	5.8 %	0.03 %
Epsilon LS	4.5 %	0.02 %
Tau LS	1.1 %	0.06 %
Pi LS	6.6 %	0.08 %
Ro LS	5.7 %	0.03 %
Theta LS	5.1 %	0.01 %

Table 11. Percentage of children of valid parents that are valid(left) and of children of non valid parents that are valid(right) up to the 6th order of reflection.

4.2.2.2 *Parent Validity*

The parent validity termination criterion assumes that the probability of an image source having a valid parent image source is higher than the average density of valid sources at the parent level. This can be expressed by the following relationship

$$P(V|PAR_v) > P(V|PAR_{NV})$$

Equation 54

Where V indicates that an image source is valid, PAR_v a valid parent source and PAR_{NV} a non-valid parent source. The above expression can be phrased as: **The probability of an image with a valid parent source to be valid is higher than the probability of an image with a non-valid parent source to be valid.**

The physical explanation of this criterion follows. A valid image source represents a sound wave generated from the sound source, which eventually hits the image source's surface and arrives at the receiver. This means that waves, bouncing from a surface and arriving at the receiver, have a higher probability of subsequently bouncing back from another surface and hitting the receiver again at a later stage than waves that have not encountered a receiver yet. Even if this assumption does not hold true for any possible geometry, this is something that can be intuitively accepted for room-like enclosures or geometries that have some room like properties, like parallel walls in (Vorländer, 1989) (Mechel F. P., 2002) (Mechel F. , 2012). In brief, we can assume that in an environment bounded by surfaces, a reflected wave that passes from a receiver position has more probabilities to bounce back to the receiver than a wave that does not pass from a receiver position.

In Figure 72, this can be demonstrated by taking the third level of image sources as an example. In this level 3 in 4 valid image sources have a valid parent source. When compared to the 4 in 9 valid image sources in the second level, the probability of an image source having a valid parent is higher than the probability of the parent being valid or not. An intuitive physical explanation of this fact is that it is more probable for the surfaces that reflect sound to the receiver to also reflect the sound to surfaces that also send the sound wave back to the receiver, than surfaces that do not reflect any sound to a receiver.

In a similar way to the first termination criterion, we ran a series of experiments to strengthen this claim. We ran the improved image source algorithm in the same room, like the enclosures for the first termination criterion. Then, we recorded the percentage of valid children for parent images that are valid and the percentage of valid children for parent images that are not valid. The results are displayed in Table 11.

Based on the results of this experiment, our second termination criterion is related to the fact that it seems more probable that a valid image source has a valid parent source than a non-valid one. Based on this, rays reaching a tree node with a non-valid image source

have fewer probabilities, to reach a valid child node than rays that reach a valid tree node. Therefore, we terminate ray propagation as soon as a maximum number of non-valid parent images has been reached within the tree path traversed while progressively adjusting the maximum number of non-valid images criterion and giving priority to the images that have more valid parents at the beginning of the execution.

4.2.2.3   Sound Pressure Attenuation

An improvement to previous studies (Charalampous & Michael, 2016) is the addition of a third termination criterion. A limitation of using only the first two termination criteria is that the algorithm becomes agnostic when it comes to the specific materials composing the 3D geometry. By evaluating only the maximum order and the parent validity criterion, the algorithm will behave in a similar way irrespective of the sound absorption of each surface. For this reason, we introduce a third termination criterion, which is the maximum sound pressure attenuation. Therefore, the tracing of a ray is interrupted whenever the pressure falls under a specific threshold. The relative sound pressure level termination threshold is initialized at a level equivalent to attenuation due to distance at 1000 meters. In each readjustment of the termination criteria, the minimum sound pressure threshold is decreased by adding the average distance between bounces up to that moment to the distance.

4.2.2.4   Termination Criteria Run-time Adjustment

The major difference of our algorithm, compared to traditional tracing implementations, is the adjustment of its termination criteria during runtime. In previous work (Charalampous & Michael, 2016) the termination criteria were adjusted whenever the number of consecutive failed rays (rays that failed to produce a valid image source) was surpassing the number of surfaces in the model. This was highlighted as one of the weaknesses of the approach due to the arbitrariness of the method and was indicated as a subject of future research. In the current work, we change the adjustment method using a less arbitrary approach. Our current method is based on comparing the consecutive failed rays to the ratio of the number of all evaluated images over the number of all valid images detected until the time of the comparison. If the number of consecutive failed rays surpasses the ratio then this is an indication that the tracing has

reached a saturation point and the termination criteria are increased. The procedure is outlined in detail in the following pseudocode.

```
RayCount = 0
MaxDistance = 1000
MinP ressure = 0
FailedRaysT hreshold = SurfaceCounter
MaxNV PI = 0
MaxOrder = 0

while Cunnert Time < Termination Time do
        if RayCount > SurfaceCount & ConsF ailedRays > FailedRaysT hreshold then
        FailedRaysT hreshold = EvaluatedImages=V alidImages
        ConsF ailedRays = 0
        MaxOrder = MaxOrder + 1
        MaxNV PI = MaxNV PI + 1
                if PathsCount > 0 then
                        if MaxDistance = 1000 then
                                MaxDistance = AvgBounceDistance() _ 2
                        else
                                MaxDistance = MaxDistance+AvgBounceDistance() _ 2
                        end if
                        MinP ressure = 1=(MaxDistance=(AvgBounceDistance()_2))
                end if
        end if
Continue Tracing
.
.
.

end while
```

As outlined above, we increase the maximum order criterion and the maximum non-valid parent images (MaxNVPI) criterion by one each time the consecutive failed images surpass the threshold value. We also decrease the minimum pressure based on the average distance between bounces.

4.2.3 Criteria for Evaluation of Algorithmic Performance for Real-Time Sound Rendering

Real-time sound rendering algorithms are usually executed on a variety of hardware configurations and with a variety of input parameters, like the number of three-dimensional entities to be processed and the properties of these entities. The criteria that define a good algorithm for real-time purposes are a subject that is missing from the

literature. The performance of algorithms is usually evaluated by comparing the execution times for the traversal of a given part of the tree. For example, two hypothetical algorithms A and B are compared on the amount of time required to detect sound paths in a geometry up to a specific order of reflection. But this fact alone is not a sufficient indicator that can determine which of the two algorithms is better to use since there are other factors to be taken into account as well. For example, it needs to be verified that both algorithms deliver the same results and that the difference is located only at the execution time, something that is not always true especially for stochastic algorithms. Therefore, we attempt to define an optimum real-time sound rendering algorithm as an algorithm that approaches the ground truth solution i.e. measured data, as fast as possible, regardless the hardware configuration and the model to be simulated. This behavior should be ideally observed on a range of acoustical parameters that are perceived by a listener. For the purpose of this study we used the following criteria, number of sound paths, excess attenuation and reverberation time. Following on, we briefly describe these criteria.

4.2.3.1 Number of Detected Sound Paths

The number of paths is the number of valid direct and reflected sound paths, from source to the received that have been detected.

4.2.3.2 Excess Attenuation

The excess attenuation expresses the relation of the sound pressure level at the receiver when compared to the sound pressure of the direct path between the source and the receiver. We calculate the excess attenuation using the following equation

$$EA = 10log \frac{\int_{t_0}^{\infty} p^2_{total}(t)dt}{\int_{t_0}^{\infty} p^2_{direct}(t)dt}$$

Equation 55

where p^2_{total} is the total sound pressure at the receiver and p^2_{direct} is the pressure of the direct sound path arriving at the receiver at time t.

4.2.3.3 Reverberation Time

Reverberation time expresses the time required for sound energy to decay by 60 dB as described by the following equations (ISO, 2008)

$$RT = \frac{60}{a}$$

Equation 56

Where a is the slope for the function

$$y = ax + b$$

calculated using the least squares method of the Schröder integration

$$E(t) = \int_{t}^{\infty} p(t)^2 dt$$

where $p(t)$ is the relative sound pressure at time t.

4.2.3.4 Experimental Execution and Validation Models

To evaluate our our improved prioritized hybrid (IPH) algorithm, we compared it against other popular tracing algorithms. To make valid comparison, we had to compare algorithms developed on the same technology stack, to be sure that any differences in performance are of pure algorithmic nature. Hence we compared the algorithm's performance to the original hybrid algorithm (HT) without prioritization criteria, a previous implementation of the prioritized algorithm (FPH) (Charalampous & Michael, 2016), a typical ray tracing (RT) algorithm, which has a pretty straight forward implementation, and a ground truth solution. The comparison of our method with beam tracing method does not falls under the scope of this thesis because because the comparison is not between our method and the beam tracing method but between

prioritized and non-prioritized methods. Any improvement achieved for the HT algorithm could be transferred to a beam tracing algorithm as well.

For the comparison, we used four different 3D models, each with different characteristics, to cover as many different scenarios as possible. The models are the following:

1. **Shoe-box model.** We used a shoe-box model which is the typical scenario in room acoustics calculations. It has six surfaces and all of them face each other.

2. **Multi-room indoor model.** We used an indoor environment consisting of many interconnecting rooms, resembling a typical scenario found in virtual reality and video-game environments. It has 44 surfaces but most of them are occluded from the source as well as the receiver.

3. **Outdoor model.** We used the outdoor model, as used in (Charalampous & Michael, 2014) for comparison with previous methods. It has 44 surfaces and many of them are occluded from the source as well as the receiver. Also, the area is not bounded in all directions, resulting to sound escaping in the environment.

4. **Elmia Theatre.** The Elmia theater was used in the 2nd Round Robin for room acoustics (Bork I. , 2000). Our model has 1908 surfaces. Even though most of the surfaces are not occluded by any obstacle, large parts of its walls are composed of protrusions thus, allowing few specular reflections to exist while most of the sound field is scattered.

In contrast with (Charalampous & Michael, 2016) where infinite material impedance was considered, we apply a random absorption coefficient on each surface, which is held constant between executions of different algorithms. This allows us to evaluate the addition of the minimum sound pressure criterion introduced in the IPH algorithm and how it compares with the FPH algorithm.

We chose a source-receiver position for each model, which would resemble a realistic scenario for that case. For example, in the Elmia Theater, we placed the source on the stage and the receiver in the middle of the audience. We ran each algorithm for 5 seconds. We compare all results with a ground truth solution. The ground truth solution was obtained by running the IPH algorithm for five minutes. We implemented the code

in C# and run the evaluation tests on a computer with an Intel Core i5-4200M Processor @ 2.50GHz.
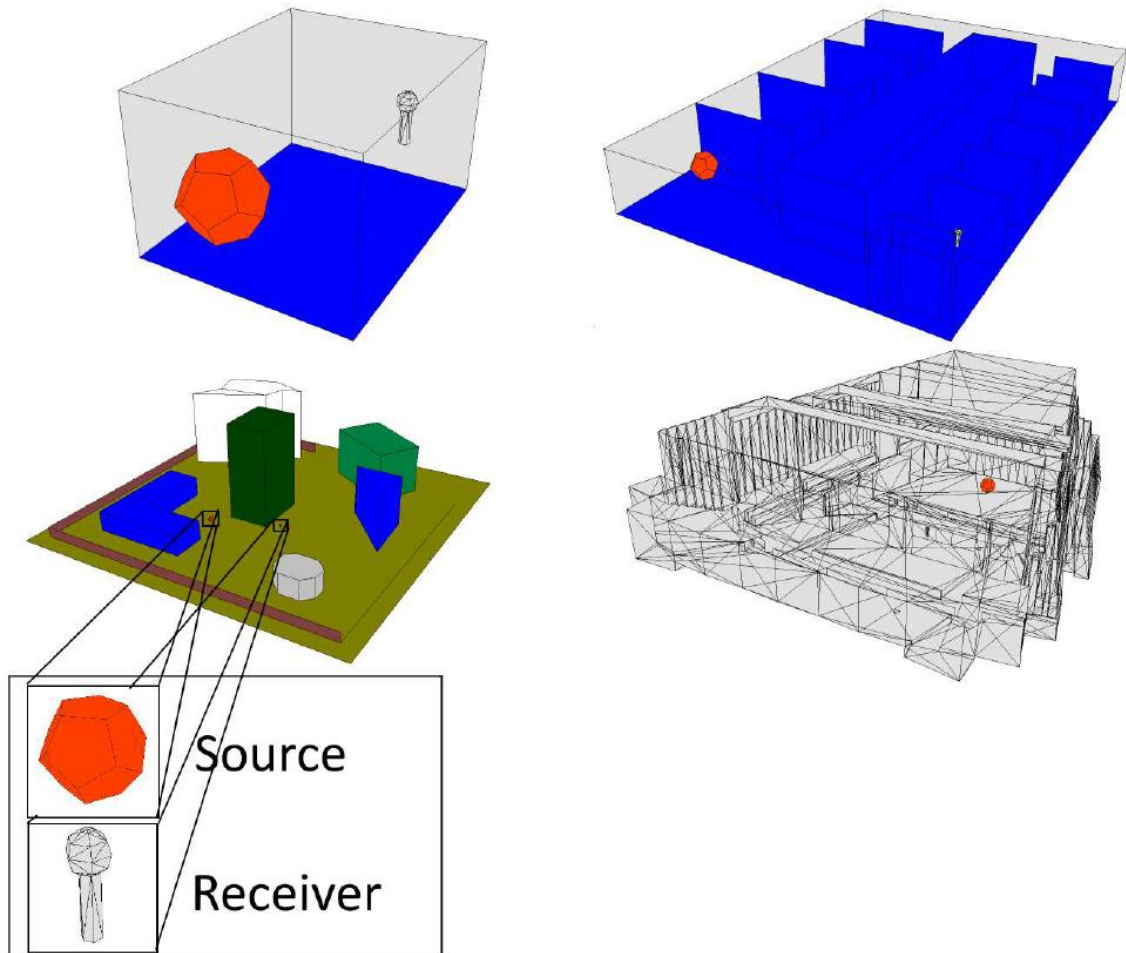
Figure 73. The 3D geometries used for validation a. Shoe Box model (top-left) b. Multi-room indoor model (top-right) c. Outdoor model (bottom-left) d. Elmia Theater (bottom-right).

4.2.4   Results and Discussion

4.2.4.1   Shoe Box

In Figure 74, Figure 75 and Figure 76 we see the results of running the four algorithms on the Shoe-Box model. We observe that FPH and IPH perform better than the other two on excess attenuation, as they approximate much faster the ground truth result. The difference varies from 2-5 dB for the largest part of the execution, a difference that can be considered perceptually important. IPH seems to perform slightly better than FPH.

In the reverberation time comparisons, FPH and IPH approach the ground truth solution much faster than the other two, even though a slight deviation is noted during the later

parts of the execution. In the number of paths detected over time IPH performs better than the rest during the execution period.
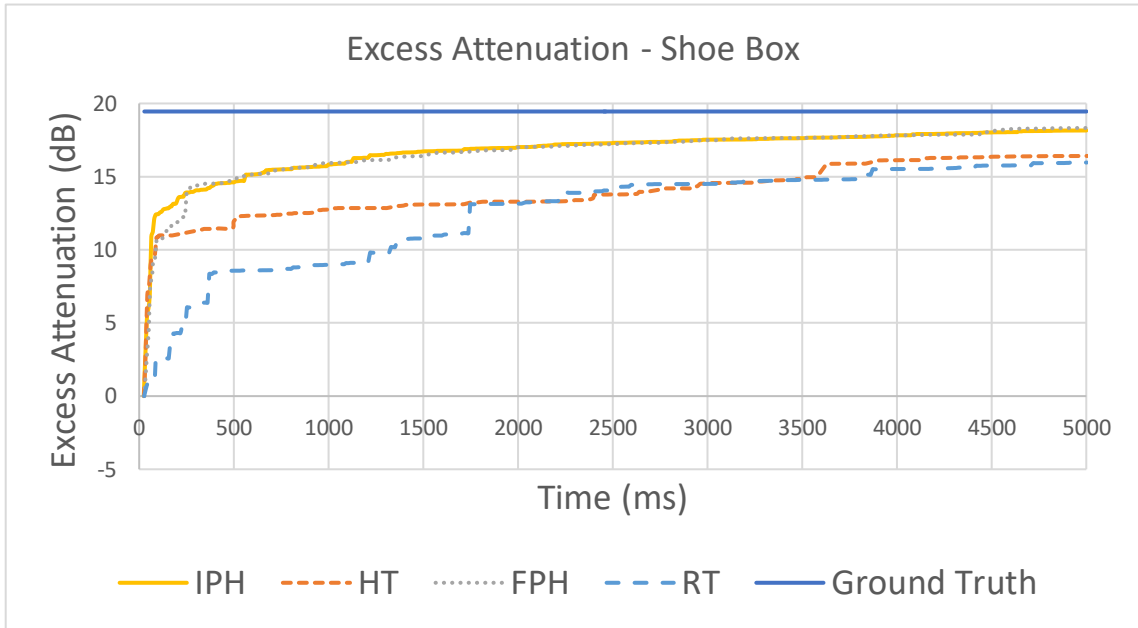
Figure 74. Excess attenuation for shoe box model.
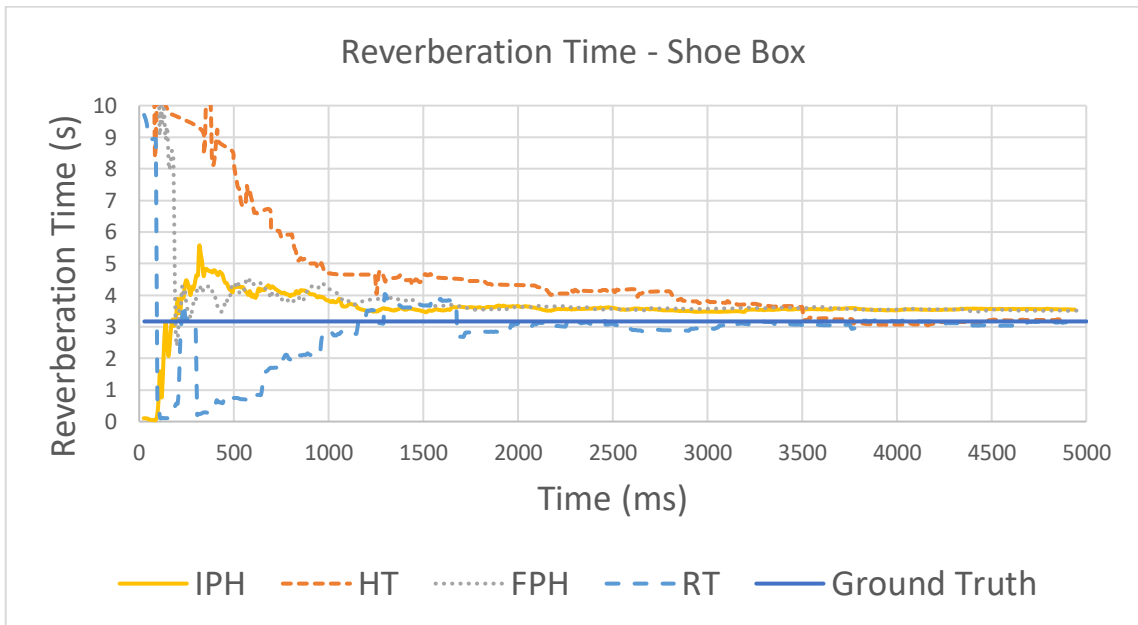
Figure 75. Reverberation time for shoe box model
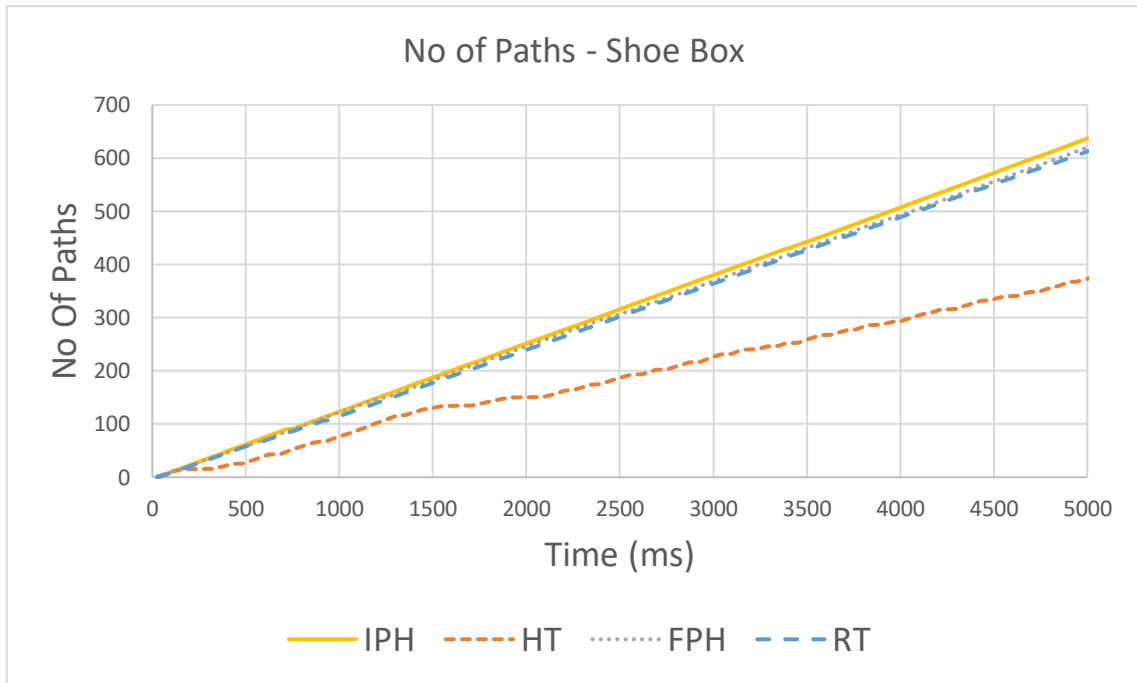
Figure 76. Paths for shoe box model

4.2.4.2 Multi-room Indoor Model

Figure 77, Figure 78 and Figure 79 display the results of running the four algorithms on the Multi-room indoor model. We highlight again that FPH and IPH perform better than the other two on excess attenuation as they approximate faster the ground truth result. Again, IPH performs slightly better than FPH and hybrid tracing.

When it comes to reverberation time, none of the algorithms outperforms the others clearly since they all calculate a fluctuating reverberation time between 280 - 350 milliseconds for most of the duration of the execution. Comparing the number of paths detected IPH outperforms the rest at all stages of the execution.
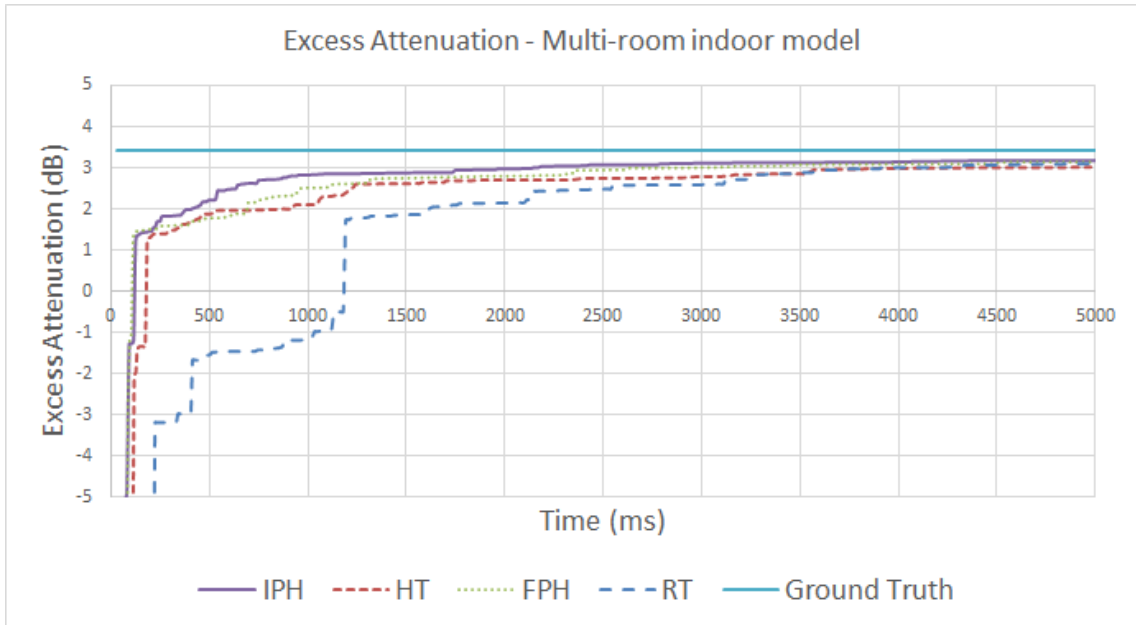
Figure 77. Excess attenuation for Multi-room indoor model.
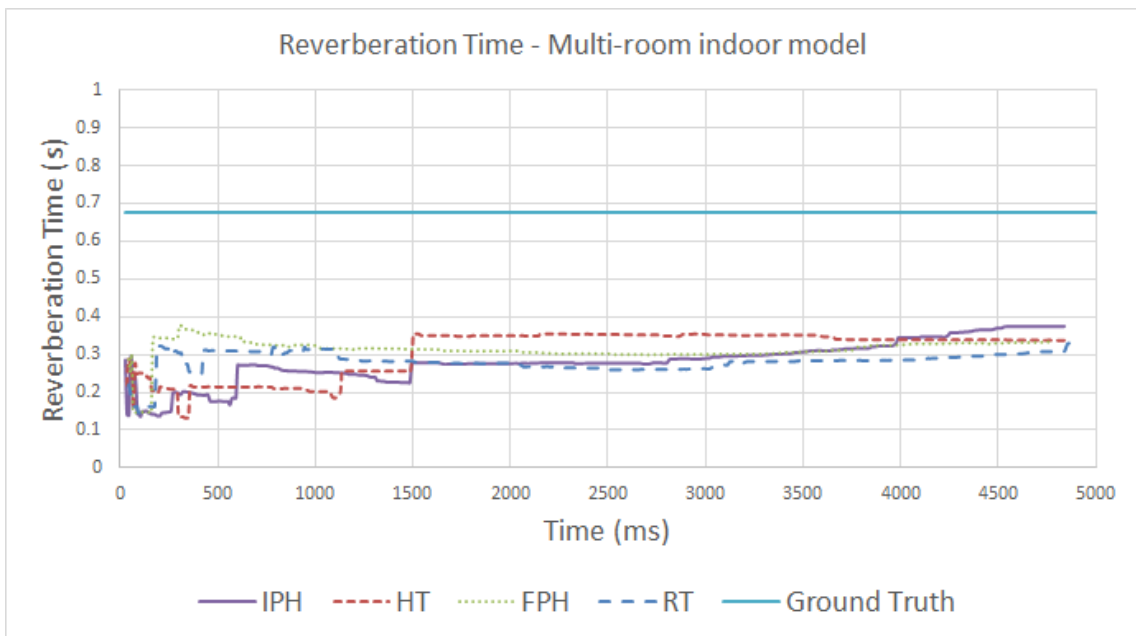
Figure 78. Reverberation time for Multi-room indoor model.
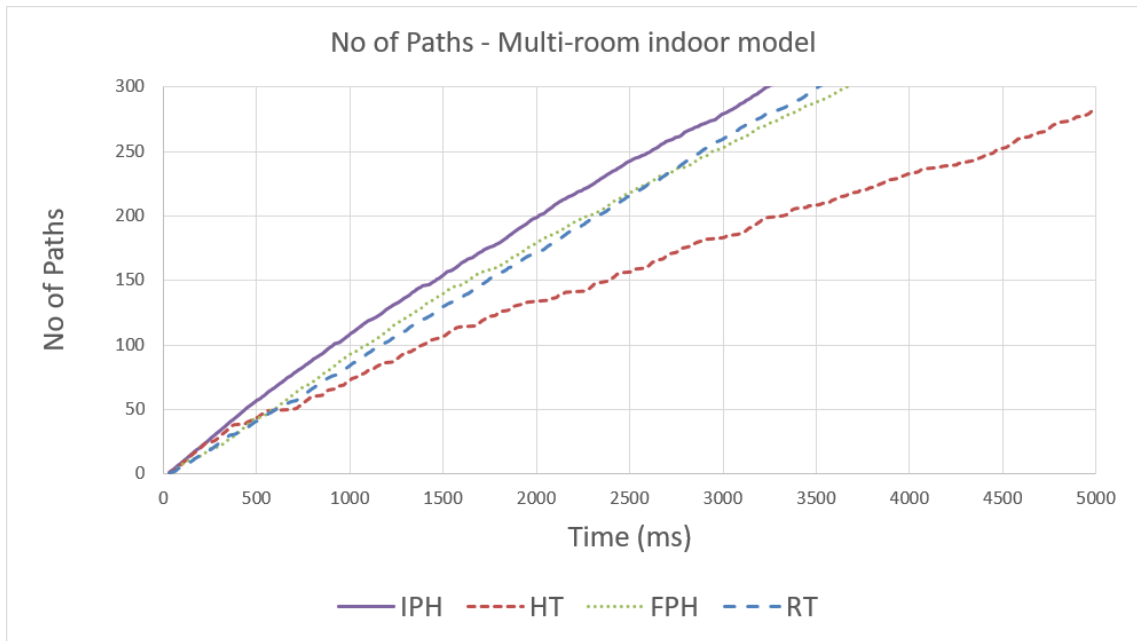
Figure 79. Paths for Multi-room indoor model.

4.2.4.3   Elmia Theatre

The results for executions run for the Elmia Theater displayed in Figure 80, Figure 81 and Figure 82.
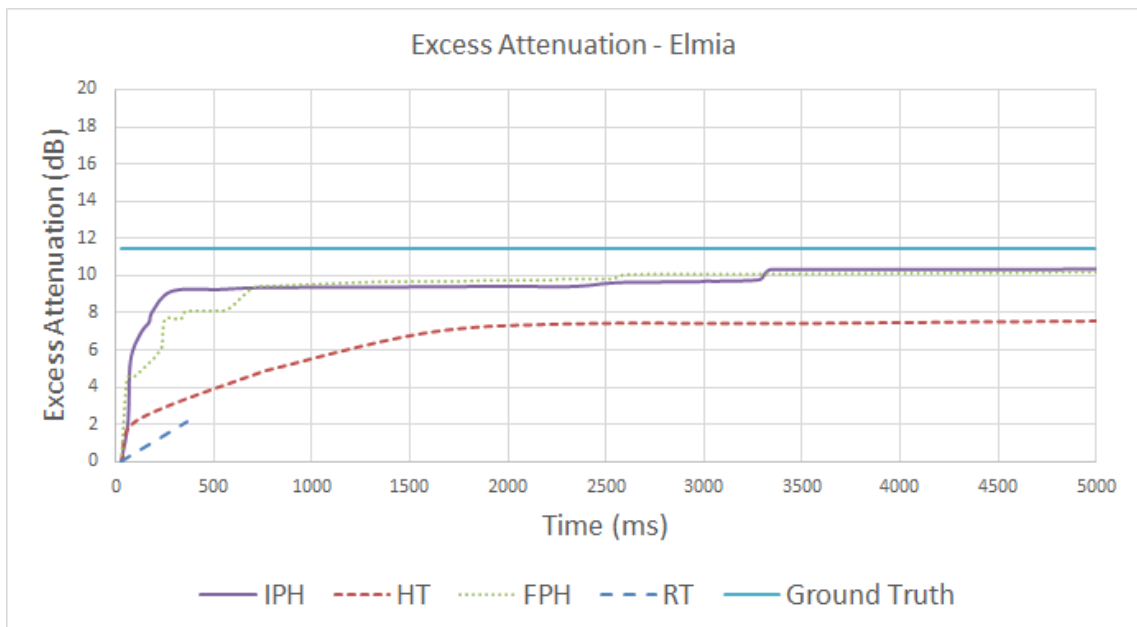
Figure 80. Excess attenuation for Elmia Theater.
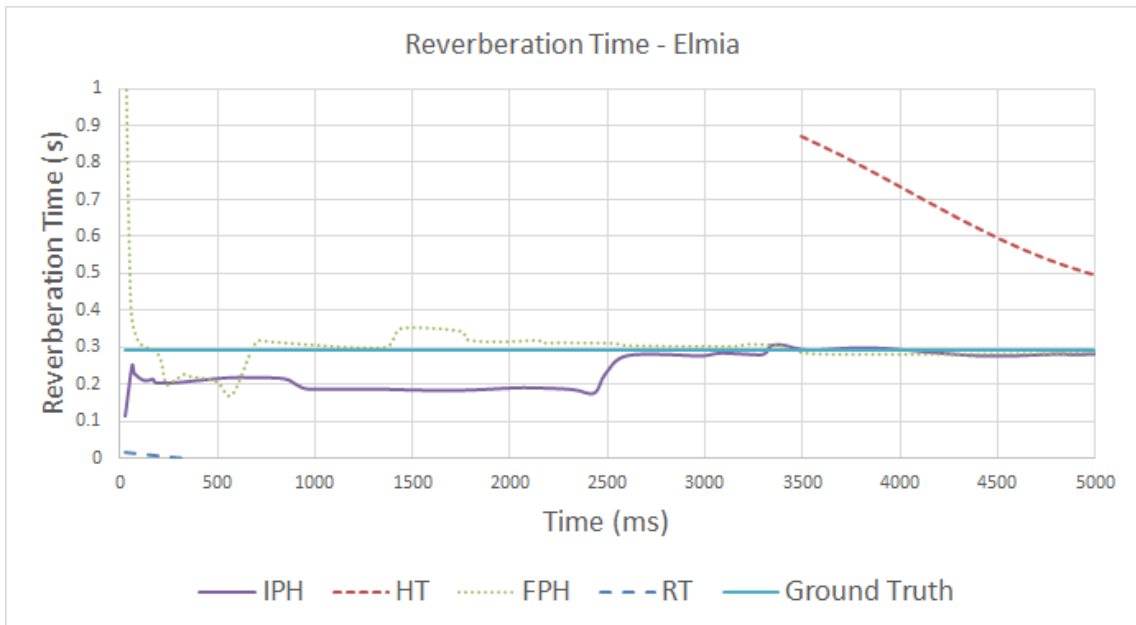
Figure 81. Reverberation time for Elmia Theater.
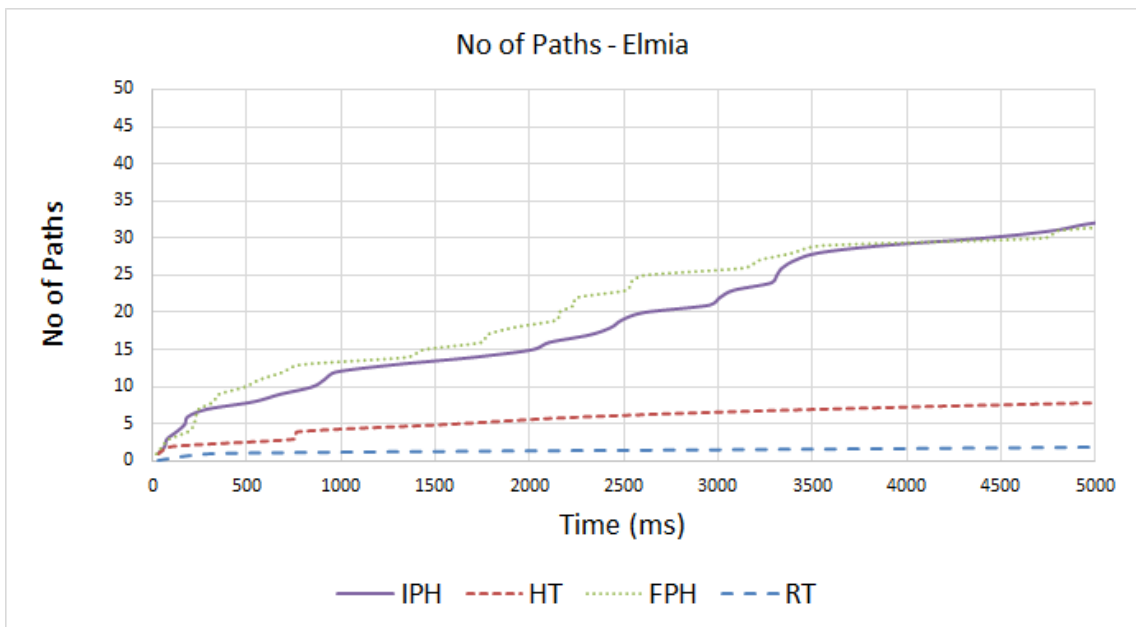
Figure 82. Paths for Elmia Theater**.**

Due to the fact that Elmia Theater is a large model and large parts of its walls are composed of protrusions, few specular reflections exist when compared to scattered sound paths. Thus, the number of paths detected for all executions is small, a fact that does not allow safe conclusions. Nevertheless, we can see that FPH and IPH detect a much larger number of sound paths than the other two and this allows both algorithms to approach faster the ground truth solutions for excess attenuation and reverberation

149

time. In Figure 82, we can see that FPH outperforms IPH in the number of paths at the initial stages of the calculation. Both algorithms perform equally well in excess attenuation. In reverberation time FPH outperforms IPH. Nevertheless, due to the small number of paths, the superiority might not be constant in subsequent executions. Ray tracing yielded to a few paths for a calculation of meaningful reverberation time and it is omitted from the reverberation time graph.

4.2.4.4 Outdoor Model

Graphs in Figure 83Figure 84 and Figure 85 contain the results for the outdoor model. In this case, despite the fact that the hybrid algorithm detects a much higher number of sound paths than the rest, in the case of excess attenuation, IPH performs equally well. FPH and ray tracing under-perform in both the reverberation time and the number of paths.
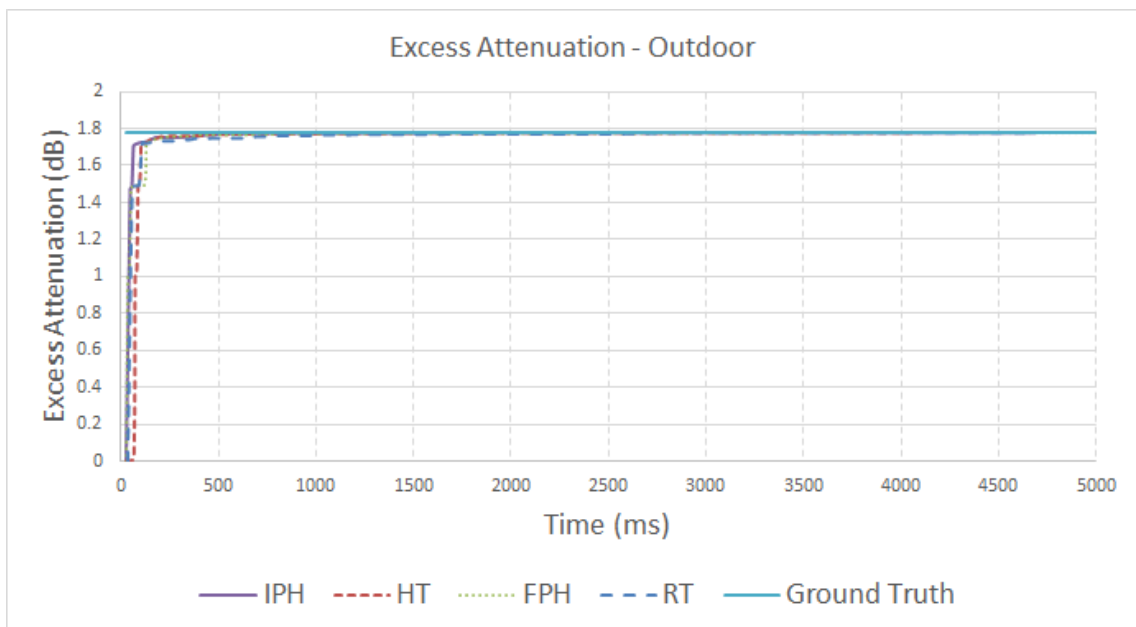
Figure 83. Excess attenuation for Outdoor model.
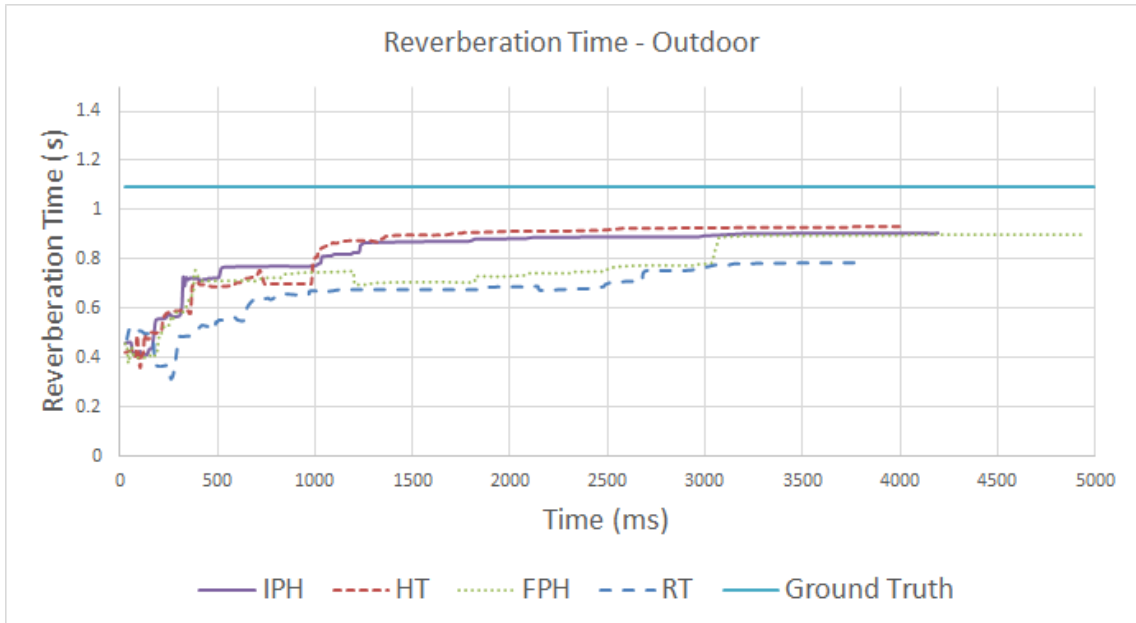
Figure 84. Reverberation time for Outdoor model.
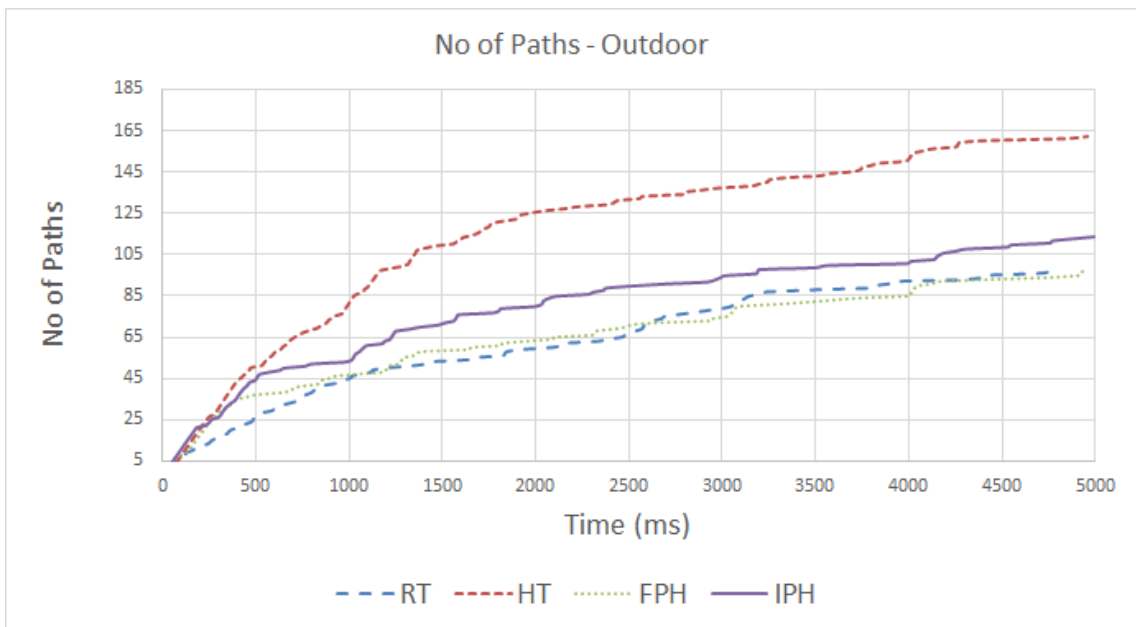
Figure 85. Paths for Outdoor model.

4.2.5 Conclusions and future work

In this section, we presented a method for improving the performance of geometrical acoustics algorithms used in sound rendering, based on the concept of prioritization. We modified a widely used hybrid tracing algorithm and we prioritized the traversal of the tree in such a way that more important nodes were validated earlier in the process. We

151

achieved this by automatically adjusting tracing termination criteria during runtime instead of explicitly setting them beforehand. Simulation results of our method on four models with different characteristics showed improvements in the calculated sound pressure and reverberation, which were of perceptual significance for all the cases.

Beyond performance improvements, our method also has the following benefits a) it removes the burden of setting termination criteria from the user. It is shown that the selection of termination criteria could affect the performance of tracing methods. Therefore, non-optimum termination criteria could lead to performance deterioration. b) It does not replace previous methods, but it can be used side by side. It can be used in parallel with any other GA method that consists a tree traversal. For example, it can enhance and improve any beam, ray or frustum tracing method.

Future work will focus on extending our algorithm beyond specular reflections to incorporate sound diffractions. Furthermore, we will examine further attributes of the 3D model that might lead to better and more efficient prioritization. Lastly, we will perform perceptual evaluations with users.

4.3 Applications of Prioritization in Engineering Applications

The third part of our work involved developing a novel algorithm for room acoustic parameters calculations, which address one of the major uncertainties in room acoustics prediction, that of user defined termination criteria (Charalampous & Economou, 2016). One of the uncertainties in room acoustics predictions that take place using geometrical acoustics methods is the user defined termination criteria. Ray tracing algorithms require a maximum length and a number of rays to be sent. Image source algorithms require maximum reflection orders and/or maximum sound attenuation. The presented algorithm adjusts progressively its termination criteria until a correct result is approximated, based on intelligent guessing, therefore removing this burden and risk from the user. The results approximate measurements equally well or better than other ray tracing algorithms, having the benefit that the user does not need to worry anymore about these settings.

4.3.1 The Algorithm

This algorithm is a hybrid implementation combining ray tracing and image source (Vorländer, 1989), extended with sound diffractions from images together with automating evaluation of termination criteria at run time. It can be split into two major parts a) tracing b) result evaluation and criteria readjustment. The algorithm is explained graphically in the flowchart in Figure 86. In brief, the process can be summarized as follows

a) 100 rays are sent.
b) The specular reflections and the image source edge diffractions detected are evaluated and added to the 1/3 octave reflectograms.
c) Termination criteria are adjusted if needed.
d) Result deviation is evaluated, and the loop goes back to (a) or terminates accordingly.
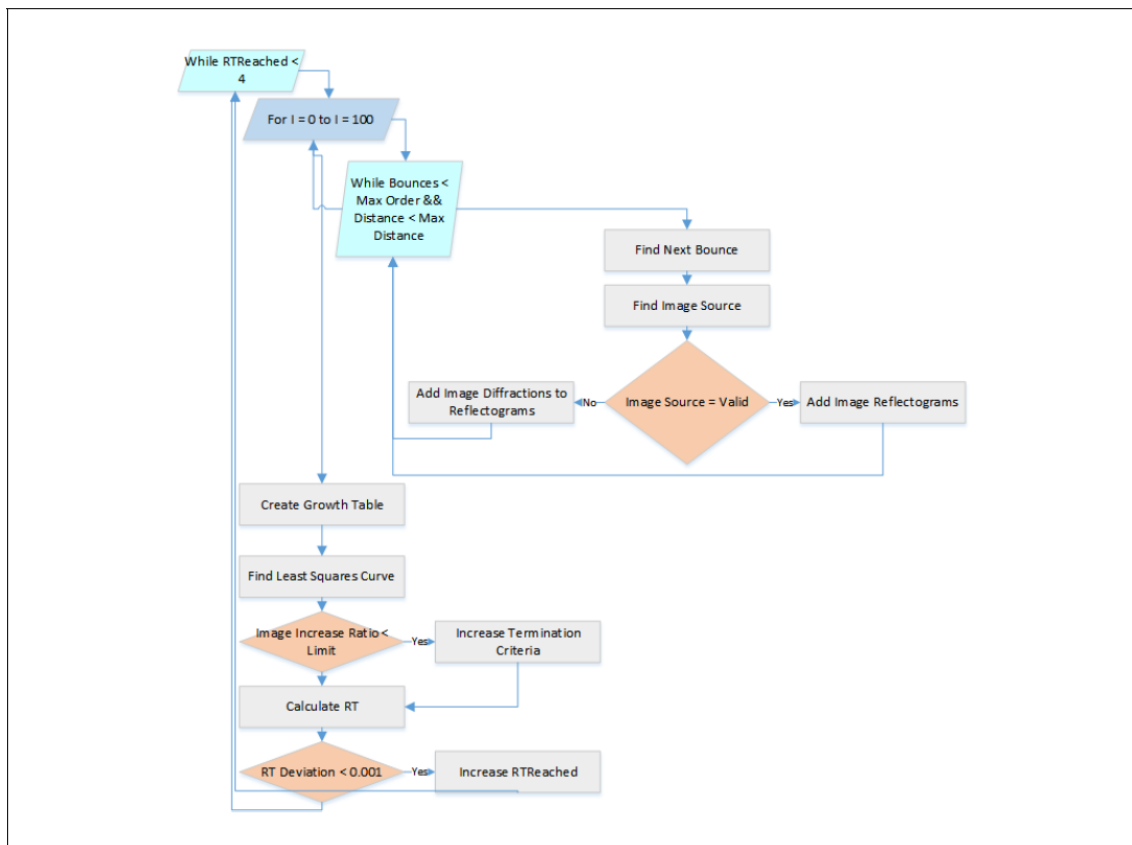
Figure 86. Flowchart for user independent room acoustics parameters calculation.

4.3.1.1 *Tracing*

As mentioned above the tracing part of our algorithm, based on Vorländer, extends by also detecting sound diffractions from image sources. The addition of edge sound diffractions from images allows for a more accurate and physically correct simulation of the scattering phenomenon in interior spaces.

The image source detection process goes as follows:

a) A ray is cast from the source and propagated through space.

b) As soon as the ray hits a surface, the surface's image source is generated and recorded.

c) The ray is reflected from the surface.

d) Steps b and c are repeated recursively until the termination criteria are met. The termination criteria are the number of ray bounces and the distance traveled by the ray and they are adjusted during run time (this is discussed later on).

e) On meeting the termination criteria, the ray is neglected, and the image sources recorded during ray tracing are evaluated for their validity. Valid image sources are used for the estimation of the impulse response.

In the above process an extra step is added, that of the detection of image source edge diffractions from the image's surface. The addition of sound diffractions was considered necessary, in order to provide a more accurate and physically correct representation of the diffused sound. Typical GA implementations consider diffused reflections which reflect at different angles than the angle of incidence, an assumption that could provide a statistically correct result in many cases, but it does not represent the actual way sound waves propagate. Hence, we chose to use sound diffractions instead of diffused reflections. The image source edge diffractions are only detected whenever the receiver does not fall in the field angle of the image source. Thus, an image source can contribute to the sound field either with a specular reflection or a diffraction from its surface edges. A graphical explanation is given in Figure 87.
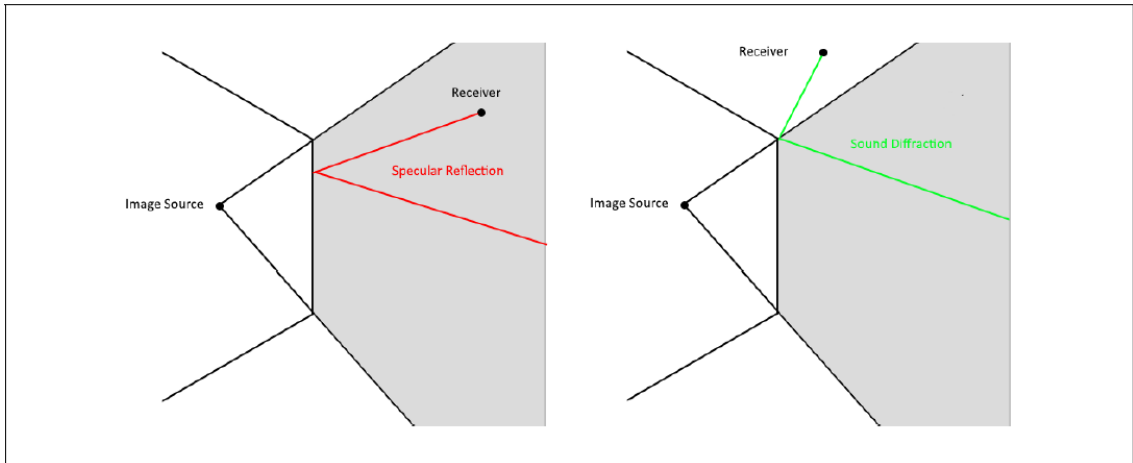
Figure 87. Image Source Edge Diffractions. Detection of a specular reflection (left) and an edge diffraction in the case of no specular reflection(right)

The image source edge diffractions are constructed by finding the shortest path connecting a source, an edge and the receiver. The process is explained in detail in the Diffraction Path Detection section. Because for each surface there might be more than one valid diffraction path, for each image source we consider only the shortest diffraction path to the receiver.
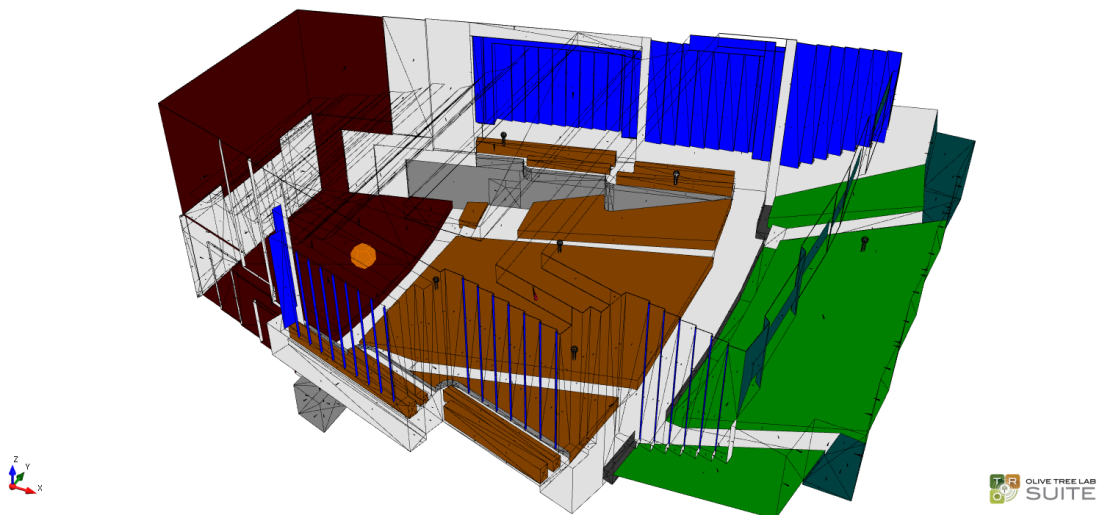
Figure 88. Elmia Hall Model

4.3.1.2 Evaluation Criteria and Readjustment

The differentiation of the algorithm, when compared to traditional geometrical acoustics algorithms, is the introduction of an evaluation stage during run-time and the dynamic adjustment of termination criteria. As seen in Figure 86, for every 100 rays traced, an evaluation part takes place. This part evaluates the following a) The ratio of increase of valid rays and b) The mean absolute deviation between the last 6 calculated reverberation times. If (a) falls under a certain number, this indicates that the tracing has started getting saturated and the termination criteria are increased. The termination criterion increase takes place when the following inequality becomes true

$$Ri < 3Am/Rr$$

Equation 57

Where Ri is the ratio of increase between the total valid images detected up to that moment to the number of valid images at the previous evaluation, A is the ratio of images growth over the impulse response time, m is the mean free path and Rr is the ratio of increase of rays traced.

The total transfer function of the sound field is calculated as per the method described extensively in Chapter 2. The transfer functions of the paths are used for the construction of the reflectograms, which are subsequently used for the calculation of the room acoustics parameters. Following on, the reverberation time for a single frequency is stored in a list. The frequency is selected after calculating the Sabine reverberation time and picking the frequency with the highest RT. We call this "the check frequency" and it is calculated as follows

$$agrmaxf(Sabine(i))$$

Where i is the check frequency.

At each calculation interval, the reverberation time is calculated using the process described in ISO 3382-2 (ISO, 2008)

As soon as the list count reaches 6 reverberation time calculations, then the mean absolute deviation of these calculations is calculated. As soon as the deviation falls under 0.001 then a variable named RTReached is increased. If the deviation does not fall under 0.001 then the RTReached variable is set to 0. The calculation is terminated

when the RTReached variable reaches the value of 4, meaning that for 4 consecutive times the deviation was under 0.001. This fact indicates that the subsequent additions of image sources have not changed the result, thus the actual reverberation time has been approximated. At this stage, the tracing is terminated, and the final results are calculated.

4.3.1.3   Results

We compare our algorithm to an equivalent user-dependent (UD) algorithm. The UD algorithm is the same as the user-independent (UI) version with the difference that the ray distance and the number of bounces is set by the user. We run the UI algorithm by using the ELMIA hall model (Figure 88) that was used in round robin 2 (Bork I. , 2000) with the same input data, to allow a comparison with measurements. UI algorithm was terminated automatically after 10732 rays were traced and termination critetion increases to 96 bounces. Then, we run the UD version with four different input configurations. We chose the Elmia hall because the model is widely available as well as some material absorption coefficients. However, the original web page has been taken down, so we had the data provided by third-party software vendors. We have also noticed some deviations between the results provided by the software vendors and the round robin findings (the software calculations deviated significantly from the reported calculation in the round robin), therefore we adjusted the model's absorption coefficients until the calculation results of the third-party software match the round robin results. Nevertheless, some deviations that remain in the calculation results might be explained by the uncertainty in the input data. We compare the results of each run for T30, D50 and Centre Time for Source 1 and Receiver 6, as described by Bork (Bork I. , 2000). We show the results in Figure 89,Figure 90 and Figure 91 respectively.
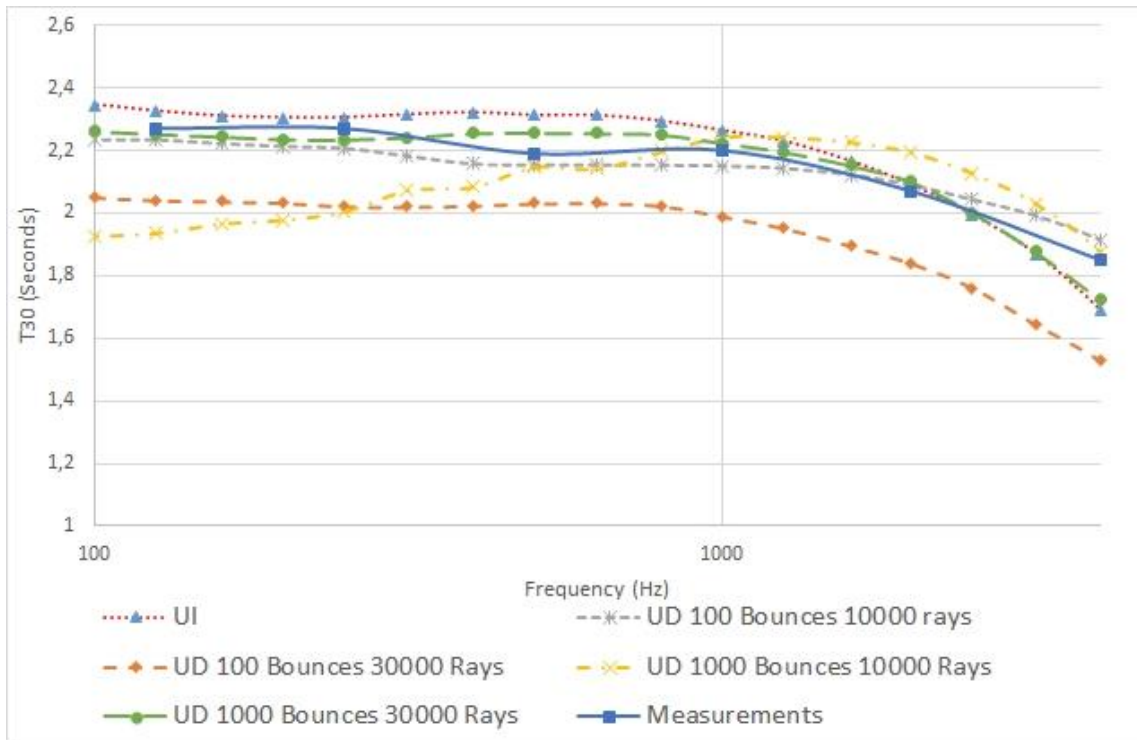
Figure 89. T30 Comparisons
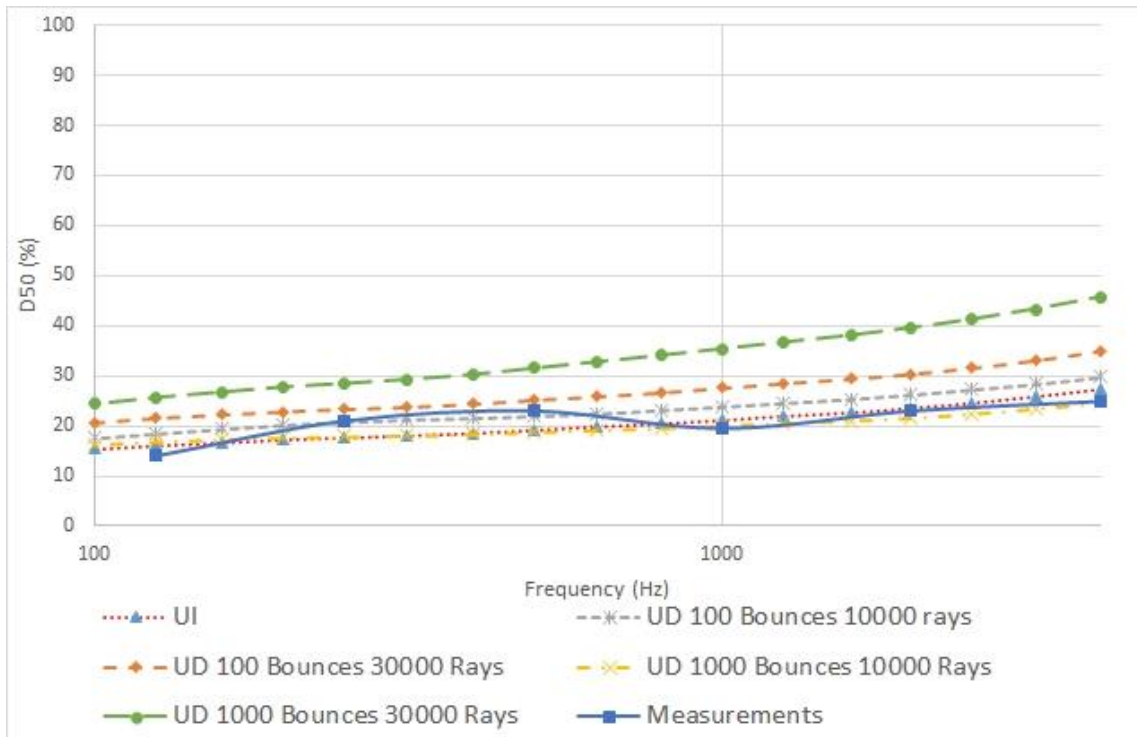
Figure 90. D50 Comparisons
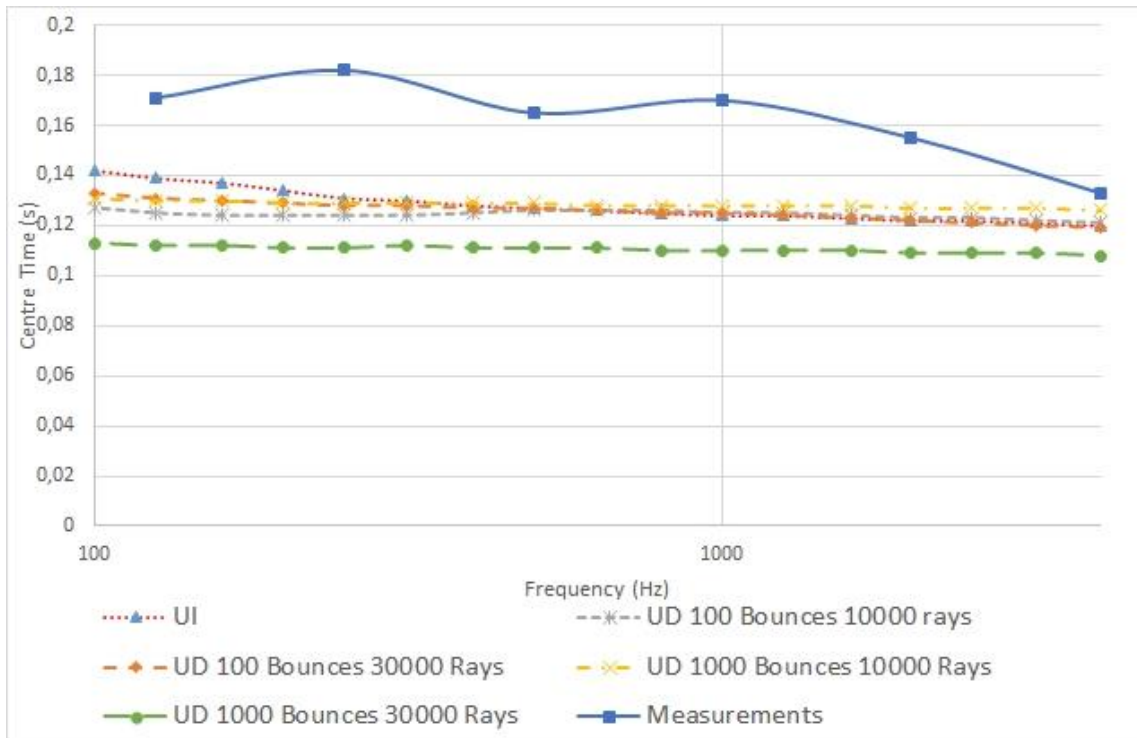
Figure 91. CT Comparisons

By examining the results, we see the deviation in the calculated results between the two algorithms. We notice that the deviation occurs not only by the selected number of rays, something that could be intuitively expected, but also by the selected termination order, which is relatively high in both cases of the UD algorithm. On the other hand, we remark how closely the UI approximates the results, which are driven by its internal termination adjustment procedure and the incremental validation of the results.

5 Conclusions and Future Work

5.1 Conclusions

The purpose of this thesis was to present a wave-based geometrical acoustics model that could yield accurate calculations of sound propagation in arbitrary 3D geometries and acceptable calculation time for practical purposes. The model incorporates the calculation of sound reflections, sound diffractions and atmospheric effects for arbitrary 3D geometries and is successfully incorporated in a commercial software application. The accuracy of the model is validated through several projects that involved comparing predicted and measured results. We focused on cases that highlight the wave-based nature of sound-like wave interferences and sound diffractions. The results indicate that

our method provides a better match than existing widely adopted models, especially when wave based phenomena need to be considered, like wave interferences. The applicability of our model on several different scenarios assisted in unifying domains of acoustics engineering that have been treated separately up to now, like room acoustics, environmental acoustics and noise control. Our calculation method can successfully calculate a range of acoustical parameters like reverberation times for auditoria, speech transmission index for open-plan offices as well as the effectiveness of noise barriers in highways.

In addition to the above, we presented novel algorithms for improving the tracing process of the image algorithm used by our model. Our research has shown that the type of tree traversal chosen by a geometrical acoustics tracing algorithm could affect the performance in a given time span. Therefore, we have proposed tracing algorithms that alter the sequence, in which the tree nodes are examined in an intelligent way by using priority functions. We have shown that, by applying intelligent prioritization during the traversal process, an algorithm could demonstrate improvements of perceptual importance. Also, we have shown that, by using intelligent prioritization, we could develop tracing algorithms that are independent of user defined tracing parameters which might be a source of uncertainty in the calculated result. Our user-independent tracing algorithm has also been incorporated in OTL Suite as a part of the room acoustic calculations offered by the software application.

5.2 Future Work

We plan to extend the current work in several ways. Some of the immediate areas of the extension are the following

1. **Sound Transmission.** 3D sound transmission through solid structures, is a subject matter that is completely absent from the literature regarding 3D sound propagation techniques. There is substantial research available for sound transmission in solid materials but as far as the authors are aware, such calculations have not been included in 3D sound propagation tools. To add such calculations, a model like ours needs to be extended in order to detect sound paths refracting and passing through walls and other solid materials. Then, for these transmitting paths, we need to calculate the sound reduction index for each

transmission point and add these paths to the results. This addition will allow our model to be used in another major domain of acoustics called Building Acoustics.

2. **Advanced Material Properties.** At the moment, our reflection calculations assume locally reacting flat surfaces. We plan to extend these calculations to account for extended reacting materials as well as rough surfaces. The calculation of reflection coefficients for extended reacting materials involves more complicated equations and rough surfaces calculation will allow for a more accurate calculation of sound scattering caused by non-planar surfaces.

3. **Prioritization on Sound Diffraction Detection.** We plan to extend our prioritization technique to consider sound diffractions as well. This will entail the development of priority functions specific to sound diffraction path properties. We assume that due to the different nature of diffracted sound waves, prioritization will benefit by priority functions designed specifically for sound diffractions.

4. **Game Engine Sound Rendering.** Our model has been developed for use by a non-real-time calculation engine aimed mainly at acoustics engineers. However, our findings apply to existing sound rendering engines, currently used for spatial audio auralization. We plan to incorporate our calculation and prioritization techniques in such engines and investigate the improvements in the accuracy and performance of the calculated results. Our main target is to use existing sound rendering libraries, like EVERTims (EVERTims, 2020), and modify them accordingly, to incorporate prioritization techniques presented in this thesis. Then we plan to compare the quality of sound rendering between prioritized and non-prioritized methods.

In brief, the long term target of our research plans is the unification of the scattered field of computational acoustics into a general wave-based geometrical acoustics model that could take into account as many acoustical phenomena as possible and be used in a diverse range of practical applications ranging from laboratory experimental setups to environmental acoustic, architectural acoustics, virtual reality and video games.

6 References

(2020). Ανάκτηση από EVERTims: http://evertims.github.io

Allard, J. F., & Atalla, N. (2009). *Propagation of Sound in Porous Media.* John Wiley & Sons, Ltd.

Allen, J. B., & Berkley, D. A. (1979). Image method for efficiently simulating small-room acoustics. *The Journal of the Acoustical Society of America, 65*, 943.

Allred, J. C., & Newhouse, A. (1958). Applications of the Monte Carlo method to architectural acoustics. *The Journal of the Acoustical Society of America, 30*, 1-3.

Ando, Y., Takaishi, M., & Tada, K. (1982). Calculations of the sound transmission over theatre seats and meth-ods for its improvement in the low-frequency range. *Journal of the Acoustical Society of America*, 443-448.

Antani, L., Chandak, A., Savioja, L., & Manocha, D. (2012). Interactive sound propagation using compact acoustic transfer operators. *ACM Transactions on Graphics (TOG), 31*, 7.

Antani, L., Chandak, A., Taylor, M., & Manocha, D. (2012). Direct-to-indirect acoustic radiance transfer. *Visualization and Computer Graphics, IEEE Transactions on, 18*, 261-269.

Antani, L., Chandak, A., Taylor, M., & Manocha, D. (2012). Efficient finite-edge diffraction using conservative from-region visibility. *Applied Acoustics, 73*, 218-233.

Antonacci, F., Foco, M., Sarti, A., & Tubaro, S. (2004). Fast modeling of acoustic reflections and diffraction in complex environments using visibility diagrams. *Proceedings of 12th european signal processing conference (EUSIPCO'04)*, (σσ. 1773-1776).

Aretz, M. (2012). *Combined Wave and Ray Based Room Acoustic Simulations of Small Rooms* (Τόμ. 12). Logos Verlag Berlin.

Aretz, M., Dietrich,, P., & Vorländer, M. (2014). Application of the Mirror Source Method for Low Frequency Sound Prediction in Rectangular Rooms. *Acta Aoustica United With Acustica*, 306-319.

Artusi, A., Michael, D., Roch, B., Chrysanthou, Y., & Chalmers, A. (2011). A selective approach for tone mapping high dynamic range content. *SIGGRAPH Asia 2011 Posters*, (σ. 50).

Atalla, N., & Sgard, F. (2005). On the modeling of perforated plates and screens. *12th ICSV*. Lisbon.

Atalla, N., & Sgard, F. (2007). Modeling of perforated plates and screens using rigid frame porous models. *Journal of Sound and Vibration*, 195-208.

Attenborough , H., & Waters-Fuller, T. (2000). Effective impedance of rough porous ground surfaces. *The Journal of the Acoustical Society of America*.

Attenborough, K. (1992). Ground parameter information for propagation modeling. *The Journal of the Acoustical Society of America*, 418-427.

Attenborough, K., Li, K. M., & Horoshenkov, K. (2007). *Predicting Outdoor Sound.* Taylor & Francis.

Attenborough, K., Taherzadeh, S., Bass, H. E., Di, X., Raspet, R., Becker, G. R., . . . Hoof, H. A. (1995). Benchmark Cases for outdoor sound propagation models. *Journal of the Acoustical Society of America, 97*(1), 173-191.

Barbone, P. E., Montgomery, J. M., Michael, O., & Harari, I. (1998). Scattering by a hybrid asymptotic/finite element method. *Computer methods in applied mechanics and engineering, 164*, 141-156.

Bashir, I., Attenborough, K., Taherzadeh, S., & Hill, T. (2010). Diffraction assisted rough ground effect. *Proceedings of ASA 160th Meeting*.

Beig, M., Kapralos, B., Collins, K., & Mirza-Babaei, P. (2019). GPU-Based Voxel Graph Pathfinding for Spatial Audio Rendering in Games and VR. *IEEE Conference on Games* (σσ. 1-8). IEEE.

Berardi , U., & Iannace, G. (2016). Predicting the sound absorption of natural materials: Best-fit inverse laws for the acoustic impedance and the propagation constant. *Applied Acoustics*, 131-138.

Berardi, U., & Iannace, G. (2015). Acoustic characterization of natural fibers for sound absorption applications. *Building and Environment*.

Berry, A., & Daigle, G. A. (1988). Controlled experiments of the diffraction of sound by a curved surfacce. *Journal of the Acoustical Society of America*, 2047-2058.

Bertram, M., Deines, E., Mohring, J., Jegorovs, J., & Hagen, H. (2005). Phonon tracing for auralization and visualization of sound. *Visualization, 2005. VIS 05. IEEE*, (σσ. 151-158).

Bigot, A., Economou, P., & Economou, C. (2017). Wind turbine noise prediction using Olive Tree Lab Terrain. *7th International Conference on Wind Turbine Noise*. Rotterdam.

Biot, M. A. (1968). Generalised boundary condition for multiple scatter in acoustic reflection. *Journal of the Acoustical Society of America*, 1616-1622.

Biot, M. A., & Tolstoy, I. (1957). Formulation of wave propagation in infinite media by normal coordinates with an application to diffraction. *Journal of the Acoustical Society of America*, 381-391.

Bolt, R. H. (1939). Normal Modes on Vibration in Room Acoustics. *Journal of the Acoustical Society of America*, 184-197.

Borish, J. (1984). Extension of the image model to arbitrary polyhedra. *The Journal of the Acoustical Society of America, 75*, 1827.

Bork, I. (2000). A comparison of room acoustics simulation software - the 2nd round robin on room acoustical computer simulation. *Acta Acustica inited with Acoustica*, 943-956.

Bork, I. (2000). A comparison of room simulation software-The 2nd round robin on room acoustical computer simulation. *Acta Acustica united with Acustica, 86*, 943-956.

Bowman, J., & Senior, T. (1969). The Wedge. *Electromagnetic and Acoustic Scattering by Simple*.

Bradley, J. S. (1991). Some further investigations of the seat dip effect. *Journal of the Acoustical Society of America*, 324-333.

Bradley, J. S. (1991). Some further investigations of the seat dip effect. *Journal of the Acoustical Society of America*, 324-333.

CadnaA – state-of-the-art noise prediction software. (2020, October 01). Ανάκτηση από Datakustik: https://www.datakustik.com/products/cadnaa/cadnaa/

Calamia, P. T. (2009). *Advanced in Edge Diffraction Modelling for Virtual Acoustics Simulations.* Princeton University.

Cao, C., Ren, Z., Schissler, C., Manocha, D., & Zhou, K. (2016). Interactive Sound Propagation with Bidirectional Path Tracing. *ACM Transactions on Graphics*, 1-11.

Chandak, A. (2011). *Efficient Geometric Sound Propagation Using Visibility Culling.* Ph.D. dissertation, University of North Carolina.

Chandak, A., Antani, L., Taylor, M., & Manocha, D. (2009). FastV: From-point Visibility Culling on Complex Models. *Computer Graphics Forum*, *28*, σσ. 1237-1246.

Chandak, A., Antani, L., Taylor, M., & Manocha, D. (2011). Fast and accurate geometric sound propagation using visibility computations. *Building Acoustics, 18*, 123-144.

Chandak, A., Lauterbach, C., Taylor, M., Ren, Z., & Manocha, D. (2008). Ad-frustum: Adaptive frustum tracing for interactive sound propagation. *Visualization and Computer Graphics, IEEE Transactions on, 14*, 1707-1722.

Charalampous, P., & Economou, P. (2013). A Framework for the Development of Accurate Acoustic Calculations for Games. *Audio Engineering Society Conference: 49th International Conference: Audio for Games.*

Charalampous, P., & Economou, P. (2016). An Improved user-independed algorithm for room acoustic parameters calculation. *23rd International Congress on Sound and Vibration.*

Charalampous, P., & Michael, D. (2014). Sound propagation in 3D spaces using computer graphics techniques. *Virtual Systems & Multimedia (VSMM), 2014 International Conference on*, (σσ. 43-49).

Charalampous, P., & Michael, D. (2014). Tree Traversal Algorithms for Real Time Sound Propagation Calculation. *Audio Engineering Society Conference: 55th International Conference: Spatial Audio.*

Charalampous, P., & Michael, D. (2016). Improved Hybrid Algorithm for Real Time Sound Propagation using Intelligent Prioritization. *MELECON 2016.*

Charalampous, P., & Michael-Grigoriou, D. (2018). Geometrical Algorithms for Real Time Sound Rendering Using Intelligent Prioritization. *ICAT-EGVE.* Limassol.

Clay, C. S., Chu, D., & Li, S. (1993). Specular reflections of transient pressures from finite width plane facets. *Acoustical Society of America*, 2279-2286.

Clifford, S. F., & Lataitis, R. J. (1983). Turbulence effects on acoustc wave propagation over a smooth surface. *Journal of the Acoustical Society of America*, 1545-1550.

Cohen-Or, D., Chrysanthou, Y. L., Silva, C. T., & Durand, F. (2003). A survey of visibility for walkthrough applications. *Visualization and Computer Graphics, IEEE Transactions on, 9*, 412-431.

Collins, K. (2008). *Game sound: an introduction to the history, theory, and practice of video game music and sound design.* The MIT Press.

Cowan, B., & Kapralos, B. (2010). GPU-based real-time acoustical occlusion modeling. *Virtual reality, 14*, 183-196.

Danish Electronics Light & Acoustics. (2006). *Validation of the Propagation Model for The Danish Road Directorate.* Danish Electronics Light & Acoustics.

Davies, W. J., & Cox, T. J. (2000). Reducing seat dip attenuation. *Journal of the Acoustical Society of America*, 2211-2218.

Delany, M. E., & Bazley, E. N. (1970). Acoustical properties of fibrous absorbent materials. *Applied Acoustics*, 105-116.

Drechsler, S. (2014). An algorithm for automatic geometry simplification for room acoustical simulation based on regression planes. *Acta Acustica united with Acustica, 100*, 956-963.

Dreher, M., Dutilleux, G., Junker, F., & others. (2012). Optimized 3D ray tracing algorithm for environmental acoustic studies. *Acoustics 2012 Nantes*.

Economou , P., & Charalampous, P. (2016). Room Resonances using Wave Based Geometrical Acoustics (WBGA). *23rd International Congress on Sound & Vibration.* Athens.

Economou, P., & Charalampous, P. (2012). A comparison of ISO 9613 and advanced calculation methods using Olive Tree Lab-Terrain, an outdoor sound propagation software application: Predictions versus experimental results. *Meeting on" Environmental Noise Propagation-Definitions, measuring and control aspects.*

Economou, P., & Charalampous, P. (2013). The Significance of Sound Diffraction Effects in Simulating Acoustics in Ancient Theatres. *Acta Acustica united with Acustica, 99*, 48-57.

Economou, P., & Charalampous, P. (2016). Seat Dip Effect using Wave Based Geometrical Acoustics (WBGA). *23rd International Congress on Sound & Vibration.* Athens.

Economou, P., & Peppin, R. J. (2012). A comparison of ISO 9613-2 and advanced calculation methods: Predictions versus experimental results. *Canadian Acoustics, 40*, 54-55.

Economou, P., Charalampous, P., & Amadasi, G. (χ.χ.). Development of Accurate and Fast Acoustic Calculations using Olive Tree Lab-Acoustics Lib.

Economou, P., Charalampous, P., Ioannides, S., & Polykarpou, P. (χ.χ.). THE SIGNIFICANCE OF SOUND DIFFRACTION EFFECTS IN PREDICTING ACOUSTICS IN ANCIENT THEATRES.

Embleton, T. F., Thiessen, G. j., & Piercy, J. E. (1976). Propagation in an inversion and reftections at the ground. *Journal of the Acoustincal Society of America*, 278-82.

Embleton, T. W. (1980). Line integral theory of barrier attenuation in the presence of ground. *Journal of the Acoustical Society of America*, 42-45.

Environmental Noise Modeling and Mapping Software – Predictor-LimA. (2020, October 01). Ανάκτηση από EnviroSuite: https://envirosuite.com/predictor-lima

Eyring, C. F. (1930). Reverberation time in "dead" rooms. *The Journal of the Acoustical Society of America, 1*, 217-241.

Farina, A. (1995). RAMSETE-a new Pyramid Tracer for medium and large scale acoustic problems. *Proc. of Euro-Noise*, *95*.

Foale, C., & Vamplew, P. (2007). Portal-based sound propagation for first-person computer games. *Proceedings of the 4th Australasian conference on Interactive entertainment*, (σ. 9).

Funkhouser, T., Min, P., & Carlbom, I. (1999). Real-time acoustic modeling for distributed virtual environments. *Proceedings of the 26th annual conference on Computer graphics and interactive techniques*, (σσ. 365-374).

Funkhouser, T., Tsingos, N., & Jot, J.-M. (2003). Survey of methods for modeling sound propagation in interactive virtual environment systems.

Funkhouser, T., Tsingos, N., Carlbom, I., Elko, G., Sondhi, M., West, J. E., . . . Ngan, A. (2004). A beam tracing method for interactive architectural acoustics. *The Journal of the Acoustical Society of America, 115*, 739.

Hadden, J. W., & Pierce , A. D. (1981). Sound diffraction around screens and wedges for arbitrary point source locations. *Journal of the Acoustical Society of America*, 1266-1276.

Hamidi, F., & Kapralos, B. (2009). A review of spatial sound for virtual environments and games with graphics processing units. *Open Virtual Real J, 1*, 8-17.

Hampel, S., Langer, S., & Cisilino, A. P. (2008). Coupling boundary elements to a raytracing procedure. *International journal for numerical methods in engineering, 73*, 427-445.

Havel, J., & Herout, A. (2010). Yet Faster Ray-Triangle Intersection. *IEEE TRANSACTIONS ON VISUALIZATION AND COMPUTER GRAPHICS*, 434-438.

He, Z. C., Cheng, A. G., Zhang, G. Y., Zhong, Z. H., & Liu, G. R. (2011). Dispersion error reduction for acoustic problems using the edge-based smoothed finite element method (ES-FEM). *International Journal for Numerical Methods in Engineering, 86*, 1322-1338.

Heuvhek, F., Caviedes-Nozal, D., Fernandez-Grande, E., Brunskog, J., & Agerkvist, F. T. (2019). Adapting transfer functions to changes in atmospheric conditions for outdoor sound field control. *23rd International Congress on Acoustics.* Aachen.

Hodgson, M., & Nosal, E.-M. (2006). Experimental evaluation of radiosity for room sound-field prediction. *The Journal of the Acoustical Society of America, 120*, 808.

Huiberts, S. (2010). *Captivating sound the role of audio for immersion in computer games.* Ph.D. dissertation, University of Portsmouth.

Hulusic, V., Harvey, C., Debattista, K., Tsingos, N., Walker, S., Howard, D., & Chalmers, A. (2012). Acoustic Rendering and Auditory--Visual Cross-Modal Perception and Interaction. *Computer Graphics Forum*, *31*, σσ. 102-131.

Hulusic, V., Harvey, C., Debattista, K., Tsingos, N., Walker, S., Howard, D., & Chalmers, A. (2012). Acoustic Rendering and Auditory--Visual Cross-Modal Perception and Interaction. *Computer Graphics Forum*, *31*, σσ. 102-131.

International Standards Organization. (1996). *Acoustics - Attenuation of sound during propagation.* International Standards Organization.

Ishida, K. (1995). Investigation of the fundamental mechanism of the seat-dip effect – Using measurements on a parallel barrier scale-model. *Journal of the Acoustical Society of Japan*, 105-114.

ISO. (2008). ISO 3382-2:2008,Acoustics -- Measurement of room acoustic parameters -- Part 2: Reverberation time in ordinary rooms. ISO.

Jedrzejewski, M., & Marasek, K. (2006). Computation of room acoustics using programmable video hardware. Στο *Computer Vision and Graphics* (σσ. 587-592). Springer.

Jensen, H. W. (1996). Global illumination using photon maps. Στο *Rendering Techniques' 96* (σσ. 21-30). Springer.

Jeong, C.-H., Jeong, G., & Rindel, J. (2008). An approximate treatment of reflection coefficient in the phased beam tracing method for the simulation of enclosed sound fields at medium frequencies. *Applied Acoustics*, 601-613.

Kapralos, B. (2006). *The sonel mapping acoustical modeling method.* Ph.D. dissertation, YORK UNIVERSITY TORONTO, ONTARIO.

Kapralos, B., Jenkin, M., & Milios, E. (2004). Sonel mapping: Acoustic modeling utilizing an acoustic version of photon mapping. *Haptic, Audio and Visual Environments and Their Applications, 2004. HAVE 2004. Proceedings. The 3rd IEEE International Workshop on*, (σσ. 1-6).

Keller, J. B. (1962). Geometrical Theory of Diffraction. *Journal of the Optical Society of America*, 116-130.

Kim, H. S., Kim, J. S., Kang, H. J., Kim, B. K., & Kim, S. R. (2005). Sound diffraction by multiple wedges and thin screens. *Applied Acoustics*, 1102-1119.

Kirkup, S., & Wu, S. F. (2000). The boundary element method in acoustics. *Journal of the Acoustical Society of America, 108*, 1973-1973.

Kleshchev, A. (2016). Some Methods of Solution of Problems of Sound Diffraction on Bodies of Non-Analytical Form. *Open Journal of Acoustics*.

Knuth, D. E. (1999). *The art of computer programming.* Fundamental Algorithms.

Koutsouris, G. I., Brunskog, J., Jeong, C.-H., & Jacobsen, F. (2013). Combination of acoustical radiosity and the image source method. *The Journal of the Acoustical Society of America, 133*, 3963-3974.

Kouyoumjian, R. G., & Pathak, P. H. (1974). A uniform geometrical theory of diffraction for an edge in a perfectly conducting surface. *Proc. IEEE*, 1448-1461.

Krokstad, A., Strom, S., & Sørsdal, S. (1968). Calculating the acoustical room response by the use of a ray tracing technique. *Journal of Sound and Vibration, 8*, 118-125.

Kulowski, A. (1985). Algorithmic representation of the ray tracing technique. *Applied Acoustics, 18*, 449-469.

Kuttruff, H. (2007). *Acoustics: an introduction.* Taylor & Francis.

Laine, S., Siltanen, S., Lokki, T., & Savioja, L. (2009). Accelerated beam tracing algorithm. *Applied Acoustics, 70*, 172-181.

Lam, Y. W. (2005). Issues for computer modelling of room acoustics in non-concert hall settings. *Acoust. Sci. & Tech*, 145-155.

Lam, Y. W. (2009). An analytical model for turbulence scattered rays in the shadow zone for outdoor sound propagation calculation. *Journal of the Acoustical Society of America, 125*(3), 1340-1350.

Lam, Y. W. (2009). An analytical model for turbulence scattered rays in the shadow zone for outdoor sound propagation calculation. *Journal of the Acoustical Society of America*, 1340-1350.

Lam, Y. W., & Monazzam, M. R. (2006). On the modeling of sound propagation over multi-impedance discontinuities using a semiempirical diffraction formulation. *Journal of the Acoustical Society of America*, 686-698.

Larsson, P., Vastfjall, D., & Kleiner, M. (2002, 6). Better Presence and Performance in Virtual Environments by Improved Binaural Sound Rendering. *Audio Engineering Society Conference: 22nd International Conference: Virtual, Synthetic, and Entertainment Audio.* Ανάκτηση από http://www.aes.org/e-lib/browse.cfm?elib=11148

Lauterbach, C., Chandak, A., & Manocha, D. (2007). Interactive sound rendering in complex and dynamic scenes using frustum tracing. *Visualization and Computer Graphics, IEEE Transactions on, 13*, 1672-1679.

Lehmann, E. A., & Johansson, A. M. (2008). Prediction of energy decay in room impulse responses simulated with an image-source model. *The Journal of the Acoustical Society of America, 124*, 269.

Lehmann, E. A., & Johansson, A. M. (2010). Diffuse reverberation model for efficient image-source simulation of room impulse responses. *Audio, Speech, and Language Processing, IEEE Transactions on, 18*, 1429-1439.

Lehmann, E. A., & Johansson, A. M. (2010). Diffuse reverberation model for efficient image-source simulation of room impulse responses. *Audio, Speech, and Language Processing, IEEE Transactions on, 18*, 1429-1439.

Lehnert, H. (1993). Systematic errors of the ray-tracing algorithm. *Applied Acoustics, 38*, 207-221.

Lentz, T., Schröder, D., Vorländer, M., & Assenmacher, I. (2007). Virtual reality system with integrated sound field simulation and reproduction. *EURASIP Journal on Applied Signal Processing, 2007*, 187-187.

L'Esperance, A., Herzog, P., Daigle, G. A., & Nicolas, J. R. (1992). Heuristic Model for Outdoor Sound Propagation Based on an Extension of the Geometrical Ray Theory in the Case of a Linear Sound Speed Profile. *Applied Acoustics*, 111-139.

Lewers, T. (1993). A combined beam tracing and radiatn exchange computer model of room acoustics. *Applied Acoustics, 38*, 161-178.

Liu, D. S.-M., & Tan, C.-M. (2016). Visibility preprocessing suitable for virtual reality sound propagation with a moving receiver and multiple sources. *IEEE International Conference on Multimedia & Expo Workshops (ICMEW).*

Lokki, T., Southern, A., & Savioja, L. (2011). Studies on seat dip effect with 3D FDTD modeling. *Forum Acusticum.* Aalborg.

Macdonald, T. M. (1915). A class of diffraction problems. *Proc. Lond. Math. Soc.*, 410-427.

Manocha, D., & Lin, M. C. (2009). Interactive sound rendering. *Computer-Aided Design and Computer Graphics, 2009. CAD/Graphics' 09. 11th IEEE International Conference on*, (σσ. 19-26).

Markovic, D., Antonacci, F., Sarti, A., & Tubaro, S. (2016). 3D Beam Tracing Based on Visibility Lookup for Interactive Acoustic Modeling. *IEEE Transactions on Visualization and Computer Graphics*, 2262-2274.

Mechel, F. (2012). *Room Acoustical Fields.* Springer Science & Business Media.

Mechel, F. P. (2002). Improved mirror source method in roomacoustics. *Journal of sound and vibration, 256*, 873-940.

Medwin, H. (1981). Shadowing by finite noise barriers. *Journal of the Acoustical Society of America*, 1060-1064.

Mehra, R., Manocha, D., Antani, L., & Raghuvanshi, N. (2012). Real-time sound propagation and noise modeling in outdoor environments using Equivalent

Source Formulation. *The Journal of the Acoustical Society of America, 132*, 1890.

Mehra, R., Raghuvanshi, N., Antani, L., & Manocha, D. (2012). A real-time sound propagation system for noise prediction in outdoor spaces. *INTER-NOISE and NOISE-CON Congress and Conference Proceedings*, *2012*, σσ. 7026-7035.

Mehra, R., Raghuvanshi, N., Antani, L., Chandak, A., Curtis, S., & Manocha, D. (2013). Wave-based sound propagation in large open scenes using an equivalent source formulation. *ACM Transactions on Graphics (TOG), 32*, 19.

Mehra, R., Raghuvanshi, N., Savioja, L., Lin, M. C., & Manocha, D. (2012). An efficient GPU-based time domain solver for the acoustic wave equation. *Applied Acoustics, 73*, 83-94.

Menounou, P., & Nikolaou, P. (2017). Analytical model for predicting edge diffraction in the time domain. *The Journal of the Acoustical Society of America*.

Menounou, P., Busch-Vishniac, I., & Blackstock., D. (2000). Directive line source model: A new model for sound diffraction by half planes and wedges. *Journal of the Acoustical Society of America*, 2973-2986.

Michael, D., & Chrysanthou, Y. (2010). Fullsphere Irradiance Factorization for Real-Time All-Frequency Illumination for Dynamic Scenes. *Computer Graphics Forum*, *29*, σσ. 2516-2529.

Michael, D., Pelekanos, N., Chrysanthou, I., Zaharias, P., Hadjigavriel, L. L., & Chrysanthou, Y. (2010). Comparative study of interactive systems in a museum. Στο *Digital Heritage* (σσ. 250-261). Springer.

Min, H., & Xiaojun, Q. (2009). Multiple acoustic diffraction around rigid parallel wide barriers. *Journal of the Acoustical society of America*, 179-186.

Min, P., & Funkhouser, T. (2000). Priority-Driven Acoustic Modeling for Virtual Environments. *Computer Graphics Forum*, *19*, σσ. 179-188.

Morse, P. M., & Bolt, R. H. (1944). Reviews of Modern Physics: Sound Waves in Rooms. *Massachusetts Institute of Technology*, 69-150.

Murphy, D., Beeson, M., Shelley, S., Moore, A., & Southern, A. (2008). Hybrid room impulse response synthesis in digital waveguide mesh based room acoustics

simulation. *Proceedings of the 11th International Conference on Digital Audio Effects (DAFx-08)*, (σσ. 129-136).

Naylor, G. M. (1993). ODEON—Another hybrid room acoustical model. *Applied Acoustics, 38*, 131-143.

Nirenstein, S. (2003). *Fast and accurate visibility preprocessing.* Ph.D. dissertation, University of Cape Town.

Nord2000: Nordic noise prediction method. (2019). Ανάκτηση από Ministry of Environment and Food of Denmark - Envoronmental Protection Agency: https://eng.mst.dk/air-noise-waste/noise/traffic-noise/nord2000-nordic-noise-prediction-method/

Nosal, E.-M., Hodgson, M., & Ashdown, I. (2004). Improved algorithms and methods for room sound-field prediction by acoustical radiosity in arbitrary polyhedral rooms. *The Journal of the Acoustical Society of America, 116*, 970.

Nosal, E.-M., Hodgson, M., & Ashdown, I. (2004). Investigation of the validity of radiosity for sound-field prediction in cubic rooms. *The Journal of the Acoustical Society of America, 116*, 3505.

Oberhettinger, T. (1954). Diffraction of waves by a wedge. *Comm. Pure Appl. Math.*, 551-563.

Ocansey , D. T., & Bikdash, M. (2016). Modeling the effect of atmospheric attenuation on a propagation outdoor noise. *SoutheastCon.* Norfolk: IEEE.

Okada, M., Onoye, T., & Kobayashi, W. (2012). A Ray Tracing Simulation of Sound Diffraction Based on the Analytic Secondary Source Model. *Audio, Speech, and Language Processing, IEEE Transactions on, 20*, 2448-2460.

Olive Tree Lab Suite. (2020). Ανάκτηση από https://www.mediterraneanacoustics.com/olive-tree-lab-suite.html

Ostashev, V., Clifford, S., Lataitis, R., Blanc-Benon, P., & Juve, D. (2000). The effects of atmospheric turbulence on the interference of the direct and ground reflected waves. *The 29th International Congress and Exhibition on Noise Control Engineering.* Nice.

Ouis, D. (2019). Diffraction of a spherical wave by a hard half-plane: Approximation of the edge field in the frequency domain. *The Journal of the Acoustical Society of America*.

Peerdeman, P. (2006). Sound and Music in Games. *And Haugehåtveit, O*.

Pierce, A. D. (1974). Diffraction of sound around corners and over wide barriers. *Journal of the Acoustical Society of America*, 941-955.

Pierce, A. D. (1994). *Acoustics: An Introduction to Its Physical Principles and Applications.* New York: Acoustical Society of America.

Plovsing, B., & Kragh, J. (2009). *Validation of the Nord2000 propagation model for use on wind turbine noise, Report AV 1236/09.* Hørsholm: DELTA Acoustics and Electronics.

Plovsing, B; Kragh, J. (2006). *Nord2000. Comprehensive Outdoor Sound Propagation Model. Part 2: Propagation in an Atmosphere with Refraction.* Hørsholm: DELTA Acoustics & Vibration Report AV 1851/00.

Porter, M. B. (2019). Beam tracing for two- and three-dimensional problems in ocean acoustics. *The Journal of the Acoustical Society of America*.

Raghuvanshi, N. (2010). *Interactive Physically-based Sound Simulation.* Ph.D. dissertation, University of North Carolina.

Raghuvanshi, N., Snyder, J., Mehra, R., Lin, M., & Govindaraju, N. (2010). Precomputed wave simulation for real-time sound propagation of dynamic sources in complex scenes. *ACM Transactions on Graphics (TOG), 29*, 68.

Röber, N., Kaminski, U., & Masuch, M. (2007). Ray acoustics using computer graphics technology. *10th International Conference on Digital Audio Effects (DAFx-07), S*, (σσ. 117-124).

Röber, N., Kaminski, U., & Masuch, M. (2007). Ray acoustics using computer graphics technology. *10th International Conference on Digital Audio Effects (DAFx-07), S*, (σσ. 117-124).

Rodriguez, J.-V., Pascual-Garcia, J., Martínez-Inglés, M.-T., Molina-Garcia-Pardo, J.-M., & Juan-Llácer, L. (2017). Uniform theory of diffraction (UTD)-based

solution for sound diffraction caused by an array of obstacles. *The Journal of the Acoustical Society of America*.

Russell, R. D., & Stuart, J. (1995). *Artificial intelligence: a modern approach.* 1995: Englewood Cliffs: Prentice hall.

Sakurai, Y., & Nagata, K. (1981). Sound reflections of a rigid plane and of the "live end" composed by those panels. *Journal of the Acoustical Society of America*, 5-14.

Salomons, E. (1997). Sound propagation in complex outdoor situations. *Acta Acoustica*, 436-454.

Salomons, E. M. (1994). Downwind propagation of sound in an atmosphere with a realistic sound-speed profile: A semianalytical ray model. *Journal of the Acoustical Society of America, 95*(5), 2425-2436.

Salomons, E. M. (1998). Caustic diffraction fields in a downward refracting atmosphere. *Journal of the Acoustical Society of America, 104*(6), 3259-3272.

Samarasinghe, P. N., Abhayapala, T. d., Lu, Y., Chen, H., & Dickins, G. (2018). Spherical harmonics based generalized image source method for simulating room acoustics. *The Journal of the Acoustical Society of America*, 1381-1391.

Savioja, L. (2010). Real-time 3D finite-difference time-domain simulation of low-and mid-frequency room acoustics. *13th Int. Conf on Digital Audio Effects*, *1*, σ. 75.

Savioja, L., & Svensson, U. P. (2015). Overview of geometrical room acoustic modeling techniques. *The Journal of the Acoustical Society of America, 138*, 708-730.

Savioja, L., Huopaniemi, J., Lokki, T., & Väänänen, R. (1999). Creating interactive virtual acoustic environments. *Journal of the Audio Engineering Society, 47*, 675-705.

Schissler, C., Mehra, R., & Manocha, D. (2014). High-order diffraction and diffuse reflections for interactive sound propagation in large environments. *ACM Transactions on Graphics (TOG), 33*, 39.

Schröder, D., & Lentz, T. (2006). Real-time processing of image sources using binary space partitioning. *Journal of the Audio Engineering Society, 54*, 604-619.

176

Schultz, T. J., & Watters, B. G. (1964). Propagation of sound across audience seating. *Journal of the Acoustical Society of America*, 885-896.

Sessler, G. M., & West, J. E. (1964). Sound transmission over theatre seats. *Journal of the Acoustical Society of America*, 1725-1732.

Sikora, M., & Mateljan, I. (2013). A method for speeding up beam-tracing simulation using thread-level parallelization. *Engineering with Computers*, 1-10.

Sikora, M., Mateljan, I., & Bogunović, N. (2012). Beam tracing with refraction. *Archives of Acoustics, 37*, 301-316.

Sikora, M., Russo, M., & Mateljan, I. (2018). Hybrid Beam/Ray Tracing Simulation Method. *Euronoise.*

Siltanen, S. (2010). Efficient physics-based room-acoustics modeling and auralization. *Aalto-yliopiston teknillinen korkeakoulu.*

Siltanen, S., Lokki, T., Kiminki, S., & Savioja, L. (2007). The room acoustic rendering equation. *The Journal of the Acoustical Society of America, 122*, 1624.

Siltanen, S., Lokki, T., Savioja, L., & Lynge Christensen, C. (2008). Geometry reduction in room acoustics modeling. *Acta Acustica united with Acustica, 94*, 410-418.

SoundPlan. (2020, October 01). Ανάκτηση από SoundPlan: https://www.soundplan.eu/en/software/soundplannoise/product-description/

Southern, A., & Siltanen, S. (2013). A hybrid acoustic model for room impulse response synthesis. *Proceedings of Meetings on Acoustics*, *19*, σ. 015113.

Southern, A., Siltanen, S., & Savioja, L. (2011). Spatial room impulse responses with a hybrid modeling method. *Audio Engineering Society Convention 130.*

Stavrakis, E., Tsingos, N., & Calamia, P. (2008). Topological sound propagation with reverberation graphs. *Acta Acustica united with Acustica, 94*, 921-932.

Stephenson, U., & Svensson, U. P. (2007). An improved energetic approach to diffraction based on the Uncertainty Principle. *Proc. 19th Intl. Congress on Acoustics (ICA).* Madrid.

Svensson, P., & Krokstad, A. (2008). The early history of ray tracing in room acoustics. *Reflections on sound: In honour of Professor Emeritus Asbjørn Krokstad. Norwegian University of Science and Technology*.

Svensson, U. P., Fred, R. I., & Vanderkooy, J. (1999). An analytic secondary source model of edge diffraction impulse responses. *Journal of the Acoustical Society of America*, 2331-2344.

Tahvanainen, H., Pätynen,, J., & Lokki, T. (2015). Analysis of the seat-dip effect in twelve European concert halls. *Acta Acustica united with Acustica*, 731-742.

Takahashi, D. (1997). Seat dip effect: The phenomena and mechanism. *Journal of the Acoustical Society of America*, 1102-1119.

Takahashi, D. (1997). Seat dip effect: The phenomena and the mechanism. *Journal of the Acoustical Society of America*, 1326-1334.

Taylor, M. T., Chandak, A., Antani, L., & Manocha, D. (2009). Resound: interactive sound rendering for dynamic virtual environments. *Proceedings of the 17th ACM international conference on Multimedia*, (σσ. 271-280).

Taylor, M., Chandak, A., Mo, Q., Lauterbach, C., Schissler, C., & Manocha, D. (2012). Guided multiview ray tracing for fast auralization. *IEEE transactions on visualization and computer graphics, 18*, 1797-1810.

Taylor, M., Chandak, A., Ren, Z., Lauterbach, C., & Manocha, D. (2009). Fast edge-diffraction for sound propagation in complex virtual environments. *EAA auralization symposium*, (σσ. 15-17).

Tenenbaum, R. A., Taminato, F. O., & Melo, V. S. (2019). Room acoustics modeling using a hybrid method with fast auralization with artificial neural network techniques. *PROCEEDINGS of the 23rd International Congress on Acoustics* . Aachen.

Thompson, L. L. (2006). A review of finite-element methods for time-harmonic acoustics. *The Journal of the Acoustical Society of America, 119*, 1315.

Tolstoy, I. (1982). Coherent sound scatter from a rough interface between arbitrary fluids with particular refer-ence to roughness element shapes and corrugated surfaces. *Journal of the Acoustical Society of America*, 960-972.

Trorey, W. (1970). A simple theory for seismic diffractions. *Geophysic*, 762-784.

Trorey, W. (1977). Diffraction for arbitrary source receiver locations. *Geophysics*, 1177-1182.

Tsingos, N. (2009). Precomputing geometry-based reverberation effects for games. *Audio Engineering Society Conference: 35th International Conference: Audio for Games.*

Tsingos, N., & Gascuel, J.-D. (1997). Acoustic simulation using hierarchical time-varying radiant exchanges. *Unpublished tech. report, iMAGIS-GRAVIR/IMAG.*

Tsingos, N., Dachsbacher, C., Lefebvre, S., & Dellepiane, M. (2007). Instant sound scattering. *Proceedings of the 18th Eurographics conference on Rendering Techniques*, (σσ. 111-120).

Tsingos, N., Funkhouser, T., Ngan, A., & Carlbom, I. (2001). Modeling Acoustics in Virtual Environments Using the Uniform Theory of Diffraction. *ACM SIGGRAPH*, 545-553.

Tsingos, N., Gallo, E., & Drettakis, G. (2004). Perceptual audio rendering of complex virtual environments. *ACM Transactions on Graphics (TOG)*, *23*, σσ. 249-258.

Tsingos, N., Gascuel, J.-D., & others. (1997). Soundtracks for computer animation: sound rendering in dynamic environments with occlusions. *Graphics Interface'97.*

Tsingos, N., Jiang, W., & Williams, I. (2011). Using programmable graphics hardware for acoustics and audio rendering. *Journal of the Audio Engineering Society, 59*, 628-646.

Twersky, V. (1957). On scattering and reflection of sound by rough surfaces. *Journal of the Acoustical Society of America*, 209-225.

Vanderkooy, J. (1991). A simple theory of cabinet edge diffraction. *Journal of the Audio Engineering Society*, 923-933.

Vorlander, M. (2010). *Auralization: Fundamentals of acoustics, modeling, simulation, algorithms and acoustic virtual reality.* Springer.

Vorländer, M. (1989). Simulation of the transient and steady-state sound propagation in rooms using a new combined ray-tracing/image-source algorithm. *The Journal of the Acoustical Society of America, 86*, 172.

Vorlander, M. (2010). *Auralization: fundamentals of acoustics, modelling, simulation, algorithms and acoustic virtual reality.* Springer Publishing Company, Incorporated.

Vorländer, M. (2013). Computer simulations in room acoustics: Concepts and uncertainties. *The Journal of the Acoustical Society of America, 133*, 1203.

Wang, H., Cai, M., & Hongjun, C. (2019). Simulation and Analysis of Road Traffic Noise among Urban Buildings Using Spatial Subdivision-Based Beam Tracing Method. *Int. J. Environ. Res. Public Health*.

Wang, H., Gao, H., & Cai, M. (2019). Simulation of traffic noise both indoors and outdoors based on an integrated geometric acoustics method. *Building and Environment*.

West, M., Walkden, F., & Sack, R. A. (1989). The Acoustic Shadow Produced by Wind Speed and Temperature Gradients Close to the Ground. *Applied Acoustics*, 239-260.

West, M., Walkden, F., & Sack, R. A. (1989). The Acoustic Shadow Produced by Wind Speed and Temperature Gradients Close to the Ground. *Applied Acoustics*, 239-260.

Wolfgang, P., & Lars, S. (2019). Calculation of Multiple Diffraction in a Downward Refracting Atmosphere With Ray-Based Engineering Models. *Acta Acustica united with Acustica*, 226-230.

WP2 Team. (2002). *Task 2.2. State of the art of modeling.* Delft: HAR22TR-020222-TNO03.

WP2 Team. (2002). *Task 2.3. Benchmark calculations and modeling approximations .* Delft: HAR23TR-020222-TNO10.

Yeh, H., Mehra, R., Ren, Z., Antani, L., Manocha, D., & Lin, M. (2013). Wave-ray coupling for interactive sound propagation in large complex scenes. *ACM Transactions on Graphics (TOG), 32*, 165.

Zechen, Z. (2019). *Spatial Computing of Sound Fields in Virtual Environments.* Cornell
University.

7   Appendix

7.1   Ray Equivalency Theorem

7.1.1   Axioms

1. Keller's law, which follows the principle of minimum path length (Fermat's
    principle), states that the angle of incidence at an edge is equal to the angle of
    diffraction (Keller, 1962). (Figure 92 a).

2. Any curve in space can be geometrically represented as a straight line of
    negligible length, lying on the tangent of the curve at that locality. Any ray
    intersecting a curve at a certain point is a local issue and equivalent to studying
    the behavior of a ray intersecting the tangent at that given point (Figure 92 b).
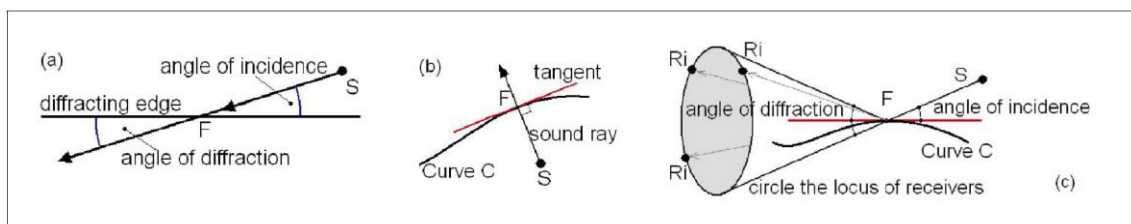

Figure 92. Keller's Law

A diffracted sound ray is formed by a line connecting a diffracting point F on an edge
and a receiver R. The incident sound ray between the source and a diffracting point is
formed based on Axiom 2 above. The receiver point may only be found on a cone's
surface area, with its apex being the diffraction point F, cone sides being the distance of
FR and an apex angle being twice the angle of incidence (Axiom 1, Figure 92 c).

As a result, in a three-dimensional space, a diffracted ray from a point F on a curve C is equivalent to the diffracted ray from its tangent at that point. The diffracted ray may be found on a cone, with its apex being the diffraction point F and an apex angle being twice the angle of incidence of the incoming ray on the same tangent.

7.1.2   Theorem

Given a circular arc C with length $< \pi$, a point S on an axis L perpendicular to the plane of the arc at its center at point P, and a point Ro not on L, there is only one incident diffracting ray from S to Ro on arc C via the diffraction point F. Point F belongs to both the arc C and its tangent at that point, and Ro is only found on a circle formed with its center being the diffracting point F and a FRo radius (Figure 93).
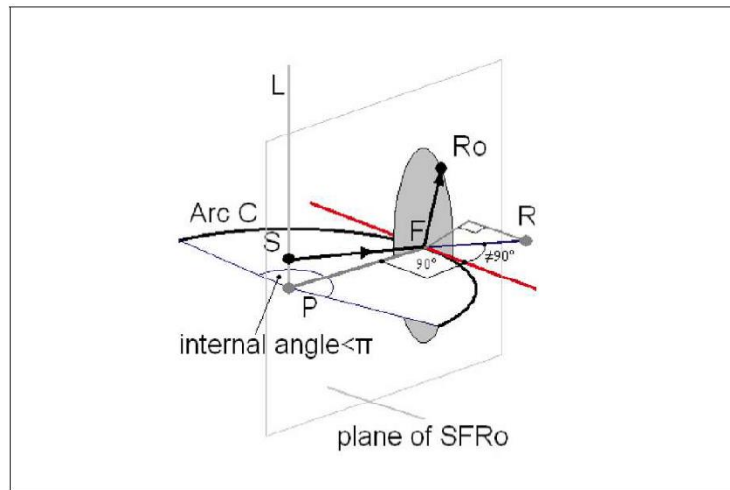

Figure 93. Diffraction from a circular arc

7.1.3   Proof

Any point R not on the plane formed by SFRo, cannot receive a ray from S since the angle of incidence does not equal to the angle of diffraction, a violation of Axiom 1 (Figure 93).

7.2 PEMARD Publication Approval

P.E. Mediterranean Acoustics Research & Development Ltd
P.O.Box 51443, CY 3505, Limassol CYPRUS
No 1 Ammochostou St, Trimiklini 4730
Tel: +357 25 822 816, Fax: +357 25 822 817
Email: info@pemard.com
Website: www.pemard.com

24 November 2020

TO WHOM IT MAY CONCERN,

We would like to acknowledge that the industrial part of the research work included in Panagiotis Charalampous doctoral dissertation with title "Wave-Based Geometrical Acoustics for Accurate and Efficient Sound Rendering" has been carried out during Panagiotis' employment at PEMARD. More specifically, in relation to the industrial PhD work of this thesis, Panagiotis' contribution is related to the algorithms developed for the detection of sound paths for sound reflections, sound diffractions and sound refractions, as they have been described in Sections 3.1, 3.2, 3.3 respectively, to the validation projects presented in Section 3.4 and to the algorithm presented in section 4.3, of the aforementioned thesis. We are fully aware of the content that is included in this thesis and we grant the approval for this and as well for the work to be published.

Panagiotis' main responsibility was the algorithmic part of the project, which is the main focus of the industrial part of this PhD work. Panagiotis was responsible for conceiving, designing and developing all the corresponding new algorithms described in the thesis, and specifically the enhanced image source method using a visibility matrix and visibility beams, the multiple diffraction path detection algorithm, the reflected-diffracted paths detection algorithm as well as the refraction path detection algorithm. Panagiotis was also responsible for the results outputs of the algorithms by running simulations/taking measurements and doing comparisons.

P.E. Mediterranean Acoustics
Research & Development Ltd

Panos Economou
Founder, Director

Directors:
Panos Economou (Managing) BSc, MSc, MASA, MIOA, MAES, MIEEE, MHELINA, ETEK
Lina Economou